Doctoral Thesis

Gravitational physics tests with a Rubidium atom interferometer

Author:
Giulio D'Amico

Supervisor:
Prof. Guglielmo Tino

UNIVERSITÀ
DEGLI STUDI
FIRENZE

September 13, 2018

Contents

List of Figures

Chapter 1

Introduction

The measurements that we report in this thesis were realized with the MAGIA-Advanced (MAGIA-Adv) experimental apparatus at the Florence University and INFN Florence. This apparatus is a vertical fountain Atom Interferometer originally developed to perform the first determination of the Newtonian gravitational constant G through atom interferometry. The apparatus is now used to perform other high sensitivity gravitational tests and to develop novel experimental techniques in the field of atom gravimetry and gradiometry, i.e. for the measurement of the gravity acceleration and the gravity gradient respectively.

In this first chapter we intuitively introduce the notion of atom interferometry and its similarities with the standard light interferometry experiments. We then present the main applications of atom interferometers which derive from their high sensitivity to inertial forces and briefly discuss the main motivation and importance of a determination of G through atom interferometry. We conclude the chapter introducing the new measurements realized in the last three years with the advanced set-up.

1.1   Light interferometry - Atom interferometry

An Atom Interferometer (AI) [1], [2] is an instrument which, taking advantage of the matter wave nature, generates the phenomenon of interference between two or more matter wave-fronts and uses it to measure some quantity of interest. In this regard an AI is conceptually analogous to a standard light interferometer, but the role between matter and light is completely exchanged.

Indeed in a light interferometer a beam of coherent light is split and let propagate through two different optical paths; the light beams are manipulated with the use of material objects (glass beam-splitters, mirrors, gratings, etc...) and several different arrangements are possible [3]. As soon as the light beams are recombined their intensity shows an interference pattern as a function of the relative optical path length.

Of all the possible interferometric geometries, we will focus mainly on the Mach-Zehnder (MZ) configuration which is one of the most implemented geometries both in light and atom interferometers[1]. In the case of a light interferometer the MZ geometry is typically realized with the use of two glass beam-splitters and two mirrors; an initial beam-splitter is used to define two interferometric arms by splitting the incoming coherent light beam; the arms are then recombined with the use of two mirrors in the final beam splitter and the light intensity from one output is finally recorded. If the two optical paths have equal optical length there will be no phase

---

[1]The Mach-Zehnder configuration is also the one originally implemented in the MAGIA apparatus. In the following we will always refer to this particular geometry unless stated otherwise.
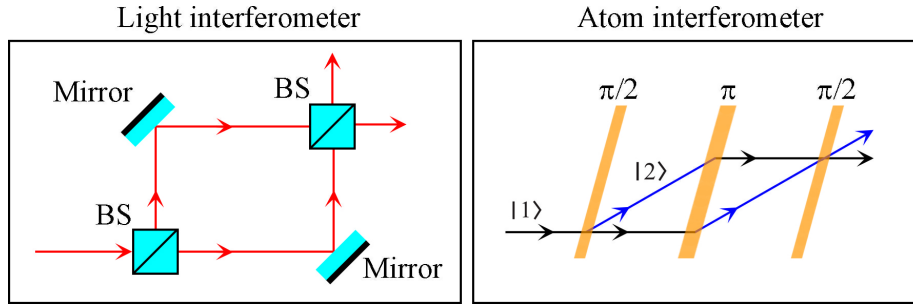
FIGURE 1.1: Comparison between a light (left) and an atom (right) interferometer in the Mach-Zehnder configuration. In the AI the $\pi/2$ pulses act as beam-splitters (BS) for the matter-wave, while the π pulses act as mirrors (see Sec. 2.1.1). From the figure we can note the complete analogy between the two configurations. In the light interferometer the phase difference between the two interferometric arms is mapped on the output light intensity while in the AI it is mapped on the atomic population in states $|1\rangle$ and $|2\rangle$ detected after the final $\pi/2$ pulse.

shift between them; however if the optical length of one path is changed, an extra phase shift ϕ will emerge between the two interferometric arms and the light intensity will manifest an interference pattern as a function of ϕ.

We show the described configuration in the left panel of Fig. 1.1 and compare it with its atomic counterpart reported in the right panel of Fig. 1.1. In this case the situation is exactly equivalent, but the atomic wave-function takes the place of the coherent light beam while the material beam-splitters and mirrors are substituted with pulses of coherent light. Considering the atom as a simple two-level system, the so called $\pi/2$ and π pulses (see Sec. 2.1.1) act as beam-splitters and mirrors for the atomic wave-function and are able to connect the two different atomic states $|1\rangle$ and $|2\rangle$ which generally differ both in the external or internal degrees of freedom (i.e. atomic momentum or electronic energy level, respectively). The splitting of the interferometric arms in the case of an AI can therefore be obtained both spatially and on the internal atomic states[2]. At the moment of the final beam-splitter (final $\pi/2$ pulse), when the wave-fronts are recombined, an interference pattern can be observed in the atomic state population as a function of the phase difference ϕ accumulated between the two interferometric paths. Indeed the probability of detecting an atom in one of the two considered states can be written as $P = \frac{1}{2}(1 + \cos(\phi))$, i.e. as an oscillatory function of the interferometric phase; the atomic population thus shows a typical interferometric fringe.

The phase ϕ is sensitive to the different local forces that the wave-functions experience in the distinct interferometric arms. Furthermore, an atom is intrinsically more sensitive to environmental conditions than a photon and since atoms are massive particles they are affected by gravitational fields. For these reasons an AI can be used as a high sensitivity external field sensor and in particular as a high sensitivity inertial and gravitational force sensor.

As we will analyse in Ch. 4 a typical AI experiment is composed of three distinct parts. Initially we have the preparation stage which can involve the trapping,

---

[2]As we will see this happens when the π and $\pi/2$ pulses are realized with Raman transitions. However this is not always the case. Indeed if the manipulation pulses are implemented using multi-photon Bragg transitions the separation of the arms will be only on the external atomic degrees of freedom.

cooling and launching of one or several atomic samples. Then the prepared ensembles are interrogated in the chosen interferometric sequence applying subsequent coherent light pulses. Finally the atomic population in the two states involved in the interferometer is measured in order to retrieve the interferometric phase ϕ.

1.2 Atom interferometers as inertial sensors

The idea of a matter-wave interferometer is an old one. The first implementation was realized by E. Fermi in 1947 [4] with slow neutrons; only a few years later came the first MZ interferometer for electrons [5]. Already at that time it was clear that in order to realize highly sensitive devices the use of neutral matter was preferable to charged particles or photons. A neutral particle is indeed much less sensitive to perturbing electric or magnetic fields and its speed can be reduced to values $\ll c$ (c is the speed of light) allowing a much longer interaction time. Neutrons were a good candidate, but they resulted difficult to produce in laboratory since an accelerator was needed; the use of neutral atoms became feasible only in the 90's even if the idea was around from before [6], [7]. The first neutral atom interferometers were demonstrated in 1991 by four different research groups. Two experiments still used material beam-splitters realized with micro-fabricated slits [8] or gratings [9]; the other two experiments exploited the atom-light interaction to realize the beam-splitters and mirrors for the matter-waves; one with single photon transitions [10], the other with two-photon transitions [11].

After these first demonstrations, AIs experienced a rapid development; their growing impact on practical applications derives from the great improvements in the understanding of the atomic internal structure and consequently in the ability to manipulate atoms with laser radiation. New experimental techniques in laser cooling permitted to reach higher coherence levels of the atoms and also to increment the interrogation time by orders of magnitude.

Nowadays AIs can be used to perform a wide variety of useful measurements and their performances are comparable, if not superior to other competing instruments. The most successful scheme proved to be the one first demonstrated at Stanford [12] which uses two-photon Raman transitions to manipulate the neutral atoms. This scheme finds important applications in particular in the measurement of inertial forces. Following the first AI demonstration, the Earth rotation rate was measured with a short term sensitivity of 6×10^{-10} rad/s after 1 s of integration [13], [14] while the gravity acceleration was determined with a precision of $2 \times 10^{-8}g$ with a single measurement cycle of 1.3 s, $3 \times 10^{-9}g$ after one minute of integration and of $1 \times 10^{-10}g$ after an integration of two days [15]. The Earth gravity gradient was also measured with a precision of 4×10^{-8} s$^{-2}/\sqrt{\text{Hz}}$ [16], [17].

A precise determination of the gravitational acceleration g and of its gradient have important applications in many scientific fields. Geophysics and metrology are two common examples, but also more practical applications can be found in prospecting for underground resources (oil, water, etc...). In this regard, transportable and rugged apparatuses have been engineered and assembled for mapping Earth mass anomalies, for monitoring volcanoes activity and also to measure gravitational changes before earthquakes. The high sensitivity to inertial forces makes the transportable AIs extremely interesting also for inertial navigation systems [18].

Furthermore AIs have been used for measurements of fundamental physics; several examples are found in the determination of fundamental constants like h/m_{Cs} [19], h/m_{Na} [20], G [21] and the atomic polarizability [22], [23]; another example

is the use of AIs for testing the Einstein Equivalence Principle [24], [25], the $1/r^2$ Newton's law for short distances [26] and general relativity [27].

1.3   Measuring G with atom interferometry

The MAGIA apparatus was designed to provide a precise measurement of the Newtonian gravitational constant G. The experiment was successfully completed in 2014 [21] and now the apparatus has been used to realize several other gravitational measurements. However, in order to understand the particular design of the MAGIA set-up it is important to briefly describe the principle of the G determination and why this measurement is particularly relevant.

The Newtonian gravitational constant is the fundamental quantity known with the highest relative uncertainty. The last CODATA recommended value is

$$G = 6.67384(80) \times 10^{-11} \ \mathrm{m^3 kg^{-1} s^{-2}}, \tag{1.1}$$

with a relative uncertainty of 1.2×10^{-4}. This is due to the fact that independent determinations of G are not consistent with each other by several parts in 10^{-4}.

The particular nature of the gravitational force poses several difficulties in the experimental determination of the constant G. Indeed gravity cannot be shielded or compensated for; it is the dominating force in regimes of large neutral masses and large distances, but due to its weakness the other forces can produce large systematic effects in laboratory experiments. For these reasons all the classical determinations of G which are based on macroscopic suspended masses, i.e. torsion pendulums, or free-falling corner cubes suffer from systematics which are difficult to characterize; atom interferometry represents an alternative method for measuring G with a completely different systematic budget from the classical experiments and it can be used to validate one of the previous inconsistent measurements thus reducing the relative uncertainty on G.

In the MAGIA experiment [28], [29] G is determined from the measurement of the differential acceleration experienced by two samples of cold ^{87}Rb atoms in presence of a well characterized set of source masses. The measurement is repeated for two different and well known dispositions of the source masses; this permits to eliminate the contribution on the interferometer phase of the Earth gravitational field and maintain only the effect of the masses. From the accurate knowledge of the source mass density distribution its effect on the interferometric phase can be simulated and the value of G can be determined.

In Fig. 1.2 we report the main vacuum system of the MAGIA apparatus and the two configurations for the source masses used in the G measurement. Two atomic samples are collected in the trap chamber and launched inside the 1 m long interferometric tube. The atomic interrogation with the interferometer happens simultaneously for both the ensembles with the same laser pulses and during the free fall motion. The instrument is therefore sensitive to the differential acceleration between the two samples; repeating the measurement in the two different masses configurations the effect of the Earth gravitational field is cancelled through an additional differential measurement stage.

The double differential measurement scheme allows to reject several systematic contributions which appear as common mode noise between the simultaneous interferometers. However, the major source of systematic uncertainty in the measure
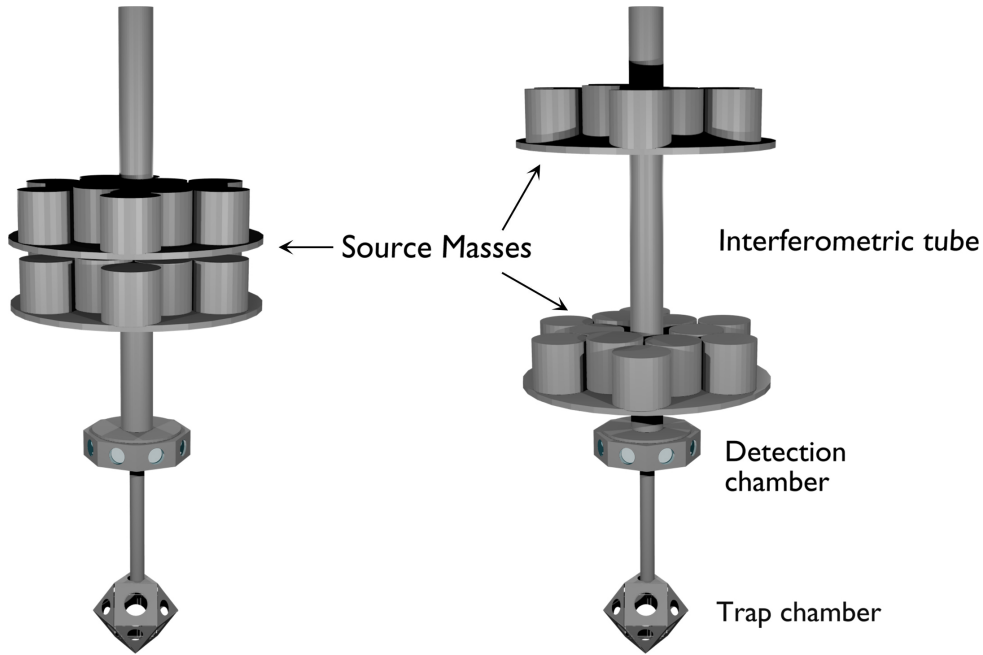
FIGURE 1.2: Overview of the MAGIA vacuum system and of the two different source masses arrangements used for the double differential measurement of G. ^{87}Rb atoms are loaded in the trap chamber at the bottom of the set-up in a 3D-MOT; two samples are launched vertically inside the interferometric tube producing the atomic fountain. When the clouds are near the apogees of the parabolic trajectories their vertical acceleration is measured with a MZ atom interferometer. The measurement is repeated in the two different configurations of the source masses.

arises from the limited control on the position and velocity of the atoms in the thermal cloud [30]. We will address this point and present an experimental method which could in principle solve this issue in Sec. 5.4.

With the presented method the measured G value was

$$G_{\mathrm{AI}} = 6.67191(99) \times 10^{-11} \ \mathrm{m^3 kg^{-1} s^{-2}}, \tag{1.2}$$

with a relative uncertainty of 150 parts per million.

1.4   Measurements with the MAGIA-Adv apparatus

The AI in the MAGIA apparatus was originally realized with two-photon Raman transitions as atom-optical elements; these transitions couple the two levels of the hyperfine ground state doublet of ^{87}Rb and are able to transfer twice an optical photon momentum to the atoms. Recently we added the possibility of exciting multiphoton Bragg processes; these processes do not change the internal atomic state and can transfer more momentum to the atoms with respect to Raman transitions. This can be advantageous in an AI since its sensitivity to inertial forces scales linearly with the momentum imparted to the atoms. In order to excite Bragg transitions we added a completely new laser system based on a high power fibre amplifier with emission centred at 1560 nm. We will describe in detail the optical configuration of this new laser system in Sec. 3.3.6.

We initially performed some characterization measurements in order to define the best experimental conditions of the new Bragg interferometer. Later, we exploited the fact that Bragg transitions do not change the internal atomic state to perform a Weak Equivalence Principle (WEP) test for ^{87}Rb atoms in different energy states. AIs are indeed largely used to performs this kind of tests in which they compare the free fall acceleration of different atoms [31]–[34] or of atoms in different internal states [24], [35].

Our measurements improve by one order of magnitude the sensitivity achieved in the WEP tests for ^{87}Rb atoms in different internal states; more importantly they also provide a conceptually new test of the WEP accessing genuine quantum aspects of the principle [25] remained so far unexplored. Indeed we test the WEP using atoms in a coherent superposition state, thus a state with no classical counterpart and for which a specific quantum formulation of the WEP is needed.

After the measurements for the WEP test we present an experiment in which we demonstrate a method to cancel the effects of gravity gradients (GGs) on the atom interferometer phase shift. Indeed a GG produces a systematic phase shift which depends on the atomic position and velocity at the start of the interferometer. This effect can be problematic for highly sensitive measurements with AI; in this regard we already mentioned that this is the major contribution in the systematic budget for the *G* measurement with AIs. However a possible compensation strategy was theoretically proposed in [36]; the principle of the method is simple and consists in slightly modifying the amount of transferred momentum to the atoms during the central mirror pulse of a MZ interferometer. In this way it is possible to make the atomic trajectories perfectly symmetric with respect to the central π pulse and cancel the systematic shift. We implemented this solution in our Raman interferometer; furthermore since in our apparatus we can realize two or three simultaneous interferometers we could use the compensation method as a technique to measure the average gravity gradient over the separation baseline between the simultaneous interferometers.

The final set of measurements that we present is the demonstration of a new method to perform a gravimetric measure with an AI. The method is based on a simpler interferometric scheme than the MZ one; we use the Ramsey interferometric scheme which is composed of only two $\pi/2$ pulses closely spaced in time. The time separation between the interferometric pulses in this configuration is about three orders of magnitude smaller than the one used in the MZ geometry. This is necessary since, without the mirror π pulse the atomic trajectories would not overlap sufficiently at the moment of the closing $\pi/2$ pulse. With this configuration it is possible to demonstrate that the interferometer phase shift depends on the atomic velocity. We can thus extract the value of the gravitational acceleration from two successive velocity measurements on the same freely falling sample, separated by a well known time. We demonstrate both theoretically and experimentally that this method is advantageous when performing gravimetric measurements in presence of strong vibration noise with respect to the standard MZ interferometer.

1.5 Organization of the thesis

In the next chapter we will present a brief theoretical introduction to the basic tools necessary for understanding an AI. We will start with the mechanisms of light-matter interaction focusing on two-photon Raman and multi-photon Bragg transitions. We will then present two different formalism for the calculation of the complete interferometric phase and consider the main contributions that can influence the interferometer.

In Ch. 3 we will describe the experimental apparatus. We will focus mainly on the laser system and describe the recent developments introduced for the stimulation of multi-photon Bragg diffraction processes.

In Ch. 4 we will describe the main experimental sequence used during the measurements starting from the atom trapping to the atomic detection. We will also present the typical signals measured with the apparatus during an interferometric measurement and introduce the analysis procedure.

Ch. 5 is dedicated to the experimental measurements realized in the three years PhD period. In the first section we will present the measurements done with the Bragg interferometer; we start with some characterization measurements and then present a test of the Weak Equivalence Principle in the quantum regime. In the second section we instead present the measurement realized with the Raman interferometer. The first one is the experimental demonstration of a novel method to compensate for the effect of a gravity gradient on an atom interferometer. We use this method to measure the average gravity gradient and the average gravity field curvature. With the second set of measurements we demonstrate a new gravimetric technique based on velocimetry measurements with atom interferometers.

In Ch. 6 we present a summary of the obtained results and the future prospects for the experiment.

Chapter 2

Theoretical formalisms for atom interferometry

In this chapter we introduce some of the essential theoretical tools needed for the understanding of multi-photon atom interferometry. The starting point in the analysis of the Atom Interferometer will be the theory of atom-light field interaction which will allow us to introduce the formalism of π and $\pi/2$ pulses, i.e. the main building blocks of any AI geometry. As we will see, these pulses allows the manipulation of the atomic wave-function in strict analogy to what can be done with mirrors and beam-splitters for a photon wave-function.

We initially present the simple, idealized case of a two-level atomic system in interaction with a monochromatic light field [37], [38]; then, considering more complex atomic structures, we analyse the theory of multi-photon processes focusing on Raman [39] and Bragg transitions [40], [41]. These two processes are largely used as atom-optic elements in atom interferometry and can both be implemented in our experimental apparatus. It is important to notice that with the use of these multi-photon interaction mechanisms the complex energy level structures of the atomic systems employed can still be considered as composed by only two-levels under typical experimental conditions.

In the case of Bragg diffraction we will see that in our experimental conditions it is not possible to provide an exact analytic solution of the atomic population dynamics; however we provide some numerical simulations of the behaviour of the atomic population versus different parameters of interest.

After the study of the atom-light field interaction processes we move on to the analysis of a complete MZ interferometric sequence and present the main physical phenomena that can induce a phase shift in the interferometric signal. The AI phase is derived with two different mathematical formalisms, the Feynman path integral formalism [42] and the sensitivity function approach [39], [43]. Even if these formalisms are completely general and can be applied to any interferometer, in the following we will always consider the MZ geometry; this is because it is one of the most common AI configurations employed for the measurement of inertial forces and because it is the one typically implemented in our experimental apparatus.

2.1 Atom-Light field interaction

2.1.1 Two-level atomic system and single-photon transitions

Let us consider a two-level atomic system in interaction with a monochromatic electric field. We recall that the two-level assumption is valid whenever the driving field is resonant or nearly resonant only with the atomic transition considered. With this assumption and in the so called dipole approximation, i.e. for field wavelengths

larger than the atomic size, the atomic system is formally analogous to a spin-1/2 particle interacting with a time dependent magnetic field. Indeed, as the magnetic field produces Rabi oscillations between the spin-up and spin-down states of the particle, the driving electromagnetic field will produce optical Rabi oscillations between the two atomic levels.

The mathematical analysis of the problem will be carried out with a semi-classical formalism. We start by writing the Hamiltonian for an electron (electronic charge e and mass m_e) interacting with an external electromagnetic field

$$\mathcal{H}_e = \frac{1}{2m_e}\left[\mathbf{p}_e - e\mathbf{A}(\mathbf{r}, t)\right]^2 + eU(\mathbf{r}, t) + V(r), \tag{2.1}$$

with $\mathbf{p}_e$ the electron momentum operator, $\mathbf{A}(\mathbf{r}, t)$ and $U(\mathbf{r}, t)$ the vector and scalar potentials of the driving field respectively and $V(r)$ the electron binding potential to the nucleus located in r_0. The functions $\mathbf{A}(\mathbf{r}, t)$ and $U(\mathbf{r}, t)$ are gauge-dependent potentials which are correlated to the gauge-independent electric and magnetic fields as

$$\mathbf{E}_l = -\nabla U - \frac{\partial \mathbf{A}}{\partial t}, \tag{2.2}$$
$$\mathbf{B}_l = \nabla \times \mathbf{A}.$$

If the entire atom is immersed in the electromagnetic wave, the vector potential can be written in the so called dipole approximation, valid when $\mathbf{k}_l \cdot \mathbf{r} \ll 1$ ($\mathbf{k}_l$ is the wave-vector of the electromagnetic field)

$$\mathbf{A}(\mathbf{r}_0 + \mathbf{r}, t) = \mathbf{A}(t)\exp[i\mathbf{k}_l \cdot (\mathbf{r}_0 + \mathbf{r})] \simeq \mathbf{A}(t)\exp(i\mathbf{k}_l \cdot \mathbf{r}_0). \tag{2.3}$$

In the radiation gauge in which $U(\mathbf{r}, t) = 0$ and $\nabla \cdot \mathbf{A} = 0$, the Schrödinger equation for the electron wave-function ψ_e becomes

$$\left[-\frac{\hbar^2}{2m_e}\left(\nabla - \frac{ie}{\hbar}\mathbf{A}(\mathbf{r}_0, t)\right)^2 + V(r)\right]\psi_e(\mathbf{r}, t) = i\hbar\frac{\partial \psi_e(\mathbf{r}, t)}{\partial t}. \tag{2.4}$$

The equation above can be simplified with the substitution

$$\psi_e(\mathbf{r}, t) = \exp\left[\frac{ie}{\hbar}\mathbf{A}(\mathbf{r}_0, t) \cdot \mathbf{r}\right]\varphi_e(\mathbf{r}, t).$$

With this new wave-function we obtain the Schrödinger equation

$$i\hbar\left[\frac{ie}{\hbar}\dot{\mathbf{A}} \cdot r\varphi_e(\mathbf{r}, t) + \dot{\varphi}_e(\mathbf{r}, t)\right]\exp\left(\frac{ie}{\hbar}\mathbf{A} \cdot \mathbf{r}\right)$$
$$= \exp\left(\frac{ie}{\hbar}\mathbf{A} \cdot \mathbf{r}\right)\left[\frac{p_e^2}{2m_e} + V(r)\right]\varphi_e(\mathbf{r}, t). \tag{2.5}$$

The equations above can be simplified by defining the unperturbed Hamiltonian $\mathcal{H}_0 = p_e^2/(2m_e) + V(r)$ which accounts only for the kinetic energy of the electron and the binding potential to the nucleus and by factoring out the common exponential factor. Using the results in Eq. 2.2 we obtain

$$i\hbar\dot{\varphi}_e(\mathbf{r}, t) = [\mathcal{H}_0 - e\mathbf{r} \cdot \mathbf{E}_l(\mathbf{r}_0, t)]\varphi_e(\mathbf{r}, t). \tag{2.6}$$

The complete Hamiltonian is the sum of two terms, $\mathcal{H}_e = \mathcal{H}_0 + \mathcal{H}_1$; $\mathcal{H}_0$ takes into account the electron evolution in the binding potential of the nucleus, while the atom-field interaction is considered in the term $\mathcal{H}_1$.

We now consider the interaction of a single mode of electromagnetic radiation with a two-level atom. The electric field with frequency ω_l can be written as

$$\mathbf{E}_l(\mathbf{x}, t) = \mathbf{E}_0 \cos(\mathbf{k}_l \cdot \mathbf{x} - \omega_l t + \phi_l). \tag{2.7}$$

We label the two atomic levels as $|a\rangle$ and $|b\rangle$ for the ground and excited state respectively; these two levels are eigenstates of the unperturbed Hamiltonian $\mathcal{H}_0$ with energy eigenvalues $\hbar\omega_a$ and $\hbar\omega_b$. The resonant transition frequency can be defined as $\omega_{ab} = \omega_b - \omega_a$. The frequency detuning between the exciting electric field and the resonant transition frequency is $\delta = \omega_l - \omega_{ab}$. Using the completeness relation $(|a\rangle\langle a| + |b\rangle\langle b|) = 1$ the Hamiltonian $\mathcal{H}_0$ can be written as

$$\mathcal{H}_0 = (|a\rangle\langle a| + |b\rangle\langle b|)\mathcal{H}_0(|a\rangle\langle a| + |b\rangle\langle b|) = \hbar\omega_a|a\rangle\langle a| + \hbar\omega_b|b\rangle\langle b|. \tag{2.8}$$

We continue to analyse the problem in the basis which takes into account both the external and internal atomic degrees of freedom [1], [44]; we will thus consider a continuous basis for the atomic momentum $|\mathbf{p}\rangle$ and a quantized basis for the atomic energy eigenstates $|a\rangle$ and $|b\rangle$. With the specified basis an atomic state will be expressed as a tensor product $|a, \mathbf{p}_1\rangle = |a\rangle \otimes |\mathbf{p}_1\rangle$ or $|b, \mathbf{p}_2\rangle = |b\rangle \otimes |\mathbf{p}_2\rangle$.

The complete Hamiltonian of the system can be written introducing the external atomic momentum operator $\mathbf{p}$ and the atomic dipole moment $\mathbf{d} = e\mathbf{r}$ as

$$\mathcal{H} = \frac{\mathbf{p}^2}{2m} + \hbar\omega_a|a\rangle\langle a| + \hbar\omega_b|b\rangle\langle b| - \mathbf{d} \cdot \mathbf{E}_l, \tag{2.9}$$

with m the atomic mass. Considering that

$$\exp(\pm i\mathbf{k}_l \cdot \mathbf{x}) = \int d^3\mathbf{p} \exp(\pm i\mathbf{k}_l \cdot \mathbf{x})|\mathbf{p}\rangle\langle \mathbf{p}| = \int d^3\mathbf{p}|\mathbf{p} \pm \hbar\mathbf{k}_l\rangle\langle \mathbf{p}|, \tag{2.10}$$

and Eqs. 2.7 and 2.9, we see that any event of photon absorption or stimulated emission is associated with a corresponding change in the external atomic momentum by a discrete amount $\pm\hbar\mathbf{k}_l$. Indeed we can identify a direct relationship between the internal and external states of the atomic system. It is then convenient to introduce the two eigenstates $|1\rangle$ and $|2\rangle$ defined as

$$|1\rangle = |a, \mathbf{p}\rangle \qquad\qquad E_1 = \hbar\omega_a + \frac{|p|^2}{2m} = \hbar\omega_1,$$

$$|2\rangle = |b, \mathbf{p} + \hbar\mathbf{k}_l\rangle \qquad E_2 = \hbar\omega_b + \frac{|p + \hbar k_l|^2}{2m} = \hbar\omega_2.$$

The atomic wave-function can be written as a linear superposition of the two defined eigenstates as

$$|\psi(t)\rangle = C_1(t)|1\rangle + C_2(t)|2\rangle, \tag{2.11}$$

where $C_{1,2}(t)$ are the amplitude probabilities of detecting the atom in state $|1\rangle$ or $|2\rangle$ at time t. The coefficients $C_{1,2}(t)$ can be split in two terms; one due to the interaction with the electric field and another one due to the free evolution of the atomic wave-function

$$C_1(t) = a_1(t)e^{-i\omega_1 t}, \qquad\qquad C_2(t) = a_2(t)e^{-i\omega_2 t}. \tag{2.12}$$

With these new coefficients the atomic state becomes

$$|\psi(t)\rangle = a_1(t)e^{-i\omega_1 t}|1\rangle + a_2(t)e^{-i\omega_2 t}|2\rangle. \tag{2.13}$$

This wave-function evolves according to the Hamiltonian 2.9 now defined as

$$\mathcal{H} = \hbar\omega_1|1\rangle\langle 1| + \hbar\omega_2|2\rangle\langle 2| - \mathbf{d}\cdot\mathbf{E}_l. \tag{2.14}$$

At this point it is useful to write the relevant frequencies as

$$\omega_0 = \omega_2 - \omega_1 = \omega_{ab} + \frac{\mathbf{p}\cdot\mathbf{k}_l}{m} + \frac{\hbar|\mathbf{k}_l|^2}{2m},$$

$$\Delta = \omega_l - \omega_0.$$

With these definitions and using the Schrödinger equation $i\hbar\frac{d}{dt}|\psi(t)\rangle = \mathcal{H}|\psi(t)\rangle$ we derive the following differential equations for the coefficients $a(t)$ in the rotating wave approximation [45]

$$\dot{a}_1 = -i\frac{\Omega}{2}e^{-i\phi_l}e^{i\Delta t}a_2(t),$$
$$\dot{a}_2 = -i\frac{\Omega^*}{2}e^{-i\phi_l}e^{-i\Delta t}a_1(t), \tag{2.15}$$

where Ω is the Rabi frequency defined as

$$\Omega = -\frac{\langle a|\mathbf{d}\cdot\mathbf{E}_0|b\rangle}{\hbar}. \tag{2.16}$$

The exact solution for the equations of motion of the coefficients $a_{1,2}$ can be written introducing the generalized Rabi frequency as

$$\Omega' = \sqrt{\Delta^2 + \Omega^2}. \tag{2.17}$$

With this definition we obtain

$$a_1(t) = e^{i\frac{\Delta}{2}t}\left\{a_1(0)\left[\cos\left(\frac{\Omega' t}{2}\right) - i\frac{\Delta}{\Omega'}\sin\left(\frac{\Omega' t}{2}\right)\right] + \right.$$
$$\left. a_2(0)e^{-i\phi_l}\left[-i\frac{\Omega}{\Omega'}\sin\left(\frac{\Omega' t}{2}\right)\right]\right\},$$
$$a_2(t) = e^{-i\frac{\Delta}{2}t}\left\{a_1(0)e^{i\phi_l}\left[-i\frac{\Omega}{\Omega'}\sin\left(\frac{\Omega' t}{2}\right)\right] + \right.$$
$$\left. a_2(0)\left[\cos\left(\frac{\Omega' t}{2}\right) + i\frac{\Delta}{\Omega'}\sin\left(\frac{\Omega' t}{2}\right)\right]\right\}. \tag{2.18}$$

From the equations above we can see that the probability of finding the atom in the ground state at time t, $\mathcal{P}_1 = |a_1(t)|^2$ or in the excited state $\mathcal{P}_2 = |a_2(t)|^2$, are oscillatory functions with frequency Ω' (see Fig. 2.1).

$$\mathcal{P}_1(t) = \left(\frac{\Omega}{\Omega'}\right)^2\frac{1 + \cos(\Omega' t)}{2},$$
$$\mathcal{P}_2(t) = \left(\frac{\Omega}{\Omega'}\right)^2\frac{1 - \cos(\Omega' t)}{2}. \tag{2.19}$$
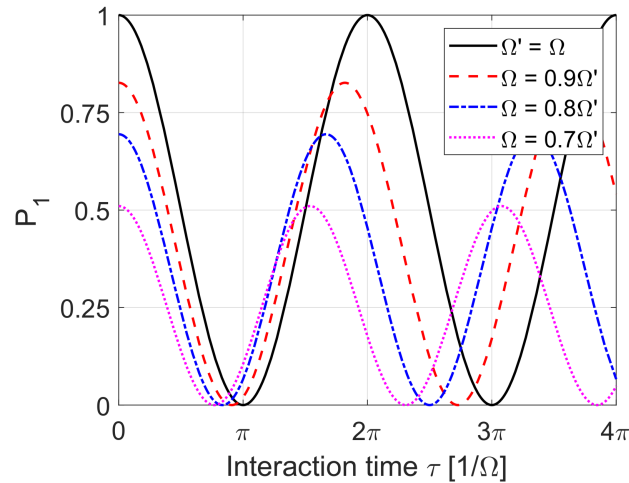
FIGURE 2.1: Behaviour of the atomic population in state $|1\rangle$ of a two-level atomic system in interaction with a monochromatic electric field as a function of the interaction time τ. The ideal case of perfect frequency matching ($\Delta = 0 \Rightarrow \Omega' = \Omega$) is shown with the black continuous line. In this case we observe complete population transfer between the two energy levels $|1\rangle$ and $|2\rangle$ with a frequency Ω. With the other colors we report the out of resonance cases in which $\Omega' \neq \Omega$.

The case of perfect frequency matching ($\Delta = 0$) is particularly interesting and easy to analyse. In this case we have

$$
\begin{aligned}
a_1(t) &= a_1(0) \cos\left(\frac{\Omega t}{2}\right) - i a_2(0) e^{-i\phi_l} \sin\left(\frac{\Omega t}{2}\right), \\
a_2(t) &= a_2(0) \cos\left(\frac{\Omega t}{2}\right) - i a_1(0) e^{i\phi_l} \sin\left(\frac{\Omega t}{2}\right).
\end{aligned}
\tag{2.20}
$$

From the two equations above we see that when a light pulse of temporal length τ is sent on an atom initially in state $|1\rangle$ (i.e. $a_1(0) = 1$, $a_2(0) = 0$), the final state will be

$$
|\psi(t)\rangle = \cos\left(\frac{\Omega\tau}{2}\right)|1\rangle + e^{-i\frac{\pi}{2}} e^{i\phi_l} \sin\left(\frac{\Omega\tau}{2}\right)|2\rangle.
\tag{2.21}
$$

From Eq. 2.21 we see that, as a function of the interaction time τ, there is a complete oscillation of the atomic population between the two states $|1\rangle$ and $|2\rangle$ with a frequency Ω. This particular behaviour is called optical Rabi oscillation (see black trace of Fig. 2.1).

It is now possible to define the formalism of the π and $\pi/2$ pulses. Considering again Eq. 2.21 we see that when $\tau = \pi/\Omega$ the atom will be transferred into state $|2\rangle$ with certainty; the complete population transfer defines the effect of a π pulse. Since every time that there is a transition between $|1\rangle$ and $|2\rangle$ there is a momentum exchange between atom and light field the pulse acts as a mirror for the wave-function (see Fig 2.2 right). On the contrary a $\pi/2$ pulse occurs when $\tau = \pi/(2\Omega)$; in this case the atom ends up in a linear superposition of the states $|1\rangle$ and $|2\rangle$ with equal amplitude probabilities. The pulse acts as a 50:50 beam-splitter for the wave-function on the two states $|1\rangle$ and $|2\rangle$ (see Fig 2.2 left).
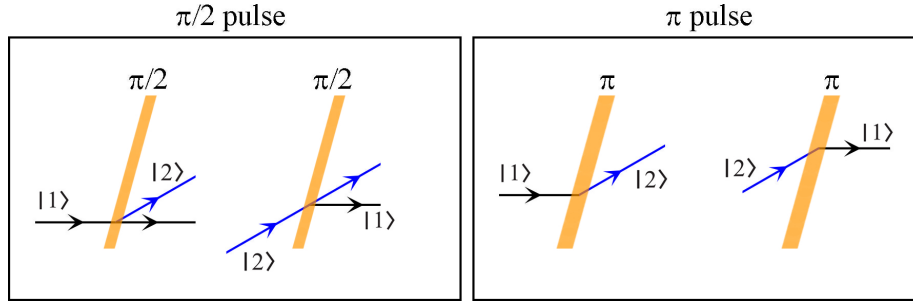
FIGURE 2.2: Effect of a $\pi/2$ and a π pulse when applied on the two-level system $|1\rangle$ and $|2\rangle$. The $\pi/2$ pulse can be considered as a 50:50 beam-splitter for the matter-wave, while the π pulse as a mirror.

The two defined pulses are what is needed to realize a complete atom interferometer. In our apparatus we employ a Mach-Zehnder interferometric geometry which can be realized with a $\pi/2 - \pi - \pi/2$ pulse sequence. First a $\pi/2$ pulse splits the atomic wave-function in two parts evolving independently along different paths[1]; after a time T a π pulse can be used to redirect the different paths towards each other; finally, after another time T a last $\pi/2$ pulse is applied to recombine the interferometric arms (see Fig. 1.1 right).

In a real atom only the ground state has an infinite lifetime. For this reason, in a real experiment the atomic level pair used in the AI is chosen in such a way that the ideal two-level system described so far can be considered a good approximation. For this to happen, the lifetime of the chosen level pair has to be orders of magnitude longer than the experimental times.

In our apparatus the AI is realized with ^{87}Rb atoms; for the manipulation of atomic Rubidium the most used transition is the optical D2 line manifold ($5^2S_{1/2} \rightarrow 5^2P_{3/2}$), which occur around 780.241 nm. This wavelength is easily accessible with standard laser diode technology, however the D2 line has a lifetime of 26 ns [46] which makes it impractical as a two-level system for AIs. However a good two-level system candidate is constituted by the doublet of the ground state hyperfine splitting. For these two levels the energy splitting falls in the microwave range at around 6.8 GHz. Using a microwave to directly address this transition and realize the interferometer is a possible and commonly adopted solution. However since the momentum transfer associated to a microwave photon is extremely low (transferred velocity of 10^{-4} mm/s) this scheme is used only when the momentum separation between the interferometric arms is not desired, e.g. in fountain clock experimental schemes. In our case achieving a high momentum separation between the interferometric arms is fundamental. Indeed, when an atom interferometer is used as an inertial sensor, its sensitivity is directly proportional to the momentum imparted on the atoms; this rules out the possibility of using a microwave pulse to realize the interferometric transitions.

A viable and largely exploited solution is represented by Raman transitions or other multi-photon processes which are able to both couple the ^{87}Rb hyperfine states and transfer momentum in the optical photon range. As we will see in the next section Raman transitions are realized with two counter-propagating light beams

---

[1]The two paths define the interferometric branches or interferometric arms. The branches can be separated on the atomic external and internal degrees of freedom (like in the case of Raman atom interferometers) or only on one of these two degrees of freedom (like in the case of Bragg interferometers where only a momentum separation between the arms is obtained).

with a relative detuning which equals the ground state hyperfine splitting. They allow to consider the ground state hyperfine doublet as a good two-level system and they can transfer twice an optical momentum (two-photon recoil velocity of $2v_r = 11.8$ mm/s).

In the next section we present the theory of two-photon Raman transitions, while in Sec. 2.1.3 we introduce multi-photon Bragg transitions.

2.1.2 Two-photon Raman transitions

We now consider a three-level atomic system with two main energy levels, $|a\rangle$ and $|b\rangle$ and an excited virtual level $|i\rangle$. In the case of ^{87}Rb the levels $|a\rangle$ and $|b\rangle$ are the two hyperfine levels with $F = 1$ and $F = 2$ of the $5^2S_{1/2}$ ground state, while the state $|i\rangle$ can be considered as the superposition of all the hyperfine levels of the excited $5^2P_{3/2}$ state.

As anticipated in the previous section, we consider the interaction of the atomic system with two counter-propagating light beams

$$
\begin{aligned}
\mathbf{E}_{l1}(x,t) &= \mathbf{E}_{l1,0}\cos[\mathbf{k}_{l1} \cdot \mathbf{x} - \omega_{l1}t + \phi_{l1}], \\
\mathbf{E}_{l2}(x,t) &= \mathbf{E}_{l2,0}\cos[\mathbf{k}_{l2} \cdot \mathbf{x} - \omega_{l2}t + \phi_{l2}],
\end{aligned}
\tag{2.22}
$$

with frequencies ω_{l1} and ω_{l2}.

Like in the case of single-photon transitions we will use a basis of coupled external and internal atomic degrees of freedom. We consider the following states

$$
\begin{aligned}
|1\rangle &= |a, \mathbf{p}\rangle & E_1 &= \hbar\omega_a + \frac{|p|^2}{2m} = \hbar\omega_1, \\
|2\rangle &= |b, \mathbf{p} + \hbar\mathbf{k}_{l1} - \hbar\mathbf{k}_{l2}\rangle & E_2 &= \hbar\omega_b + \frac{|p + \hbar\mathbf{k}_{l1} - \hbar\mathbf{k}_{l2}|^2}{2m} = \hbar\omega_2, \\
|i0\rangle &= |i, \mathbf{p} + \hbar\mathbf{k}_{l1}\rangle & E_{i0} &= \hbar\omega_c + \frac{|p + \hbar\mathbf{k}_{l1}|^2}{2m} = \hbar\omega_{i0}, \\
|i1\rangle &= |i, \mathbf{p} + 2\hbar\mathbf{k}_{l1} - \hbar\mathbf{k}_{l2}\rangle & E_{i1} &= \hbar\omega_c + \frac{|p + 2\hbar\mathbf{k}_{l1} - \hbar\mathbf{k}_{l2}|^2}{2m} = \hbar\omega_{i1}, \\
|i2\rangle &= |i, \mathbf{p} + \hbar\mathbf{k}_{l2}\rangle & E_{i2} &= \hbar\omega_c + \frac{|p + \hbar\mathbf{k}_{l2}|^2}{2m} = \hbar\omega_{i2}.
\end{aligned}
$$

States $|1\rangle$ and $|2\rangle$ are the fundamental states which are coupled by the Raman transition. Starting from the state $|1\rangle$, state $|2\rangle$ is reached with the absorption of one photon from the field $\mathbf{E}_{l1}$ and the stimulated emission of a photon in the field $\mathbf{E}_{l2}$. The other three states are the ones in which the atom can be transferred into if starting from one of the main levels and interacting with one of the two light fields. $|i0\rangle$ corresponds to the absorption of a photon from $\mathbf{E}_{l1}$ when the atom is in $|1\rangle$ or to the absorption of a photon from $\mathbf{E}_{l2}$ when the atom is in $|2\rangle$. State $|i1\rangle$ corresponds to the absorption of a photon from $\mathbf{E}_{l1}$ when the atom is in $|2\rangle$, and finally state $|i2\rangle$ is reached when the atom in $|1\rangle$ absorbs a photon from $\mathbf{E}_{l2}$. We note that the momentum transfer associated with the transition $|1\rangle \rightarrow |2\rangle$ is $\hbar|\mathbf{k}_{l1} - \mathbf{k}_{l2}| \simeq 2\hbar k_{l1}$, i.e. two optical photons momentum since the two light beams are counter-propagating.

The wave-function of the atomic system can be written as the linear superposition

$$
|\psi(t)\rangle = \sum_s a_s(t)e^{-i\omega_s t}|s\rangle,
\tag{2.23}
$$

where s represents the five energy levels considered. The evolution of the atomic
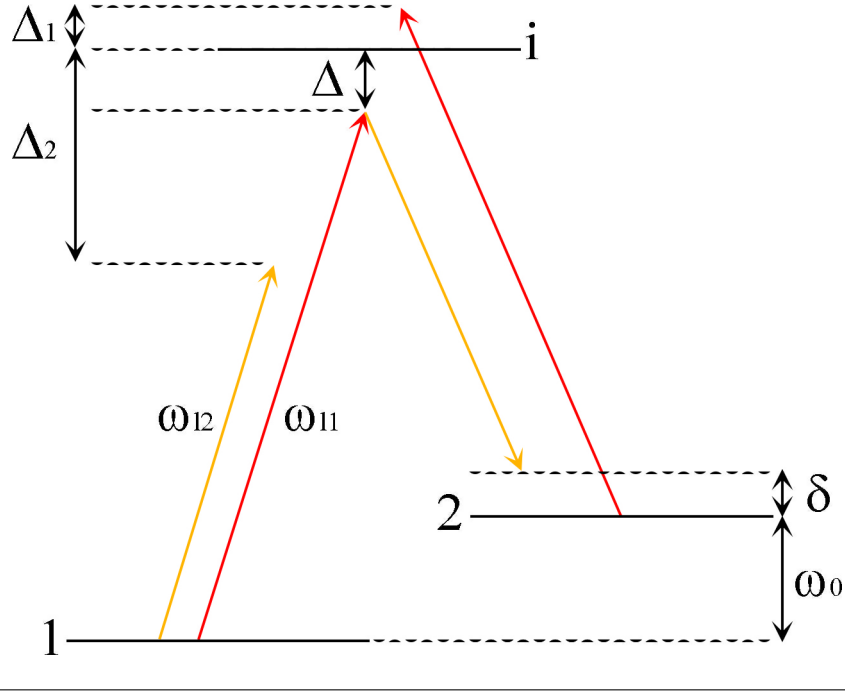
FIGURE 2.3: Schematic diagram of the atomic energy levels involved in a Raman transition. Two light field of frequencies ω_{l1} and ω_{l2} couple the two ground hyperfine states $|1\rangle$ and $|2\rangle$.

wave-function is regulated by the Hamiltonian (see Eq. 2.14)

$$\mathcal{H} = \sum_s \hbar\omega_s |s\rangle\langle s| - \mathbf{d} \cdot (\mathbf{E}_{l1} + \mathbf{E}_{l2}),\qquad(2.24)$$

where $\mathbf{d}$ is again the electric dipole moment.

We now define some frequencies of interest (see Fig. 2.3): $\omega_0 = \omega_2 - \omega_1$ is the atomic resonance frequency, $\delta = (\omega_{l1} - \omega_{l2}) - \omega_0$ is the detuning of the light fields from the atomic resonance, Δ is the common detuning from the excited state $|i0\rangle$, while Δ_1 and Δ_2 are respectively the detuning of the light field $\mathbf{E}_{l1}$ from the transition $|2\rangle \rightarrow |i0\rangle$ and of the light field $\mathbf{E}_{l2}$ from the transition $|1\rangle \rightarrow |i0\rangle$.

Considering the coupling between the states $|m\rangle$ ($m = 1$, 2) and the states $|n\rangle$ ($n = i0$, $i1$, $i2$) induced by the laser fields $j = 1$, 2, we can define the Rabi frequency as

$$\Omega_{mn,j} = \frac{\langle n| - \mathbf{d} \cdot \mathbf{E}_{lj,0}|m\rangle}{\hbar}.\qquad(2.25)$$

Applying the Schrödinger equation to the wave-function 2.23 with the Hamiltonian 2.24 we obtain the following equations of motion for the coefficients a_s in the rotating

wave approximation

$$i\dot{a}_1(t) = a_{i0}(t)\frac{\Omega_{1i0,1}^*}{2}e^{i(\Delta t - \phi_{l1})} + a_{i2}(t)\frac{\Omega_{1i2,2}^*}{2}e^{i(\Delta_2 t - \phi_{l2})},$$

$$i\dot{a}_2(t) = a_{i0}(t)\frac{\Omega_{2i0,2}^*}{2}e^{i(\Delta t - \delta t - \phi_{l2})} + a_{i1}(t)\frac{\Omega_{2i1,1}^*}{2}e^{i(\Delta_1 t - \phi_{l1})},$$

$$i\dot{a}_{i0}(t) = a_1(t)\frac{\Omega_{1i0,1}}{2}e^{i(-\Delta t + \phi_{l1})} + a_2(t)\frac{\Omega_{2i0,2}}{2}e^{i(-\Delta t + \delta t + \phi_{l2})},$$

$$i\dot{a}_{i1}(t) = a_2(t)\frac{\Omega_{2i1,1}}{2}e^{i(-\Delta_1 t + \phi_{l1})},$$

$$i\dot{a}_{i2}(t) = a_1(t)\frac{\Omega_{1i2,2}}{2}e^{i(-\Delta_2 t + \phi_{l2})}.$$

It is possible to demonstrate that the coefficients of the excited levels oscillate with frequency Δ while the coefficients of the main levels vary much more slowly. We can therefore adiabatically eliminate the three excited levels [47] by integrating the three corresponding differential equations considering a_1 and a_2 constant. We then obtain

$$i\dot{a}_1(t) = a_1(t)\left[\frac{|\Omega_{1i0,1}|^2}{4\Delta} + \frac{|\Omega_{1i2,2}|^2}{4\Delta_2}\right] + a_2(t)\left[\frac{\Omega_{1i0,1}^*\Omega_{2i0,2}}{4(\Delta-\delta)}\exp[-i(\phi_{l1}-\phi_{l2}) + i\delta t]\right],$$

$$i\dot{a}_2(t) = a_1(t)\left[\frac{\Omega_{2i0,2}^*\Omega_{1i0,1}}{4\Delta}\exp[i(\phi_{l1}-\phi_{l2}) - i\delta t]\right] + a_2(t)\left[\frac{|\Omega_{2i0,2}|^2}{4(\Delta-\delta)} + \frac{|\Omega_{2i1,1}|^2}{4\Delta_1}\right].$$

The equations above can be simplified and made similar to those obtained in Sec. 2.1.1 by defining the frequency light shifts of the two main states as

$$\Omega_1^{AC} = \left[\frac{|\Omega_{1i0,1}|^2}{4\Delta} + \frac{|\Omega_{1i2,2}|^2}{4\Delta_2}\right],$$
$$\Omega_2^{AC} = \left[\frac{|\Omega_{2i0,2}|^2}{4(\Delta-\delta)} + \frac{|\Omega_{2i1,1}|^2}{4\Delta_1}\right], \tag{2.26}$$

and the effective quantities

$$\omega_{\text{eff}} = \omega_{l1} - \omega_{l2},$$
$$\mathbf{k}_{\text{eff}} = \mathbf{k}_{l1} - \mathbf{k}_{l2},$$
$$\phi^0 = \phi_{l1} - \phi_{l2},$$
$$\Omega_{\text{eff}} = \frac{\Omega_{1i0,1}\Omega_{2i0,2}}{2\Delta},$$
$$\Omega_{\text{eff}}' = \sqrt{\Omega_{\text{eff}}^2 + (\delta - \delta^{AC})^2}.$$

We can then also define the total light shift $\Omega^{AC} = \Omega_1^{AC} + \Omega_2^{AC}$ and the differential light shift $\delta^{AC} = \Omega_2^{AC} - \Omega_1^{AC}$. Finally, considering that $\delta \ll \Delta$ we can write

$$i\dot{a}_1(t) = a_1(t)\Omega_1^{AC} + a_2(t)\frac{\Omega_{\text{eff}}^*}{2}e^{-i\phi^0}e^{i\delta t},$$
$$i\dot{a}_2(t) = a_1(t)\frac{\Omega_{\text{eff}}^*}{2}e^{i\phi^0}e^{-i\delta t} + a_2(t)\Omega_2^{AC}. \tag{2.27}$$

It is now convenient to remove the time dependence of the off-diagonal terms with the rotation of the coefficients

$$a_1(t) = c_1(t) \exp\left(i\frac{\delta - \Omega^{AC}}{2}t\right), \qquad a_2(t) = c_2(t) \exp\left(-i\frac{\delta + \Omega^{AC}}{2}t\right),$$

which produces the differential equations

$$
\begin{aligned}
i\dot{c}_1(t) &= \frac{1}{2}\left[c_1(t)(\delta - \delta^{AC}) + s_2(t)\Omega_{\text{eff}}e^{-i\phi^0}\right], \\
i\dot{c}_2(t) &= \frac{1}{2}\left[c_1(t)\Omega_{\text{eff}}e^{i\phi^0} - s_2(t)(\delta - \delta^{AC})\right].
\end{aligned}
\tag{2.28}
$$

From the solution of the equations above we derive the expression for the original coefficients of the wave-function as

$$
\begin{aligned}
a_1(t) &= e^{i(\delta - \Omega^{AC})t/2}\left[a_1(0)\left(\cos\left(\frac{\Omega'_{\text{eff}}t}{2}\right) - i\frac{\delta - \delta^{AC}}{\Omega'_{\text{eff}}}\sin\left(\frac{\Omega'_{\text{eff}}t}{2}\right)\right) + \right. \\
&\qquad \left. a_2(0)e^{-i\phi^0}\left(-i\frac{\Omega_{\text{eff}}}{\Omega'_{\text{eff}}}\sin\left(\frac{\Omega'_{\text{eff}}t}{2}\right)\right)\right], \\
a_2(t) &= e^{-i(\delta + \Omega^{AC})t/2}\left[a_1(0)e^{i\phi^0}\left(-i\frac{\Omega_{\text{eff}}}{\Omega'_{\text{eff}}}\sin\left(\frac{\Omega'_{\text{eff}}t}{2}\right)\right) + \right. \\
&\qquad \left. a_2(0)\left(\cos\left(\frac{\Omega'_{\text{eff}}t}{2}\right) + i\frac{\delta - \delta^{AC}}{\Omega'_{\text{eff}}}\sin\left(\frac{\Omega'_{\text{eff}}t}{2}\right)\right)\right].
\end{aligned}
\tag{2.29}
$$

In Tab. 2.1 we report the momentum transfers and phase shifts associated to each transition, as derived from Eqs. 2.29. The phase term θ^0 stands for the phase of the complex factor $\left[\cos\left(\frac{\Omega'_{\text{eff}}t}{2}\right) - i\frac{\delta - \delta^{AC}}{\Omega'_{\text{eff}}}\sin\left(\frac{\Omega'_{\text{eff}}t}{2}\right)\right]$ which takes into account the effect of the differential light-shift δ^{AC}.

The equations above can be simplified since experimentally it is possible to have $\delta, \delta^{AC} \ll \Omega_{\text{eff}}$. We can thus write

$$
\begin{aligned}
a_1(t) &= e^{i(\delta - \Omega^{AC})t/2}\left[a_1(0)\cos\left(\frac{\Omega_{\text{eff}}t}{2}\right) - ia_2(0)e^{-i\phi^0}\sin\left(\frac{\Omega_{\text{eff}}t}{2}\right)\right], \\
a_2(t) &= e^{-i(\delta + \Omega^{AC})t/2}\left[a_2(0)\cos\left(\frac{\Omega_{\text{eff}}t}{2}\right) - ia_1(0)e^{i\phi^0}\sin\left(\frac{\Omega_{\text{eff}}t}{2}\right)\right].
\end{aligned}
\tag{2.30}
$$

The two equations above are similar to those obtained in Sec. 2.1.1 (see Eqs. 2.20). Also for a Raman transition is therefore possible to define the formalism of the $\pi/2$ and π pulses. Indeed, if we consider an initial state such that $a_1(0) = 1$ and $a_2(0) = 0$, when $|\Omega_{\text{eff}}|\tau = \pi/2$ we achieve a coherent equi-probable superposition of the two hyperfine states; on the contrary if we consider a pulse such that $|\Omega_{\text{eff}}|\tau = \pi$ we obtain a complete population transfer between the two main states and a momentum transfer of $\hbar k_{\text{eff}} \simeq 2k_{l1}$, i.e. twice the momentum of an optical photon.

As we will see in Sec. 2.2 the interferometer phase shift and consequently the interferometer sensitivity to inertial effects is proportional to the momentum imparted on the atoms. It is therefore important to devise strategies to increase the transferred momentum; this can be done implementing atom-optical techniques different from Raman transitions which fall in the category of Large Momentum Transfer (LMT)

TABLE 2.1: Momentum transfers and phase shifts as derived from Eqs. 2.29.

Transition	Momentum	Phase shift
$\lvert a \rangle \to \lvert a \rangle$	$\lvert \mathbf{p} \rangle \to \lvert \mathbf{p} \rangle$	$\theta^0 + \frac{(\delta - \Omega^{AC})\tau}{2}$
$\lvert a \rangle \to \lvert b \rangle$	$\lvert \mathbf{p} \rangle \to \lvert \mathbf{p} + \hbar \mathbf{k_{eff}} \rangle$	$-\frac{(\delta + \Omega^{AC})\tau}{2} + \phi^0 - \frac{\pi}{2}$
$\lvert b \rangle \to \lvert a \rangle$	$\lvert \mathbf{p} + \hbar \mathbf{k_{eff}} \rangle \to \lvert \mathbf{p} \rangle$	$\frac{(\delta - \Omega^{AC})\tau}{2} - \phi^0 - \frac{\pi}{2}$
$\lvert b \rangle \to \lvert b \rangle$	$\lvert \mathbf{p} + \hbar \mathbf{k_{eff}} \rangle \to \lvert \mathbf{p} + \hbar \mathbf{k_{eff}} \rangle$	$-\theta^0 - \frac{(\delta + \Omega^{AC})\tau}{2}$

processes. The next section analyses one of these processes, i.e. atomic Bragg diffraction.

2.1.3 Multi-photon Bragg transitions

We now theoretically examine the atomic Bragg diffraction process. The results derived and presented here can be found and extended in [40], [41], [48]. In the last part of this section we also provide numerical solutions for the atomic population dynamics during Bragg transitions.

The phenomenon of Bragg diffraction was first formulated in 1913, by W. H. Bragg and W. L. Bragg [49], who noted that some crystalline substances produced peculiar and reproducible diffraction patterns when irradiated with X-ray light. From these experimental observations the authors concluded that the observed diffraction peaks were profoundly linked to the internal atomic structure of the irradiated crystal and, in particular, to the separation between the lattice planes. The final result of Bragg's analysis is the famous diffraction condition

$$n\lambda = 2d \sin\theta, \tag{2.31}$$

where λ is the wavelength of the electromagnetic field, d the distance between neighbouring lattice planes, θ the incidence angle of the radiation with respect to the normal of the lattice planes and n the diffraction order. In the ideal case of a three-dimensional, infinite, perfect lattice if the condition 2.31 is fulfilled for a certain diffraction order n, all the radiation incident on the crystal is redirected in that particular order of diffraction. An ideal diffraction process can therefore produce only one order of diffraction n, identified by the incidence angle of the wave-front with respect to the normal of the lattice planes.

In our case the role between matter and light is exchanged since the diffraction phenomenon is stimulated on an atomic wave-function with the use of an optical lattice. The interaction time is not dependent on the spatial extension of the lattice any more, but on the duration of the light pulses. Moreover, the condition on the incidence angle in relation 2.31 translates in a condition on the frequency difference for the two laser beams forming the lattice, i.e. on the velocity of the wave pattern.

For an atomic system, a Bragg diffraction process of order n can be interpreted as a $2n$-photon transition which couples two defined, different momentum states, leaving the internal state untouched. If the stationary wave pattern is produced by two counter-propagating laser beams with slightly different frequencies the process consists in the absorption of n photons from one of the beams and in the successive stimulated emission of n photons in the counter-propagating beam. If k is the wave-number associated to the wave pattern, the process is then able to determine
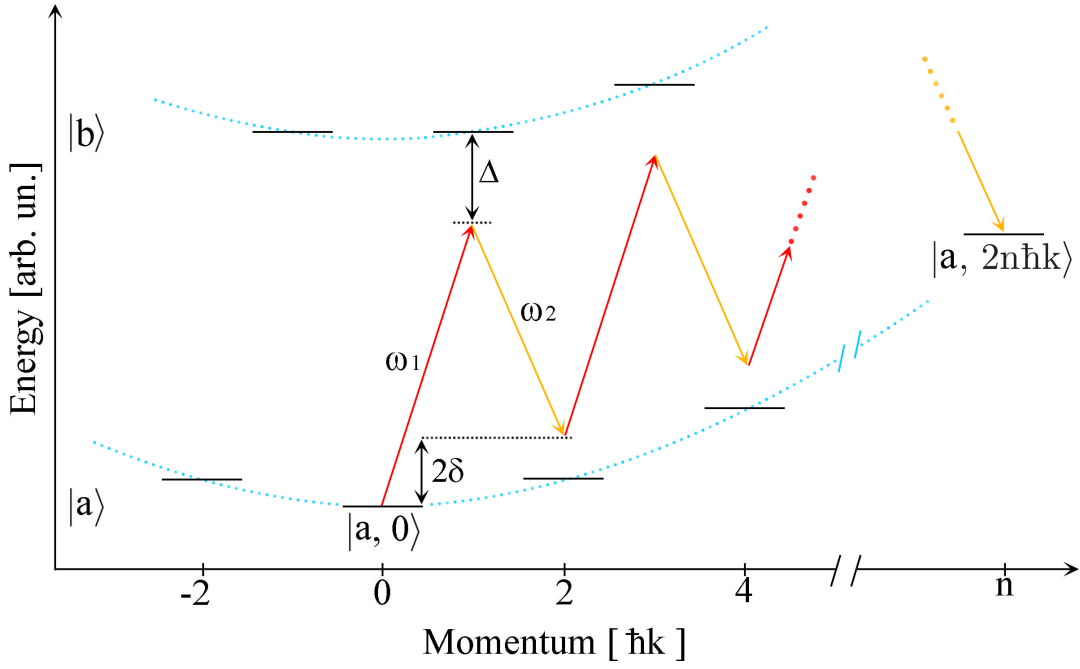
FIGURE 2.4: Energy level diagram for a Bragg diffraction process of nth order. The transition connects the state $|a,0\rangle$ to $|a,np_{\text{rec}}\rangle$, with $p_{\text{rec}} = 2\hbar k$. $|a\rangle$ and $|b\rangle$ are two internal atomic states, ω_1 and ω_2 indicate the frequencies of the two laser beams used to generate the diffracting one-dimensional wave pattern. The parabolic frequency arrangement of the different vibrational levels, following the trend $\sim n^2\omega_r$, is indicated in light blue.

a total momentum transfer of $k_{\text{eff}} = 2n\hbar k$, while the internal atomic state remains unchanged.

Fig. 2.4 shows the transition diagram for a Bragg process of order n, connecting the two states $|a, 2n_I\hbar k\rangle \rightarrow |a, 2n_F\hbar k\rangle$, where in this specific case $n_I = 0$ and $n_F = 3$. The excited diffraction order is therefore $n = n_F - n_I = 3$ and the laser fields have a relative detuning of 2δ. The atom, after the diffraction, remains in the same internal state $|a\rangle$, but acquires a kinetic energy of $4\hbar\omega_r(n_F^2 - n_I^2)$ (with $\omega_r = \hbar k^2/(2m)$ the recoil frequency and m the atomic mass). The kinetic energy acquired has to balance the energy lost by the laser field, i.e. $2\hbar(n_F - n_I)\delta$. From these two relations we can derive the resonance condition for a general Bragg transition connecting the momentum states $|2n_I\hbar k\rangle$ and $|2n_F\hbar k\rangle$ as

$$\delta = 2\omega_r(n_F + n_I). \tag{2.32}$$

In our case the level $|a\rangle$ corresponds to the ^{87}Rb hyperfine state $|F = 1, m_F = 0\rangle$ of the ground level, while $|b\rangle$ is the superposition of all the hyperfine levels of the excited state $5^2P_{3/2}$.

In Sec. 2.1.1 we already considered the interaction of an atomic two-level system with a mono-chromatic electromagnetic field of frequency ω_l and wave-vector $\mathbf{k}_l$. Labelling the two atomic energy levels as $|a\rangle$ and $|b\rangle$ (for the fundamental and excited level respectively) and the transition frequency $\omega_0 = \omega_b - \omega_a$, we recall here that the Hamiltonian in the rotating wave approximation can be written as [41]

$$\mathcal{H} = \frac{p^2}{2m} + \hbar\omega_0|b\rangle\langle b| - \left(\frac{\hbar\Omega}{2}e^{i(kz-\omega_l t)}|b\rangle\langle a| + h.c.\right), \tag{2.33}$$

where the Rabi frequency is now defined as $\Omega = \mathbf{d} \cdot \mathbf{E}_0 / \hbar$. This result can be modified for a superposition of plane waves. Indeed considering a generalized electric field

$$\mathbf{E} = \sum_j \mathbf{E}_j \cos(k_j z - (\omega_l - \delta_j)t), \qquad (2.34)$$

the Hamiltonian can be written as

$$\mathcal{H} = \frac{p^2}{2m} + \hbar(\omega_0 - \omega_l)|b\rangle\langle b| - \hbar\left(\sum_j \frac{\Omega_j}{2} e^{i(k_j z + \delta_j t)} |b\rangle\langle a| + h.c. \right), \qquad (2.35)$$

The Hamiltonian above describes the interaction of any atomic two-level system with an arbitrary electric field. When considering the special case of Bragg diffraction the atoms are scattered by a one dimensional optical lattice derived from two counter-propagating light beams; we thus have

$$\mathbf{E} = \frac{\mathbf{E}_0}{2} u(z, t) = \frac{\mathbf{E}_0}{2} \left[e^{-i(kz - \delta t)} + e^{i(kz - \delta t)} \right], \qquad (2.36)$$

where 2δ is the detuning between the counter-propagating laser beams. The Hamiltonian becomes ($\Delta = \omega_0 - \omega_l$)

$$\mathcal{H} = \frac{p^2}{2m} - \hbar\Delta|b\rangle\langle b| - \left(\frac{\Omega u(z, t)}{2} |b\rangle\langle a| + h.c. \right). \qquad (2.37)$$

For the atomic wave-function we consider the superposition

$$|\psi\rangle = a(z, t)|a\rangle + b(z, t)|b\rangle, \qquad (2.38)$$

and use it in the Schrödinger equation relative to the Hamiltonian 2.37. The result is the system of coupled differential equations

$$i\hbar\dot{a}(z, t) = \frac{p^2}{2m} a(z, t) - \frac{\hbar\Omega^*}{2} u^* b(z, t),$$

$$i\hbar\dot{b}(z, t) = \frac{p^2}{2m} b(z, t) - \hbar\Delta b(z, t) - \frac{\hbar\Omega}{2} u a(z, t).$$

The excited state dynamics can be adiabatically eliminated by setting $\dot{b}(z, t) = 0$ since the laser detuning $\Delta \gg \Omega$. Then

$$i\dot{a}(z, t) = -\frac{\hbar}{2m} \frac{\partial^2}{\partial z^2} a(z, t) + \frac{|\Omega|^2}{4\Delta} u u^* a(z, t). \qquad (2.39)$$

We note that due to the electric field periodicity we can apply Bloch's theorem and express $a(z, t)$ as a superposition of plane waves[2]

$$a(z, t) = \sum_{n=-\infty}^{\infty} a_n(t) e^{i2nkz} e^{-i(2n)^2 \omega_r t}.$$

---

[2]In the expression for $a(z, t)$ we include also a kinetic energy phase factor. This contribution, even if not strictly needed is included to reduce the complexity of the final solution.

Substituting the above plane-wave decomposition into Eq. 2.39 and defining the two-photon Rabi frequency $\Omega' = |\Omega|^2/(2\Delta)$ we obtain

$$\sum_{n=-\infty}^{\infty} i\dot{a}_n e^{i2nkz} e^{-i4n^2\omega_r t} = \Omega' \sum_{n=-\infty}^{\infty} a_n e^{i2nkz} e^{-i4n^2\omega_r t} +$$
$$\frac{\Omega'}{2}\left[\sum_{n=-\infty}^{\infty} a_n e^{i2(n-1)kz} e^{i2\delta t} e^{-i4n^2\omega_r t} + \sum_{n=-\infty}^{\infty} a_n e^{i2(n+1)kz} e^{-i2\delta t} e^{-i4n^2\omega_r t}\right]. \tag{2.40}$$

The equation above can be simplified by going into the frame rotating at the frequency Ω', i.e. with the substitution $a_n \to a_n e^{-i\Omega' t}$. We also introduce the substitutions $(n-1) \to n$ and $(n+1) \to n$ in the left and right summations respectively. We thus obtain

$$\sum_{n=-\infty}^{\infty} i\dot{a}_n e^{i2nkz} e^{-i4n^2\omega_r t} = \frac{\Omega'}{2}\left[\sum_{n=-\infty}^{\infty} a_{n+1} e^{i2nkz} e^{i2\delta t} e^{-i4(n+1)^2\omega_r t} + \sum_{n=-\infty}^{\infty} a_{n-1} e^{i2nkz} e^{-i2\delta t} e^{-i4(n-1)^2\omega_r t}\right].$$

We note that in the equation above each term is multiplied by e^{i2nkz}, but since the solution a_n has to be valid for all z, each term of order e^{i2nkz} has to be equal individually, i.e.

$$i\dot{a}_n = \frac{\Omega'}{2}\left[a_{n+1} e^{i2\delta t} e^{-i4(2n+1)\omega_r t} + a_{n-1} e^{-i2\delta t} e^{i4(2n-1)\omega_r t}\right]. \tag{2.41}$$

We thus obtain an infinite set of coupled differential equations indexed by the integer n which describe the population dynamics in the different momentum states coupled by the laser field. In general the two-photon Rabi frequency is a function of the time t. We note that Eq. 2.41 produces a coupling between the different plane-wave momentum states of the atom only by integer multiples of the photon wave-number k.

The system 2.41 cannot be treated analytically; however we can consider simplifying assumptions and some special cases in which simple solutions can be found analytically. For example when the interaction time $t \to 0$ Eq. 2.41 simplifies to

$$i\dot{a}_n = \frac{\Omega'}{2}\left[a_{n+1} + a_{n-1}\right], \tag{2.42}$$

and we are in the so called Raman-Nath regime. Solutions of the equation above can be expressed in terms of Bessel functions $\mathcal{J}_n$ as

$$a_n = (-i)^n \mathcal{J}_n(4\Omega' t).$$

Bragg diffraction processes in the Raman-Nath regime can be used in atom interferometry to realize beam-splitters [50]; however the atomic population tends to be diffracted in many momentum states and not just the two of interest. This problem severely limits the applicability of Raman-Nath beam-splitters.

An efficient beam-splitter, coupling only two momentum states can be obtained when the interaction time is long ($\tau \gg 1/\omega_r$), i.e. in the so called Bragg regime. In the particular case in which $\delta = 0$ energy conservation favors the transitions $a_{-n} \to a_n$ and all the intermediate states a_m ($m \neq \pm n$) can be adiabatically eliminated from the population dynamics. The evolution of the remaining two-level system is governed by the effective Rabi frequency [40]

$$\Omega_{\text{eff}} = \frac{(\Omega')^n}{(8\omega_r)^{(n-1)}} \frac{1}{[(n-1)!]^2}. \tag{2.43}$$

The adiabatic elimination of the intermediate states can be performed as long as the condition $4(n-1)\omega_r \gg \Omega'$ is satisfied. The same condition can be expressed as

$$\Omega_{\text{eff}} \ll \frac{8(n-1)^n}{2^n[(n-1)!]^2}\omega_r. \tag{2.44}$$

For $n \leq 5$ the second term of the expression above is $\sim \omega_r$ (i.e. the Bragg condition is satisfied for interaction times $\Omega_{\text{eff}}^{-1} \ll \omega_r^{-1}$), but it drops rapidly with increasing n. The general Bragg resonance condition to transfer atoms between the momentum states n_I and n_F reads $\delta = 2\omega_r(n_F + n_I)$.

We point out that in our set-up the conditions for the Bragg regime are not met. The transitions are stimulated with Gaussian pulses with $\sigma = 12\,\mu s$ (FWHM $\simeq 28\,\mu s$), i.e. with a duration comparable with the inverse of the ^{87}Rb recoil frequency $\omega_r^{-1} \simeq 42\,\mu s$. However a quasi-Bragg solution of the system 2.41, which can describe typical experimental conditions, can be derived numerically. If we consider the resonant coupling of the momentum states a_{nI} and a_{nF}, i.e. if we consider a detuning $\delta = 2(n_F + n_I)\omega_r$, we can introduce an upper and a lower index cutoff, respectively $n_1 > \max(n_I, n_F)$ and $-n_2 < \min(n_I, n_F)$, which permits the reduction of the infinite system 2.41 to a finite system of differential equations

$$
\begin{aligned}
i\dot{a}_{n_1+1} &= 0, \\
i\dot{a}_{n_1} &= \frac{\Omega'}{2}\left[a_{n_1-1}e^{-i2\delta t}e^{i4(2n_1-1)\omega_r t}\right], \\
i\dot{a}_{n_1-1} &= \frac{\Omega'}{2}\left[a_{n_1}e^{i2\delta t}e^{-i4(2n_1-1)\omega_r t} + a_{n_1-2}e^{-i2\delta t}e^{i4(2n_1-3)\omega_r t}\right], \\
&\;\;\vdots \\
i\dot{a}_n &= \frac{\Omega'}{2}\left[a_{n+1}e^{i2\delta t}e^{-i4(2n+1)\omega_r t} + a_{n-1}e^{-i2\delta t}e^{i4(2n-1)\omega_r t}\right], \\
&\;\;\vdots \\
i\dot{a}_{-n_2+1} &= \frac{\Omega'}{2}\left[a_{-n_2+2}e^{i2\delta t}e^{-i4(-2n_2+3)\omega_r t} + a_{-n_2}e^{-i2\delta t}e^{i4(-2n_2+1)\omega_r t}\right], \\
i\dot{a}_{-n_2} &= \frac{\Omega'}{2}\left[a_{-n_2+1}e^{i2\delta t}e^{-i4(-2n_2+1)\omega_r t}\right], \\
i\dot{a}_{-n_2-1} &= 0.
\end{aligned}
\tag{2.45}
$$

This system of differential equations can be solved numerically with standard computing software. In the following we present some numerical results derived from the equations above.

Let us now consider again the Bragg diffraction process reported in Fig. 2.4. We note that in order to reach the desired final momentum state the atom has to go through several processes of photon absorption and stimulated emission which allow it to ascend the momentum states ladder. For an efficient Bragg diffraction process, all the intermediate momentum states encountered before the target state must remain unpopulated. This requirement is highly important especially in atom interferometry since the parasitic phase imparted on the atoms by the Bragg beamsplitters is proportional to the amount of losses in the intermediate momentum states [40]. As we already mentioned when describing the Bragg regime, one way to satisfy this requirement is to use long Bragg pulses. However the pulse length needed is outside of our experimental possibilities. Fortunately it is possible to reduce the
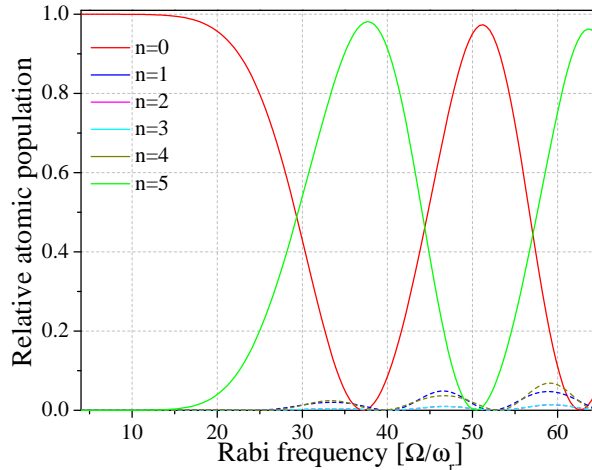
FIGURE 2.5: Population transfer due to a fifth order Bragg diffraction process ($\delta = 10\omega_r$) versus the Rabi frequency. The atomic population oscillates between the initial $n_I = 0$ state (red trace) and the $n_F = 5$ state (green trace), with some residual atomic loss in unwanted momentum states (dashed lines). Bragg diffraction is excited with a Gaussian pulse with $\sigma = 0.292\omega_r^{-1}$.

presence of atoms in undesired momentum states by using shorter pulses with particular time profiles which provide a quasi-adiabatic population transfer through the undesired momentum states with high efficiency. The amount of atom losses in unwanted momentum states can be optimized acting on the parameters of these pulses.

Typical high transfer efficiency Raman beam-splitters are obtained with square pulses. This simple kind of envelope cannot be used also for Bragg beam-splitters with a high efficiency. When using Bragg beam-splitters it is more appropriate to use envelopes derived from continuous and slowly varying functions; in our set-up we use truncated Gaussian pulses which have been studied extensively in [40], [41], [51], [52][3]

$$\Omega'(t) = \begin{cases} \Omega e^{-t^2/(2\sigma^2)} & \text{if } -\tau \leq t \leq \tau \\ 0 & \text{otherwise} \end{cases}$$

In our experimental set-up the typical value for the width σ of the pulses is 12 μs. With such an envelope we can numerically solve the system 2.45. In our analysis we consider a fifth order Bragg diffraction process which resonantly couples the momentum states with $n_I = 0$ and $n_F = 5$, i.e. $\delta = 10\omega_r$. In the following we always assume a pulse width of $\sigma = 0.292\omega_r^{-1} = 12$ μs and $\tau = 5\sigma$. We start our analysis deriving the atomic population dependence on the Rabi frequency. The results are reported in Fig. 2.5. The continuous lines represent the atomic population in the two momentum states of interest with $n_I = 0$ (red line) and $n_F = 5$ (green line). We note that the atomic population starts from n_I and is coupled to n_F and also to the four intermediate states with $1 \leq n \leq 4$ which are represented with the dashed lines. The presence of the unwanted momentum states makes impossible to transfer the initial atomic population completely to the state $n_F = 5$, however from this analysis we can derive the optimal intensities for an efficient π and $\pi/2$ pulse. We use the

---

[3]Other used pulse shapes are the Blackman window function or similar. These pulses have the desirable property of being zero at the edges $\pm\tau$ unlike the Gaussian pulses which need to be artificially truncated.
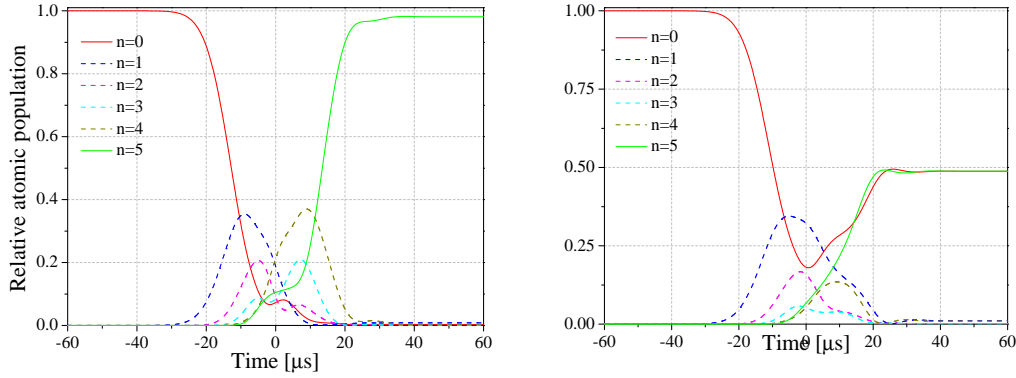
FIGURE 2.6: (Left) Atomic population versus time for a fifth order Bragg π pulse. The numerical evaluation is done with the optimal Rabi frequency derived from the analysis of Fig. 2.5, i.e. $\Omega_\pi \simeq 38\omega_r$. (Right) Atomic population versus time for a fifth order $\pi/2$ Bragg pulse. In this case we used $\Omega_{\pi/2} \simeq 29\omega_r$. From both the pulses we can see how the atomic population traverses all the intermediate momentum states (represented with the dashed lines) before arriving at the final output state.

derived intensities to reproduce the effect of optimal π and $\pi/2$ pulses on the atomic population. In Fig. 2.6 we report the atomic population dependence on the pulse time during the interaction with a π and a $\pi/2$ pulse. We note the quasi-adiabatic population dynamic during the pulse; indeed the atomic population traverses all the intermediate momentum states, from the lower till the higher until it reaches the target output state (with some residual losses in unwanted momentum states).

It is also interesting to consider the effect of a non perfectly resonant pulse. Fig. 2.7 shows the atomic population for a $\pi/2$ pulse versus the detuning δ. Varying the detuning with respect to the resonance condition for the fifth order Bragg transition $\delta = 10\omega_r$, changes significantly the efficiency of the pulse. Furthermore when the detuning is lowered we note that a larger fraction of atomic population is accumulated in the lower momentum states since they become closer to resonance, in particular the $n_F = 4$ state (dashed dark yellow trace).

2.2 Interferometric phase shifts calculation

2.2.1 Atom interferometry

As already mentioned an AI experiment can usually be divided in three stages. Initially we have the preparation of the atomic sample; then two or more laser pulses are applied on the atomic sample to realize the chosen interferometric sequence; finally the atomic population at the output of the interferometer is detected. We overlook for the moment the preparation and detection stages, which will be described in detail later, and we concentrate now on the interferometric sequence.

During the interferometric sequence a series of electromagnetic pulses interact with the prepared atomic sample. In analogy to optical interferometers, each pulse can be thought of as a beam-splitter or a mirror for the matter-wave (see Sec. 2.1.1); each pulse is then able to change the internal atomic state and transfer momentum kicks to the atom. The pulse sequence initially splits the phase-space trajectories of the atomic wave-function in different interferometric paths and finally recombines them at the moment of the last pulse. The observable of interest in an AI experiment
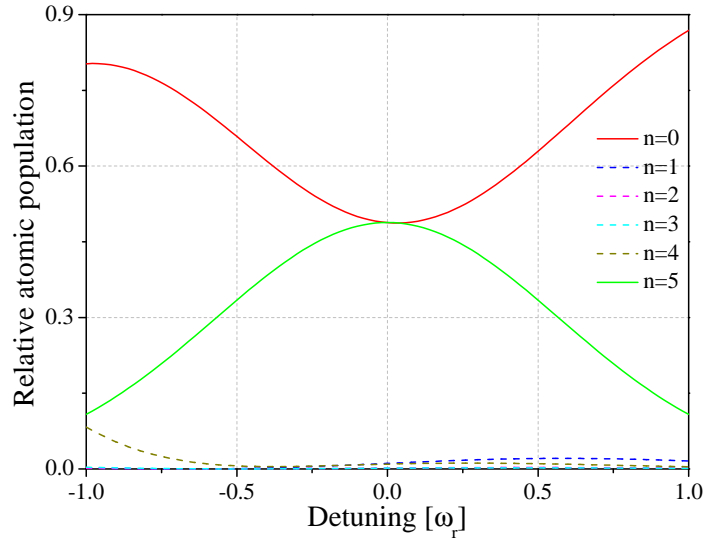
FIGURE 2.7: Dependence of the atomic population after a fifth order Bragg $\pi/2$ pulse on the detuning from the resonant condition $\delta = 10\omega_r$.

is the matter-wave phase shift ϕ which accumulates between the different paths; this phase shift can be measured by detecting the output atomic population P in one of the exit ports of the AI. Indeed the output population is a function of ϕ and can be written as $P(\phi) = \frac{1}{2}(1 - \cos(\phi))$; it thus exhibits a sinusoidal fringe pattern as a direct manifestation of the interference mechanism occurring at the output of the interferometer when the different paths are recombined.

There exist several ways to calculate the mathematical form of the interferometer phase shift ϕ. In principle the whole process could be analyzed completely by solving the time-dependent Schrödinger equation [53], [54]. However, due to the differences of the atomic evolution during the atom-light interaction periods and during the free-propagation periods several difficulties are encountered while following this approach. Indeed usually the two periods are treated separately and the individual results are then finally combined.

Since between the interferometric pulses the wave-functions propagate while being subjected to spatially varying forces a natural approach for analyzing the AI seems to be the path integral description of quantum mechanics [42], [55]. This analysis method is presented in Sec. 2.2.2.

Another method which has proven particularly useful for the calculation of the AI phase shift and in particular for analyzing the interferometer sensitivity to accelerations and to various sources of noise relies on the definition of the sensitivity function [56] and will be introduced in Sec. 2.2.3.

AIs as gravimeters and gradiometers

Before introducing the theoretical formalisms it is important to understand in general terms the experimental configuration of our apparatus. In the following theoretical analysis we will always consider a vertical AI, operated with Raman transitions in a Mach-Zehnder geometry. This is indeed the original configuration of the MA-GIA apparatus and of several other AIs used to detect gravitational phenomena and inertial accelerations.

These particular experimental apparatuses are typically realized using the atomic fountain configuration in which atoms are launched or dropped in vacuum and interrogated with the laser pulses during their ballistic trajectory. The two interferometric lasers[4] travel vertically along the length of the experimental set-up and are finally retro-reflected with a mirror. As we will see, the interferometer phase is sensitive to the acceleration experienced by the atoms along the direction of the lasers and in general can be written as $\phi = \mathbf{k}_{\text{eff}} \cdot \mathbf{a}T^2$. Indeed any external force which induces an acceleration on the atomic motion and consequently a displacement of the atom relative to the laser wave-fronts produces a phase shift between the interferometric arms. Since ϕ contains the information about the gravitational acceleration an instrument of this kind can be used as a gravimeter.

The MAGIA-Adv apparatus can realize simultaneous AIs with a relative vertical displacement between them. Typically we launch two samples separated by 30 cm and on each sample we implement an AI probing the local free fall acceleration of the atoms. Considering the difference in the signals from these two AIs $\Phi = \phi_u - \phi_l$ (with $\phi_{(u,l)}$ the AI phase of the upper and lower interferometer) we can thus obtain a measure of the differential acceleration of the ensembles due to their vertical separation. In this configuration the experimental apparatus is sensitive to the gradient of the gravitational acceleration averaged over the AIs separation and can be considered as a gradiometer.

2.2.2 Feynman path integral approach

Let us consider the atom interferometer sequence shown in Fig. 2.8 composed of $\pi/2 - \pi - \pi/2$ Raman pulses separated by a time T. The total interferometric phase can be decomposed as the sum of three distinct contributions

$$\phi_{\text{tot}} = \phi_{\text{evol}} + \phi_{\text{int}} + \phi_{\text{sep}}. \tag{2.46}$$

ϕ_{evol} accounts for the free evolution of the atomic wave-function between the pulses; ϕ_{int} is due to the atom-light interaction; ϕ_{sep} derives from a non perfect overlap of the interferometric arms at the moment of the last $\pi/2$ pulse.

The phase contribution due to the atomic free evolution ϕ_{evol} can be expressed starting from the definition of the phase β_g of a matter-wave $\psi \equiv \exp(-i\beta_g)$ given by Luis de Broglie [57] as

$$\beta_{\text{g}} = \frac{mc^2}{\hbar}\tau, \tag{2.47}$$

where m is the rest mass of the particle, c the speed of light and τ the particle proper time. It is interesting to note that in the non-relativistic limit, i.e. for weak gravitational fields and velocities small compared to c the proper time can be expressed as

$$d\tau \simeq dt - \frac{1}{mc^2}\mathcal{L}_{\text{g}}dt, \tag{2.48}$$

where $\mathcal{L}_{\text{g}} = \frac{1}{2}mv^2 - m\Phi_{\text{g}}$ is the non-relativistic Lagrangian which accounts for the kinetic energy of the particle with velocity $v \ll c$ and for the weak gravitational potential Φ_{g}. The matter-wave then can be written as

$$\psi = e^{-i\beta_{\text{g}}} \simeq \exp\left[-\frac{i}{\hbar}mc^2t\right] \exp\left[\frac{i}{\hbar}\int dt\,\mathcal{L}_{\text{g}}\right]. \tag{2.49}$$

---

[4]In our set-up the interferometric pulses are realized with Raman or Bragg transitions which need a couple of laser beams to be excited.
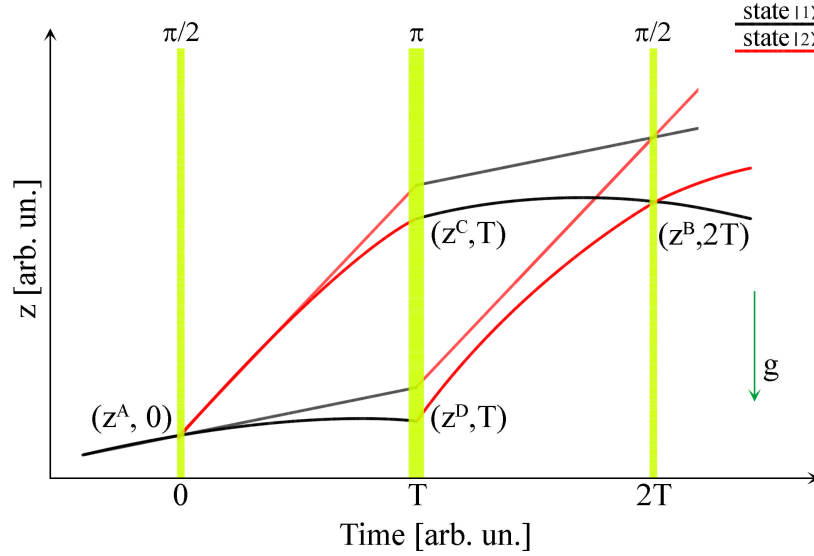
FIGURE 2.8: Space-time trajectories for an atom in a vertical Mach-Zehnder atom interferometer implemented with Raman pulses. The straight lines represent the trajectories without gravitational acceleration, while the parabolic lines take into account the effect of gravity. The interferometric pulses are shown with the green lines. g represents the gravitational acceleration.

We note that the first term in the equations above takes into account the atomic rest mass. In a standard Mach-Zehnder interferometer with two paths of identical coordinate time t this term does not produce any contribution to the total interferometric phase ϕ_{tot}. We thus obtain $\phi_{\text{evol}} = \frac{1}{\hbar} \int dt \mathcal{L}_g$. The phase due to the free evolution is thus the action calculated along the classical trajectory of the particle divided by $\hbar$.

ϕ_{int} can be derived using the results reported in Tab. 2.1 and for a MZ interferometer is

$$\phi_{\text{int}} = \phi_{\text{eff}}(z^A, 0) - \phi_{\text{eff}}(z^D, T) - \phi_{\text{eff}}(z^C, T) + \phi_{\text{eff}}(z^B, 2T) + \theta_0^0 - \theta_{2T}^0, \qquad (2.50)$$

with $\phi_{\text{eff}}(z, t) = k_{\text{eff}} z(t) + \phi^0$; we used the atomic coordinates as defined in Fig. 2.8, k_{eff} represents the momentum imparted on the atoms during the interferometric transitions, ϕ^0 is the phase difference between the interferometric lasers and the additional phase terms $\theta_{(0,2T)}^0$ take into account the differential light shift contribution due to the $\pi/2$ pulses.

ϕ_{sep} arises when the atoms are subjected to non-uniform force fields which determine a non perfect overlap of the atomic wave-function at the output of the interferometer. In this case, even with a non perfect overlap, interference can still occur because of the spatial extension of the atomic wave-packet. However we have to consider an additional phase term

$$\phi_{\text{sep}} = \frac{\mathbf{p} \cdot (\mathbf{z}_I^B - \mathbf{z}_{II}^B)}{2\hbar}, \qquad (2.51)$$

with $\mathbf{z}_I^B$ and $\mathbf{z}_{II}^B$ the end points of the two different interferometric arms. This contribution arises in presence of a gravity gradient for example.

We will now present some of the major AI phase shift contributions.

TABLE 2.2: Characteristic quantities for the classical trajectories in the MZ atom interferometer for atoms subjected to a constant gravitational potential.

	$0 < t < T$	$T < t < 2T$
Velocity on upper path, v_u	$v(t) + \frac{\hbar k_{\text{eff}}}{m}$	$v(t)$
Velocity on lower path, v_l	$v(t)$	$v(t) + \frac{\hbar k_{\text{eff}}}{m}$
Upper path z_u	$z(t) + \frac{\hbar k_{\text{eff}}}{m}t$	$z(t) + \frac{\hbar k_{\text{eff}}}{m}T$
Lower path z_l	$z(t)$	$z(t) + \frac{\hbar k_{\text{eff}}}{m}(t - T)$

Phase shift in a gravity field

Let us consider an AI interrogating an atom in free fall in a gravity field g. The complete Lagrangian $\mathcal{L}_g$ can be written as

$$\mathcal{L}_g = \frac{1}{2}mv^2 - V_g(z), \tag{2.52}$$

and involves the kinetic energy with the velocity $v = \dot{z}$ and the linear gravitational potential $V_g(z) = mgz$. The classical trajectory $z(t)$ followed by the atoms in the MZ interferometer can be calculated from the Euler-Lagrange equations for $\mathcal{L}_g$ considering also the momentum transfer on the atoms due to the interaction with the laser light at the times of the interferometric pulses

$$z(t) = z(0) + v(0)t - \frac{1}{2}gt^2 + \sum_{j=0}^{2} \int_{-\infty}^{t} dt' \Theta(t' - jT)\frac{p_j}{m}, \tag{2.53}$$

where $z(0)$ and $v(0)$ are the atomic height and velocity just before the first laser pulse, Θ is the Heaviside step function and

$$p_j = \begin{cases} +\hbar k_{\text{eff}} & \text{for } |a\rangle \to |b\rangle, \\ -\hbar k_{\text{eff}} & \text{for } |b\rangle \to |a\rangle, \\ 0 & \text{no interaction.} \end{cases}$$

In Tab. 2.2 we summarize the characteristics of the atomic classical dynamics in the MZ interferometer.

We can now calculate the phase shift contribution due to the free evolution ϕ_{evol} as

$$\phi_{\text{evol}} = \frac{1}{\hbar} \oint dt \mathcal{L}_g = \frac{1}{\hbar} \oint dt \frac{1}{2}mv^2 - \frac{1}{\hbar} \oint dt V_g. \tag{2.54}$$

Using the results in Tab. 2.2 we now calculate the two individual phase terms in the equation above, starting with the one associated to the kinetic energy

$$\phi_{\text{kin}} = \frac{1}{\hbar} \int_0^{2T} dt \frac{1}{2}m(v_u^2 - v_l^2) = k_{\text{eff}} \int_0^T dt \left(v_g + \frac{\hbar k_{\text{eff}}}{2m} \right) - k_{\text{eff}} \int_T^{2T} dt \left(v_g(t) + \frac{\hbar k_{\text{eff}}}{2m} \right) =$$
$$- k_{\text{eff}}[z_g(2T) - 2z_g(T) + z_g(0)] = -k_{\text{eff}}\ddot{z}_g(0)T^2.$$

We then obtain

$$\phi_{\text{kin}} = k_{\text{eff}} g T^2. \tag{2.55}$$

We now evaluate the contribution due to the gravitational potential energy

$$\phi_{\text{g}} = \frac{1}{\hbar} \int_0^{2T} dt \, mg(z_u - z_l) = k_{\text{eff}} g \int_0^T dt \, t + k_{\text{eff}} g \int_T^{2T} dt \, (2T - t) = k_{\text{eff}} g T^2.$$

Which results in

$$\phi_{\text{evol}} = \phi_{\text{kin}} - \phi_{\text{g}} = 0. \tag{2.56}$$

Also $\phi_{\text{sep}} = 0$ since in a constant gravitational field the atomic trajectories overlap perfectly at the time of the final beam-splitter.

The last contribution to ϕ_{tot} derives from the atom-light interaction. We note that since the atomic vertical velocity changes linearly with time during the free-fall, the Raman lasers frequency difference has to be swept linearly in order to compensate for the changing Doppler effect and maintain the resonance during all the interferometric sequence. From Eq. 2.50 considering $z(0) = 0$ and $v(0) = v_0$ we obtain

$$
\begin{aligned}
\phi_{\text{eff}}(z^A, 0) &= \phi^0(0) + \theta_0^0, \\
\phi_{\text{eff}}(z^D, T) &= k_{\text{eff}} \left[-\frac{1}{2} g T^2 + v_0 T \right] + \phi^0(T), \\
\phi_{\text{eff}}(z^C, T) &= k_{\text{eff}} \left[-\frac{1}{2} g T^2 + \left(v_0 + \frac{\hbar k_{\text{eff}}}{m} \right) T \right] + \phi^0(T), \\
\phi_{\text{eff}}(z^B, 2T) &= k_{\text{eff}} \left[-2 g T^2 + 2 v_0 T + \frac{\hbar k_{\text{eff}}}{m} T \right] + \phi^0(2T) + \theta_{2T}^0.
\end{aligned}
\tag{2.57}
$$

We finally get

$$\phi_{\text{tot}} = \phi_{\text{int}} = -k_{\text{eff}} g T^2 + \delta\phi^0 + \theta_0^0 - \theta_{2T}^0, \tag{2.58}$$

with $\delta\phi^0 = \phi^0(0) - 2\phi^0(T) + \phi^0(2T)$ the difference between the phases of the laser pulses. We note that $\delta\phi^0$ is the discrete version of the second time derivative of the phase difference ϕ^0 between the two Raman lasers.

The result in Eq. 2.58 was derived considering the phase shifts induced by the Raman lasers reported in Tab. 2.1. We note that the total light shift Ω^{AC} does not contribute to the final interferometric phase. This is because we are considering an ideal case in which the laser beams pass through optics which do not produce an intensity modulation of the light over the separation between the interferometric arms. However, since the optics are not ideal, the final AI phase will also have a contribution from the total light shift; this term arises during the π pulse, when the separation between the interferometric arms is maximum. The effect of the differential light shift δ^{AC} is considered in Eq. 2.58 through the terms θ^0 which arise from the $\pi/2$ pulses. It is possible to eliminate this phase contribution with an appropriate choice of the Raman beams intensity ratio which makes $\Omega_1^{AC} = \Omega_2^{AC}$.

We note that since the MZ phase shift depends linearly on the momentum imparted to the atom k_{eff} a possible strategy to increase the sensitivity of the interferometer is to increment this momentum. This is the reason why the development of Large Momentum Transfer interferometers is a strongly active field of research in atomic physics today. Another way to increase the interferometer sensitivity is of course to increment the interrogation time T. This can be done using taller apparatuses or set-ups in micro-gravity environments.

Eq. 2.58 can be refined taking into account the wave-packet evolution during the interferometric pulse finite time length τ. The complete analysis can be found in [58] and the phase shift becomes

$$\phi_{\text{tot}} = -k_{\text{eff}}g\left(T + \frac{4\tau}{\pi}\right)(T + 2\tau) + \delta\phi^0, \tag{2.59}$$

where in this case we neglected the contribution from the light shift.

Phase shift in presence of a gravity gradient

We now consider the effect of a gravity acceleration gradient on the AI phase shift. In this case for a symmetric MZ interferometer the atomic trajectories will not perfectly overlap at the moment of the closing $\pi/2$ pulse and $\phi_{\text{sep}} \neq 0$.

In presence of a constant gravity gradient γ the gravitational acceleration can be expressed considering a reference value $-g$ at height $z = 0$ so that the equation of motion of a free body can be written as $\ddot{z}(t) = -g + \gamma z(t)$. During a MZ interferometer the separation between the interferometric arms is maximum at the time of the central π pulse and corresponds to $\delta z = 2v_r T$, where $v_r \simeq 6$ mm/s is the ^{87}Rb recoil velocity. Considering standard operating conditions for our MZ interferometer we obtain for an interrogation time of $T = 100$ ms a maximum separation $\delta z = 1.2$ mm. With such a separation between the interferometric arms the action of a constant gravity gradient like the one of the Earth, $\gamma \sim 3 \times 10^{-6}$ s^{-2}, produces a detectable effect on the interferometric phase.

The interferometric phase shift can be evaluated using again the path integral formalism already introduced. This time considering a Lagrangian with a uniform gravity field term and a perturbation term which accounts for the gravity gradient, $\Delta\mathcal{L} = \frac{1}{2}m\gamma z^2$. The perturbation term introduces an additional phase shift [59] which adds up with the one produced by the uniform gravity Lagrangian

$$\phi_{\text{grad}} = k_{\text{eff}}\gamma T^2\left(-\frac{7}{12}gT^2 + v_0 T + z_0\right). \tag{2.60}$$

We note that the phase contributions depending on the initial cloud velocity v_0 and initial cloud position z_0 derive from the separation of the atomic trajectories at the end of the interferometer. These terms are particularly problematic for high sensitivity measurements since they produce a systematic effect which is difficult to characterize with the required accuracy. However a mitigation strategy is proposed in [36] and will be the subject of experimental investigation in Sec. 5.4.

Multi pulses interferometric schemes can be implemented for a direct measurement of the gravity gradient [17]; however the most efficient strategy to measure γ is to use two vertically separated atomic samples which act as simultaneous AIs. By considering the differential phase shift Φ between the two AIs the huge phase shift due to the gravity acceleration is cancelled together with all the common mode sources of phase noise, i.e. all the sources which affect in the same way both the AIs. The obtained signal can then be written as

$$\Phi = \phi_{\text{up}} - \phi_{\text{dw}} = -k_{\text{eff}}(g_{\text{up}} - g_{\text{dw}})T^2 = -k_{\text{eff}}\gamma dT^2, \tag{2.61}$$

with d the relative spatial separation between the two AIs and g_{up} and g_{dw} the gravity acceleration values at the height of the atomic samples. In our experimental apparatus we adopt this configuration and we usually work with $d = 30$ cm which

determines a differential acceleration of $\sim 10^{-7}$ g between the simultaneous interferometers.

Phase shift in presence of small rotations

We can follow the same procedure adopted in the previous example to consider the effect on an atom interferometer of small rotations. In this case, if $\mathbf{\Omega}$ is the vectorial angular velocity, the perturbation term for the Lagrangian is $\Delta\mathcal{L} = m\mathbf{\Omega} \cdot (\mathbf{x} \times \mathbf{v})$ and the corresponding additional phase shift is

$$\phi_{\text{rot}} = -2\mathbf{\Omega} \cdot (\mathbf{v} \times \mathbf{k}_{\text{eff}})T^2. \tag{2.62}$$

In an atomic fountain apparatus the atoms are launched along the vertical direction, however due to the finite temperature of the samples a horizontal velocity spread is always present. Launch errors can also provide a small $\mathbf{v}$ component perpendicular to $\mathbf{k}_{\text{eff}}$ which we assume to be perfectly oriented along the vertical direction. If the interferometric measurement is performed at a latitude θ_l the rotation of the Earth produces a contribution to the phase shift of

$$\phi_{\text{rot}} = -2\Omega v_{\text{EW}} k_{\text{eff}} T^2 \cos\theta_l, \tag{2.63}$$

with v_{EW} the atomic horizontal velocity along the East-West direction.

Considering again an experimental set-up in which two simultaneous interferometers are performed at different heights, if the atomic samples are launched along two slightly different trajectories with a small tilt angle from the vertical direction, their horizontal velocities will be different at the moment of the interrogation. For this reason a Coriolis phase shift term will be present in the differential signal from the two simultaneous AIs

$$\Phi_{\text{rot}} = \phi_{\text{rot, up}} - \phi_{\text{rot, dw}} = -2\Omega\Delta v_{\text{EW}} k_{\text{eff}} T^2 \cos\theta_l. \tag{2.64}$$

The MAGIA-Adv apparatus is located at a latitude of $\theta_l = 43° \, 50' \, 07'' N$. Since a complete 2π Earth rotation takes 23 h 54 min 4 s (86,044 s) we have that $\Omega = 7.3 \times 10^{-5}$ rad/s. If we consider an interrogation time of $T = 100$ ms and $k_{\text{eff}} = 1.6 \times 10^7$ m^{-1} we obtain a differential phase shift of 16 mrad for each mm/s of East-West velocity difference.

To reduce the influence of the Coriolis acceleration on the AI one of the most common strategies is the use of a tip-tilt mirror for the two counter-propagating Raman beams [60], [61].

Phase shift from magnetic fields

The interaction between an atom with a magnetic dipole moment μ and a magnetic field $\mathbf{B}$ can be expressed as $-\mu \cdot \mathbf{B}$. If the atomic quantization axis is chosen along the z direction applying a bias magnetic field, the atom is subjected to an acceleration

$$\mathbf{a} = \frac{1}{m}\nabla(\mu \cdot \mathbf{B}) = \frac{1}{m}m_F \mu_B g_F \frac{dB_z}{dz}\frac{\mathbf{z}}{|\mathbf{z}|}, \tag{2.65}$$

with μ_B the Bohr magneton, g_F the Landè factor and m the atomic mass. From the previous equation we can see that in order to produce an acceleration, what is needed is a spatial gradient of the magnetic field along the quantization axis and that the acceleration depends on the m_F quantum number.

In order to suppress the effect of magnetically induced accelerations only ^{87}Rb atoms in the $m_F = 0$ state are used during the interferometric sequence. In this way the first order Zeeman effect is cancelled; however the second order Zeeman effect still has to be considered even for $m_F = 0$ atoms. The energy shift is described by the Breit-Rabi formula

$$U_m(z) = -\frac{\mu_B^2(g_J - g_I)^2}{2h\Delta_{hf}}B(z)^2, \tag{2.66}$$

with g_J and g_I the fine structure and nuclear Landè factors, h the Planck's constant and Δ_{hf} the hyperfine splitting frequency. The acceleration is then

$$\mathbf{a}_m = \frac{1}{m}\nabla\left(\frac{\mu_B^2(g_J - g_I)^2}{2h\Delta_{hf}}B^2\right)\hat{\mathbf{z}} = \frac{2h}{m}\alpha B\frac{dB}{dz}\hat{\mathbf{z}}, \tag{2.67}$$

where $\alpha = 575$ Hz/Gauss^2 for the D2 transition.

We now consider two simultaneous AIs vertically displaced by d and immersed in a magnetic field with a constant gradient B'. The resulting differential phase shift will be

$$\Phi_m = \mathbf{k}_{\text{eff}}(\mathbf{a}_{\text{m, up}} - \mathbf{a}_{\text{m, dw}})T^2 = k_{\text{eff}}\frac{2h}{m}\alpha(B_{\text{up}} - B_{\text{dw}})B'T^2 = k_{\text{eff}}\frac{2h}{m}\alpha dB'^2 T^2. \tag{2.68}$$

With $T = 100$ ms, $B' = 0.1$ Gauss/m and $d = 30$ cm the correction to the differential phase shift is of the order of $\simeq 3$ mrad, which corresponds to a few percent of the Earth gravity gradient signal.

There is also an additional correction to be considered. Indeed in addition to the mechanical effects the magnetic field produces also a phase term $\Delta\phi_M$ connected to the transition frequency change produced by the potential 2.66. To evaluate this phase shift we introduce this potential in the system Lagrangian and use the path integral treatment

$$\phi_M = \frac{1}{\hbar}\oint dt\, U_m(z(t)) = 2\pi\alpha\oint dt\, B(z(t))^2. \tag{2.69}$$

Performing the integration along the trajectory calculated neglecting the action of the magnetic field produces a result with a good approximation.

2.2.3 Sensitivity function approach

We now introduce a second formalism to obtain the total AI phase. This formalism was initially developed for calculating the influence of local oscillator noise on atomic clocks [56], but has proven very useful also for deriving the AI sensitivity to the various sources of phase shifts.

As in the previous case we will consider a vertical MZ interferometer operated with Raman transitions. In Sec. 2.1.2 we derived the equations for the population dynamics after the application of a Raman pulse. The result presented in Eq. 2.29 can be restated in matrix form as

$$\begin{pmatrix} a_1(t_0 + \tau) \\ a_2(t_0 + \tau) \end{pmatrix} = \mathcal{M}(t_0, \phi_{\text{eff}}, \Omega_{\text{eff}}, \tau)\begin{pmatrix} a_1(t_0) \\ a_2(t_0) \end{pmatrix},$$

where $\mathcal{M}(t_0, \phi_{\text{eff}}, \Omega_{\text{eff}}, \tau)$ is the transfer matrix for a single Raman pulse. If we consider the ideal condition in which the total and differential light shifts produce no

phase contribution and in which the resonance condition is verified the transfer matrix is

$$
\mathcal{M}(t_0, \phi_{\mathrm{eff}}, \Omega_{\mathrm{eff}}, \tau) = \begin{pmatrix} \cos\left(\frac{|\Omega_{\mathrm{eff}}|\tau}{2}\right) & -ie^{\phi^0}\sin\left(\frac{|\Omega_{\mathrm{eff}}|\tau}{2}\right) \\ -ie^{-\phi^0}\sin\left(\frac{|\Omega_{\mathrm{eff}}|\tau}{2}\right) & \cos\left(\frac{|\Omega_{\mathrm{eff}}|\tau}{2}\right) \end{pmatrix}, \tag{2.70}
$$

while the transfer matrix describing the wave-packet evolution during the free-fall is obtained setting $\Omega_{\mathrm{eff}} = 0$

$$
\mathcal{M}(T) = \begin{pmatrix} 1 & 0 \\ 0 & 1 \end{pmatrix}.
$$

In this formalism the complete MZ interferometer is modelled as the matrix product

$$
\mathcal{M}_{\mathrm{int}} = \mathcal{M}(T+\tau, \phi_{\mathrm{eff}}^{(3)}, \Omega_{\mathrm{eff}}, \tau)\mathcal{M}(T)\mathcal{M}(-\tau, \phi_{\mathrm{eff}}^{(2)}, \Omega_{\mathrm{eff}}, 2\tau)\mathcal{M}(T)\mathcal{M}(-T-2\tau, \phi_{\mathrm{eff}}^{(1)}, \Omega_{\mathrm{eff}}, \tau),
$$

where we set the time origin at the middle of the π pulse.

The transition probability, considering an initial state in which all atoms are in state $|1\rangle$ is

$$
P_2 = |a_2(T+2\tau)|^2 = \frac{1 - \cos(\phi_{\mathrm{eff}}^{(1)} - 2\phi_{\mathrm{eff}}^{(2)} + \phi_{\mathrm{eff}}^{(3)})}{2}, \tag{2.71}
$$

from which we can conclude again (see Eq. 2.50) that the phase difference between the two interferometric arms is $\phi = \phi_{\mathrm{eff}}^{(1)} - 2\phi_{\mathrm{eff}}^{(2)} + \phi_{\mathrm{eff}}^{(3)}$. The interferometer is therefore sensitive to phase noise over the three Raman pulses and to all the effects that modify the transition frequency during the interferometric sequence.

We now want to explicitly calculate the influence of the mentioned effects on the interferometer phase using a mathematical formalism based on the sensitivity function.

We start considering the effect of a phase jump $\delta\phi_{\mathrm{eff}}$ of the phase difference between the Raman lasers. The phase jump will affect the measured transition probability at the output of the interferometer with a variation δP. At this point we can define the sensitivity function as

$$
g_s(t) = 2 \lim_{\delta\phi_{\mathrm{eff}} \to 0} \frac{\delta P(\delta\phi_{\mathrm{eff}}, t)}{\delta\phi_{\mathrm{eff}}}. \tag{2.72}
$$

Since the transition probability is directly linked to the interferometric phase ϕ the relation above can be rewritten as

$$
g_s(t) = \lim_{\delta\phi_{\mathrm{eff}} \to 0} \frac{\delta\phi(\delta\phi_{\mathrm{eff}}, t)}{\delta\phi_{\mathrm{eff}}}. \tag{2.73}
$$

If the phase jump happens during the free evolution phase of the AI sequence the sensitivity function can be straightforwardly calculated expanding Eq. 2.71. In the case of a phase jump between the second and third interferometric pulse the phase values will be[5] $\phi_{\mathrm{eff}}^{(1)} = \varphi + \pi/2$, $\phi_{\mathrm{eff}}^{(2)} = \varphi$ and $\phi_{\mathrm{eff}}^{(3)} = \varphi + \delta\phi_{\mathrm{eff}}$ and the sensitivity function becomes $g_s = +1$. When the phase jump occurs between the first and second interferometric pulses the sensitivity function is $g_s = -1$. If the phase jump

---

[5]We suppose to operate the interferometer at mid-fringe where the sensitivity is maximum (see Eq. 2.72).
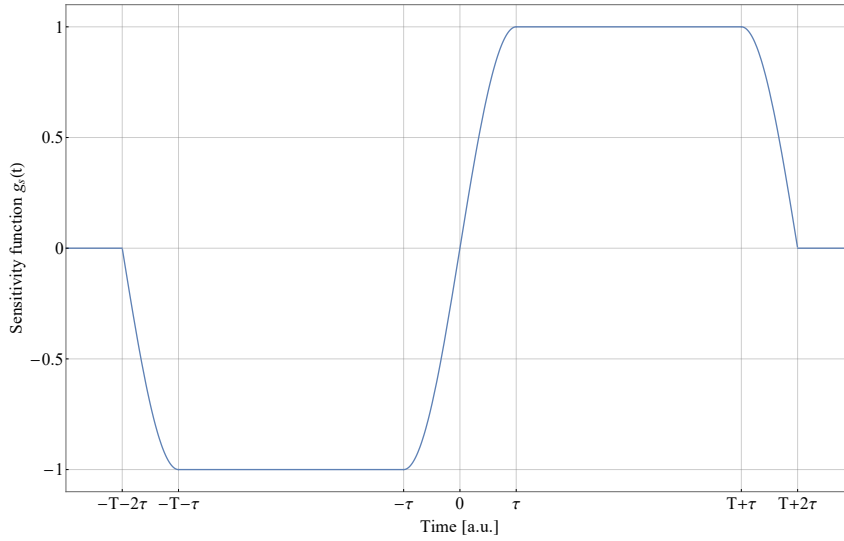
FIGURE 2.9: Behaviour of the MZ sensitivity function as reported in Eq.5.35.

happens during one of the three interferometric pulses we can evaluate g_s by splitting the single pulse transfer matrix $\mathcal{M}(t_0, \phi_{\text{eff}}, \Omega_{\text{eff}}, \tau)$ (see Eq. 2.70) in two parts. If the jump happens at the time t during the first pulse ($-2\tau - T < t < -\tau - T$) we can then write

$$\mathcal{M}(-T - 2\tau, \phi_{\text{eff}}, \Omega_{\text{eff}}, \tau) = \mathcal{M}(t, \phi_{\text{eff}} + \delta\phi_{\text{eff}}, \Omega_{\text{eff}}, -T - \tau - t)\mathcal{M}(-T - 2\tau, \phi_{\text{eff}}, \Omega_{\text{eff}}, t + T + 2\tau).$$

Finally if the phase jump happens outside of the interferometric sequence the sensitivity function is null, i.e. $g_s = 0$.

We can now write the complete expression for the sensitivity function of the MZ interferometer; setting $|\Omega'_{\text{eff}}|\tau = \pi/2$ we obtain (see Fig.2.9)

$$g_s(t) = \begin{cases} 0 & \text{for} \quad t < -T - 2\tau, \\ \sin(\Omega'_{\text{eff}}(t + T)) & \text{for} \quad -T - 2\tau < t < -T - \tau, \\ -1 & \text{for} \quad -T - \tau < t < -\tau, \\ \sin(\Omega'_{\text{eff}}t) & \text{for} \quad -\tau < t < \tau, \\ +1 & \text{for} \quad \tau < t < \tau + T, \\ \sin(\Omega'_{\text{eff}}(t - T)) & \text{for} \quad T + \tau < t < T + 2\tau, \\ 0 & \text{for} \quad T + 2\tau < t. \end{cases} \tag{2.74}$$

We can now use the sensitivity function $g_s(t)$ to calculate the interferometric phase ϕ for any variation of the Raman phase $\phi_{\text{eff}}(t)$. From Eq. 2.73 we obtain

$$\phi = \int_{-\infty}^{+\infty} g_s(t)d\phi_{\text{eff}}(t) = \int_{-\infty}^{+\infty} g_s(t)\frac{d\phi_{\text{eff}}(t)}{dt}dt. \tag{2.75}$$

We now consider the case of a vertical AI realized in presence of a uniform gravity field g. If the atoms have an initial velocity v_0, the Raman phase shift that they experience due to their free fall motion can be written as

$$\phi_{\text{eff}}(t) = k_{\text{eff}}z(t) + \phi^0(t) = \frac{k_{\text{eff}}gt^2}{2} + k_{\text{eff}}v_0t + \phi^0(t). \tag{2.76}$$

We note that since the sensitivity function is odd, the contribution of v_0 to the phase shift cancels; furthermore since in our apparatus we can control the Raman phase difference $\phi^0(t)$, we will not introduce it in the final phase shift calculation. The complete phase shift is

$$\phi = \int_{-\infty}^{+\infty} g_s(t) k_{\text{eff}} g t \, dt = k_{\text{eff}} g (T + 2\tau)(T + 4\tau/\pi), \tag{2.77}$$

which is the same result already presented in Eq. 2.59. This calculation was performed assuming that the resonance condition of the Raman pulses is always verified for all the three MZ pulses. However due to the Doppler effect this assumption does not hold for the typical interrogation times T considered in AIs and in a real experiment the resonance condition has to be maintained by changing the relative frequency difference between the Raman lasers linearly in time. This is possible adding a linear frequency ramp α on the frequency of one of the two Raman lasers. Considering also this effect the phase shift becomes

$$\phi = (k_{\text{eff}} g - \alpha)(T + 2\tau)(T + 4\tau/\pi). \tag{2.78}$$

From the equation above we note that once k_{eff} is known, the value of g can be measured by determining the frequency ramp α_0 for which $\phi = 0$, i.e. the frequency ramp which exactly compensates the Doppler effect of the freely falling atoms.

Transfer function formalism

The formalism of the sensitivity function is particularly useful for calculating the effects of phase noise sources on the atom interferometer signal. Since in this case we do not know the temporal evolution of the phase (unlike in the previous calculation, see Eq. 2.76) we will consider its noise spectrum in Fourier space. Let us start by considering a sinusoidal phase noise of the form $\phi_{\text{eff}}(t) = A_0 \cos(\omega_0 t + \psi)$. From Eq. 2.75 we obtain

$$\phi = \int_{-\infty}^{+\infty} -g_s(t) A_0 \omega_0 \sin(\omega_0 t + \psi) dt. \tag{2.79}$$

If in the equation above we perform the substitution $\sin(\omega_0 t + \psi) = \sin(\omega_0 t)\cos(\psi) + \cos(\omega_0 t)\sin(\psi)$, since the sensitivity function is odd the integral of the term with $\cos(\omega_0 t)$ is null and we obtain

$$\phi = A_0 \omega_0 \int_{-\infty}^{+\infty} -g_s(t)\sin(\omega_0 t)\cos(\psi) dt. \tag{2.80}$$

In the previous equation we note the presence of the Fourier transform of the sensitivity function $G(\omega) = \int_{-\infty}^{+\infty} e^{-i\omega t} g_s(t) dt$; indeed $G(\omega)$ can be simplified by writing $e^{-i\omega t} = \cos(\omega t) - i\sin(\omega t)$ and by considering again that since $g_s(t)$ is odd, the integral of the cosine part is null. We thus obtain

$$G(\omega) = \int_{-\infty}^{+\infty} -i\sin(\omega t) g_s(t) dt. \tag{2.81}$$

Eq. 2.80 then becomes

$$\phi = -i A_0 \omega_0 G(\omega_0)\cos(\psi) = A_0 \omega_0 |G(\omega_0)|\cos(\psi). \tag{2.82}$$
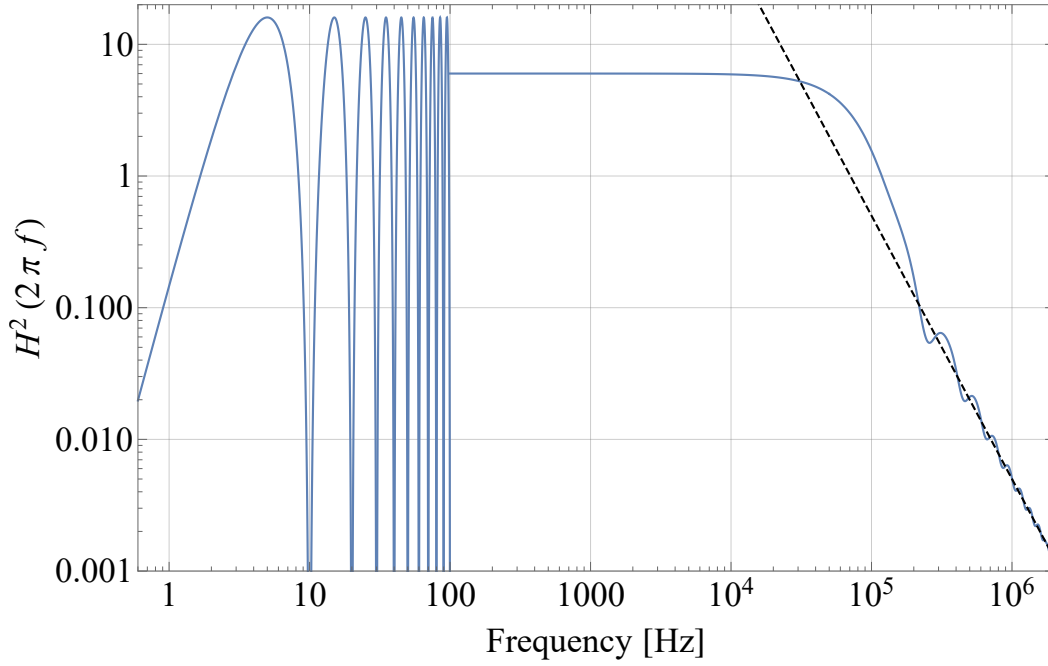
FIGURE 2.10: In blue the square root of the MZ transfer function. For frequencies above 100 Hz the function is replaced with its mean value. With the black dashed line we represent the scaling obtained for $\omega \gg \Omega'_{\text{eff}}$. The parameters used are $\Omega'_{\text{eff}} = 2\pi 50$ kHz, $T = 100$ ms and $\tau = 24$ μs.

Considering a randomly distributed phase ψ the standard deviation of the interferometer phase fluctuations is $\sigma_\phi = A_0 \omega_0 |G(\omega_0)| / \sqrt{2}$. The variance of the interferometer phase fluctuations can be calculated from the phase noise spectral density S_ϕ as

$$\sigma_\phi^2 = \int_0^\infty |\omega G(\omega_0)|^2 S_\phi(\omega) \frac{d\omega}{2\pi}. \tag{2.83}$$

If we now consider the MZ sensitivity function defined in Eq. 5.35, its Fourier transform is

$$G(\omega) = \frac{4i\Omega'_{\text{eff}}}{\omega^2 - \Omega'^2_{\text{eff}}} \sin\left(\frac{\omega(T + 2\tau)}{2}\right) \left[\cos\left(\frac{\omega(T + 2\tau)}{2}\right) + \frac{\Omega'_{\text{eff}}}{\omega} \sin\left(\frac{\omega T}{2}\right)\right]. \tag{2.84}$$

With the equation above we can then define the MZ transfer function $H(\omega) = |\omega G(\omega)|$

$$H(\omega) = \frac{4\omega\Omega'_{\text{eff}}}{\omega^2 - \Omega'^2_{\text{eff}}} \sin\left(\frac{\omega(T + 2\tau)}{2}\right) \left[\cos\left(\frac{\omega(T + 2\tau)}{2}\right) + \frac{\Omega'_{\text{eff}}}{\omega} \sin\left(\frac{\omega T}{2}\right)\right]. \tag{2.85}$$

In Fig. 2.10 we report the square root of the transfer function calculated above. Due to the multiplying sine term the square root of $H(\omega)$ vanishes periodically for multiples of $\omega = 2\pi/(T + 2\tau)$. In the graph, for frequencies above 100 Hz, we have replaced $H^2(\omega)$ with its average

$$\bar{H}^2(\omega) = \frac{4\Omega'^4_{\text{eff}}}{(\Omega'^2_{\text{eff}} - \omega^2)^2} \left(\frac{3}{2} + \frac{3\omega^2}{4\Omega'^2_{\text{eff}}} - \left(\sin\left(\frac{\pi\omega}{2\Omega'_{\text{eff}}}\right) + \frac{\omega}{2\Omega'_{\text{eff}}}\right)^2\right). \tag{2.86}$$

Due to the $4\omega\Omega'_{\text{eff}}/(\omega^2 - \Omega'^2_{\text{eff}})$ term in $H(\omega)$, when the frequency of the phase fluctuations is large compared to the Rabi frequency ($\Omega'_{\text{eff}} = 2\pi 50$ kHz) we can average the fluctuations over the pulse duration. The transfer function then acts as a low pass filter with cut-off frequency Ω'_{eff}/π and which scales as $\sqrt{2}\Omega'_{\text{eff}}/\omega$ for $\omega \gg \Omega'_{\text{eff}}$ (see dashed line of Fig. 2.10).

Sensitivity to phase noise

In order to determine the sensitivity achievable with a MZ gravimeter in presence of a given phase noise spectral density it is not appropriate to use the variance on a single phase measurement as defined in Eq. 2.83. We rather introduce the Allan variance of the interferometer phase fluctuations [62] as

$$\sigma_\phi^2(\tau_m) = \frac{1}{2}\lim_{n\to\infty}\left[\frac{1}{n}\sum_{k=1}^{n}(\bar{\phi}_{k+1} - \bar{\phi}_k)^2\right], \tag{2.87}$$

where τ_m is the total integration time and $\bar{\phi}_k$ is the average of the measured phase shifts in the interval (t_k, t_{k+1}). Introducing the repetition time T_c as the time needed for a single measurement the total integration time becomes $\tau_m = mT_c$ and the previous time interval can be rewritten as $(t_k, t_{k+1}) = (-T_c/2 + kmT_c, -T_c/2 + (k+1)mT_c)$. The mean value $\bar{\phi}_k$ can be calculated using the sensitivity function as

$$\begin{aligned}\bar{\phi}_k &= \frac{1}{m}\sum_{i=1}^{m}\int_{t_k+(i-1)T_c}^{t_k+iT_c} g_s(t - t_k - (i-1)T_c - T_c/2)\frac{d\phi_{\text{eff}}}{dt}dt \\ &= \frac{1}{m}\int_{t_k}^{t_{k+1}} g_k(t)\frac{d\phi_{\text{eff}}}{dt}dt,\end{aligned} \tag{2.88}$$

where $g_k(t) = \sum_{t=1}^{m} g_s(t - kmT_c - (i-1)T_c)$ is the sensitivity function for m measurements cycles. With this definition the difference in Eq. 2.87 can be written as

$$\bar{\phi}_{k+1} - \bar{\phi}_k = \frac{1}{m}\int_{-\infty}^{+\infty}(g_{k+1}(t) - g_k(t))\frac{d\phi_{\text{eff}}}{dt}dt. \tag{2.89}$$

We label the Fourier transform of $g_{k+1}(t) - g_k(t)$ as $G_m(\omega)$. Considering Eq. 2.83 we calculate $|G_m(\omega)|^2$ as

$$|G_m(\omega)|^2 = 4\frac{\sin^4(\omega mT_c/2)}{\sin^2(\omega T_c/2)}|G(\omega)|^2. \tag{2.90}$$

The equation above can be re-written as a comb of Dirac delta functions when the integration time increases

$$\lim_{\tau_m\to\infty}|G_m(\omega)|^2 = \frac{2m}{T_c}\sum_{j\to-\infty}^{+\infty}\delta(\omega - j2\pi f_c)|G(\omega)|^2, \tag{2.91}$$

where $f_c = 1/T_c$ is the cycle frequency.

Considering the definitions above and a phase $\phi_{\text{eff}}(t)$ characterized by a phase noise spectral density $S_{\phi_{\text{eff}}}(\omega)$ the Allan variance can be expressed as

$$\sigma_\phi^2(\tau_m) = \frac{1}{2m^2}\int_0^{+\infty}|\omega G_m(\omega)|^2 S_{\phi_{\text{eff}}}(\omega)\frac{d\omega}{2\pi}. \tag{2.92}$$
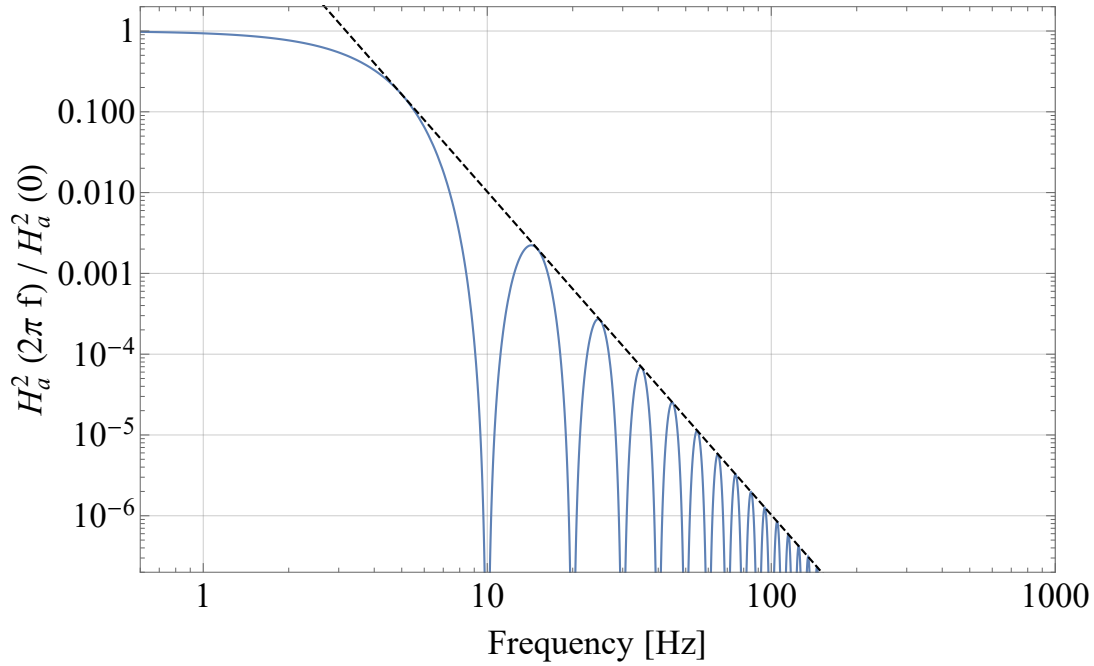
FIGURE 2.11: Square root of the acceleration transfer function $H_a(\omega)$. The function behaves as a low-pass filter with a cut off frequency $f_c = 1/(2T)$. The black dashed line represents the scaling as $16/(2\pi f T)^4$ obtained for frequencies above f_c. For the calculation we considered $T = 100$ ms, $\Omega'_{\text{eff}} = 2\pi 50$ kHz and $\tau = 24\ \mu$s.

Using the result in Eq. 2.91 the equations above becomes

$$\sigma_\phi^2(\tau_m) = \frac{1}{\tau_m} \sum_{n=1}^{\infty} |H(2\pi n f_c)|^2 S_{\phi_{\text{eff}}}(2\pi n f_c). \tag{2.93}$$

From this result we note that the phase noise at frequencies multiples of f_c is converted to low frequency noise from an aliasing effect which limits the interferometer sensitivity. When the phase noise is white, i.e. $S_{\phi_{\text{eff}}}(\omega) = S_{\phi_{\text{eff}}}^0$ the Allan variance becomes

$$\sigma_\phi^2(\tau_m) = \left(\frac{\pi}{2}\right)^2 \frac{T_c}{\tau} \frac{S_{\phi_{\text{eff}}}^0}{\tau_m}, \tag{2.94}$$

which shows that the phase noise depends also on the pulse duration τ and that it decreases when τ is increased. With $\tau = 24\ \mu$s, the white phase noise level required to obtain a maximum phase fluctuation of 1 mrad per experimental shot has to be less than or equal to -110 dB rad^2/Hz. In the gradiometer configuration two simultaneous AIs are realized with the same Raman pulses and we are interested in the phase difference between these two interferometers. Due to the differential measurement scheme most of the phase noise contributions are therefore rejected.

Acceleration and vibration sensitivity

Let us now consider the interferometer sensitivity to vibration noise. Since the two lasers are delivered to the atoms after being superposed on the same optical fibre any shift of an optical component before the retro-reflection mirror cannot induce (to first order) a differential phase shift between the Raman lasers. The vibration sensitivity

therefore derives only from the retro-reflection mirror which is used to produce the counter-propagating Raman beams used during the interferometric sequence. If this mirror moves of a quantity δz the phase of the retro-reflected beam is changed by $\delta \varphi = 2 k_i \delta z \simeq k_{\text{eff}} \delta z$. We can then define an acceleration sensitivity function $g_a(t)$ which accounts for an infinitesimal acceleration change δ_a as

$$g_a(t) = 2 \lim_{\delta_a \to 0} \frac{\delta P_a(\delta_a, t)}{\delta_a}. \tag{2.95}$$

The acceleration sensitivity function and its respective transfer function $H_a(\omega)$ can be written in terms of the phase sensitivity function and the phase transfer function as

$$g_s(t) = \frac{1}{k_{\text{eff}}} \frac{d^2 g_a(t)}{dt^2},$$

$$|H_a(\omega)|^2 = \frac{k_{\text{eff}}^2}{\omega^4} |H(\omega)|^2. \tag{2.96}$$

With the two definitions above and the result in Eq. 2.93 the Allan variance in presence of an acceleration noise with a spectral density $S_a(\omega)$ is

$$\sigma_\phi^2(\tau_m) = \frac{k_{\text{eff}}^2}{\tau_m} \sum_{n=1}^{\infty} \frac{|H(2\pi n f_c)|^2}{(2\pi n f_c)^4} S_a(2\pi n f_c). \tag{2.97}$$

Fig. 2.11 shows the square of the above defined acceleration transfer function. It acts as a low-pass filter with a cut-off frequency of $f_c = 1/(2T)$. In our experimental apparatus the usual interrogation times are of the order of $T = 100$ ms; we thus obtain a cut-off frequency of $f_0 = 5$ Hz which makes the system insensitive to high frequency vibration noise.

When the phase noise is white, $S_a(\omega) = S_a^0$ the interferometer sensitivity becomes

$$\sigma_\phi^2(\tau_m) = \frac{k_{\text{eff}}^2 T^4}{2} \left(\frac{2T_c}{3T} - 1 \right) \frac{S_a^0}{\tau_m}. \tag{2.98}$$

To have a maximum phase fluctuation of 1 mrad per measurement the required acceleration white noise has to be less than $\sim 10^{-8}$ m/s^2/Hz$^{1/2}$. However the ground vibration noise typically is 2×10^{-7} m/s^2/Hz$^{1/2}$ at 1 Hz and increases to 5×10^{-5} m/s^2/Hz$^{1/2}$ for frequencies up to 10 Hz. For this reason a vertical atom interferometer needs a seismical isolation on the retro-reflection mirror or a vibration correction method when high sensitivities are required. This is not the case in the gradiometric configuration since, as for the case of the Raman phase noise, also most of the acceleration noise is rejected in the differential measurement.

Chapter 3

Experimental apparatus

In this chapter we provide an extensive description of the MAGIA-Adv experimental apparatus (other descriptions of the same set-up can be found in [38], [63]–[65]). The complete experimental set-up is a vertical atomic fountain atom interferometer which can be operated as a gravimeter or as a gradiometer. We will start with a brief description of the vacuum system, the source masses and the experimental control system; then we will present the laser systems which produce the optical frequencies needed for the ^{87}Rb manipulation.

Particular attention will be devoted to the Raman and the Bragg laser systems. These two sources are crucial in our experiment since they provide the light which probes the atoms during the interferometer. Furthermore the Bragg set-up is one of the last additions to the complete laser system and was developed during this PhD work.

3.1 Vacuum system and source masses

Manipulation of atomic ^{87}Rb with laser light needs to be realized in an UHV (Ultra High Vacuum) environment ($\sim 10^{-9} - 10^{-10}$ Torr) in order to minimize possible interactions of the ^{87}Rb atoms with thermal background gases. The main vacuum system of the MAGIA-Adv apparatus has a vertically elongated structure; it is reported in Fig. 3.1 together with the two holders for the sets of cylindrical source masses used to modulate the gravity field in the interferometric region. From bottom to top we can distinguish three main parts of the vacuum system: a trap chamber were atoms are collected and cooled in a three dimensional Magneto-Optical Trap (3D-MOT); a detection chamber where the atomic population can be measured via fluorescence detection; the interferometric tube where the interrogation of the atoms takes place during their free fall motion.

3.1.1 Trap and Detection chambers

The trap chamber is the region of the apparatus where ^{87}Rb atoms are collected and cooled in a 3D-MOT. The chamber is derived from a light titanium alloy (TiAl$_6$V$_4$, 4430 kg/m^3) which is hard and non magnetic. This alloy also has the advantage of presenting a very high resistivity (168 $\mu\Omega$ cm). This characteristic permits to quickly damp undesired Eddy currents induced by varying electromagnetic fields. Another useful property derives from the thermal expansion coefficient of the alloy, which is very close to the one of the BK7 glass used for the optical windows.

The chamber was obtained from a 15 cm cube by cutting all the edges orthogonally to the diagonals. With this procedure the final chamber has 8 triangular faces and 6 square faces. A circular window with a diameter of 35 mm was drilled in any triangular face, while each square face has a circular window with a diameter of 50
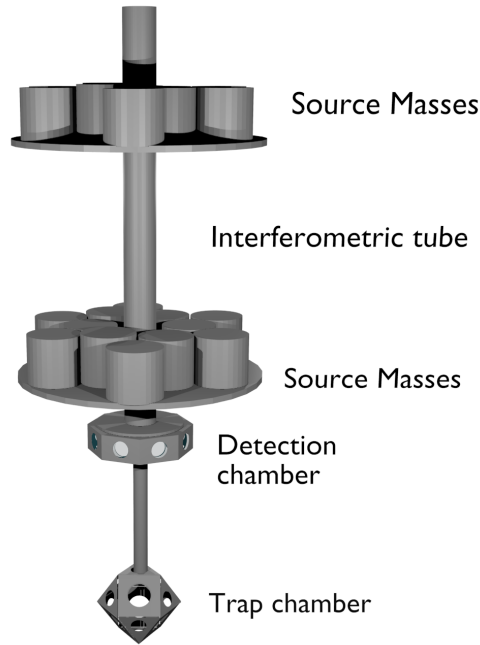
FIGURE 3.1: Main vacuum system of the experiment and source masses. The vacuum system is divided in three main parts; from bottom to top we have the trap chamber, the detection chamber and finally the interferometric tube. Around the interferometric tube, cylindrical source masses are organized in two sets and arranged in two holder plates which can translate vertically along all the tube length.

mm. The trapping and cooling laser beams of the 3D-MOT enter the chamber from the windows in the square faces and are arranged in the usual 1-1-1 configuration.

The MOT chamber is connected with the above detection chamber with a flexible bellow. The detection chamber is made of non-magnetic stainless steel 316LN and has the shape of a prism with octagonal base; it is derived from a hollow cylinder with a 170 mm internal diameter and 80 mm height. In each one of the 8 vertical faces it presents a circular optical window with a diameter of 60 mm. Of the 8 windows, 4 are used for the atomic detection system and 2 are employed to connect the vacuum apparatus with the pumping system. The remaining 2 free windows can be used as additional optical accesses whenever needed.

3.1.2   Interferometric tube

The interferometric tube defines the spatial region where the atom interferometer actually takes place. Since the ^{87}Rb interferometer is sensitive to magnetic fields the tube is realized with the same non magnetic, high resistivity titanium alloy of the trap chamber. The tube is 1 m long and has a circular section with an internal diameter of 35 mm and an external diameter of 40 mm which allows close positioning of the cylindrical source masses.

A coil is wrapped on the entire tube length, around a plastic cylinder placed outside the tube. It is used to generate a vertical magnetic field which defines the magnetic quantization axis for the ^{87}Rb atoms. Localized magnetic fields can be produced with 10 shorter coils wrapped one above the other and around the long one. We report the relevant coils parameters in Tab. 3.1.

TABLE 3.1: Relevant coils parameters.

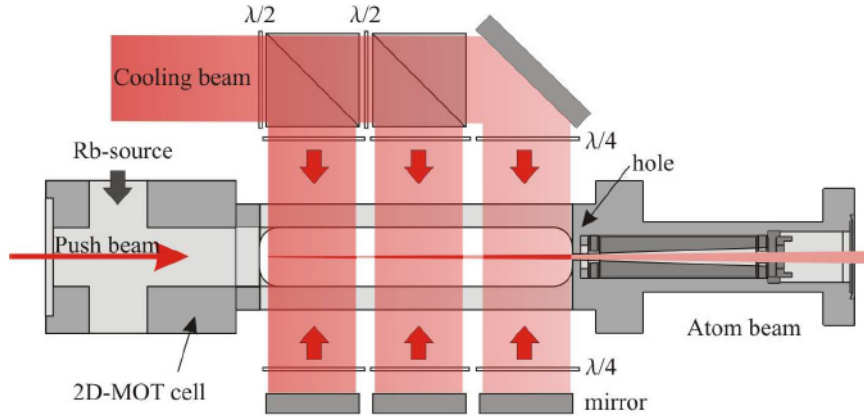| Coil	Wire ⌀ [mm]	Radius [mm]	Length [mm]	N	R [Ω]	B(i) [G/A]
Long	0.80(7)	32	926	1065	7.4	14.5
Short	0.80(7)	33	87	100	0.7	11.53

FIGURE 3.2: Top view of the 2D-MOT set-up used in the MAGIA-Adv apparatus. Figure adapted from [63].

Finally a double layer μ-metal shield is placed around the tube and the coils, to suppress external magnetic fields. The shields are two cylinders with length of 1028 mm and thickness of 0.76 mm; they are placed one inside the other and have diameters of 74 and 95 mm. With these two isolation layers, in the central region of the interferometric tube the axial fields are attenuated by 69 dB while the radial ones by 76 dB [63].

3.1.3 2D-MOT and atomic source

In order to both obtain high 3D-MOT loading rates and low background gas pressure in the vacuum system the 3D-MOT loading is aided with the use of a high flux atomic source based on a 2D-MOT [66], [67]. A complete description of the 2D-MOT set-up and its characterization can be found in [65], here we just mention its main characteristics.

In Fig. 3.2 we report a scheme of the implemented 2D-MOT. The vacuum system is derived from a parallelepiped made of titanium; the four lateral sides are closed with rectangular windows; one backside presents a circular window while the opposite backside has a hole which connects the chamber to the rest of the vacuum system and which permits the emission of a slow atom flux from the chamber. From the circular window passes a light beam which pushes the atoms towards the escape hole on the opposite side of the chamber. The trapping light is injected into the chamber from the four rectangular windows and travels perpendicularly with respect of the pushing beam.

The rubidium atoms are released as a vapour in the 2D-MOT chamber from a reservoir connected to the back of the trap; a valve allows to isolate the source of atoms if necessary. Vacuum is maintained with an ion pump with a 2 l/s pumping speed.

The magnetic field necessary for the transversal atom trapping is provided by two pairs of coils with rectangular shape and 100 windings, arranged in front of the four lateral windows. The coils, when connected in series, create a magnetic field gradient of 20 G/cm at the center of the 2D-MOT chamber.

3.1.4   Main pumping system

The required vacuum level in the apparatus is maintained with the use of a 75 l/s ion pump (Varian VacIon 75 Plus Star Cell, driver MidiVac) and a titanium sublimation pump (Thermionics SB-1020, driver Varian 9290023). The ion pump is connected to the detection chamber with large CF100 tubes. It is placed as far as possible from the experiment (55 cm) to allow the decay of the produced magnetic fields below 0.5 G. The titanium sublimation pump is used for pumping gases like H_2 or N_2.

3.1.5   Source masses and supports

One of the distinguishing features of the MAGIA-Adv apparatus is the presence of two sets of source masses arranged symmetrically on two holders around the interferometric tube. The source masses are used to modulate the gravitational field probed with the atoms and they played a crucial role in the determination of the Newtonian gravitational constant G [21].

The sensitivity and accuracy achievable in the *G* measurement depends on the knowledge of the source mass distribution. For this reason particular care was devoted in the choice of the source masses material and a thorough characterization of the position, geometrical shape and density distribution was performed; lots of details about these characterizations can be found in [38], [63]–[65], here we just present their main properties.

The source masses are 24 tungsten cylinders with base diameter of 100 mm and height of 150 mm. They are divided in two identical sets and are disposed symmetrically around the interferometric tube on two holders (see Fig. 3.1). The mass holders and elevator are designed to be strong enough to hold the cylinders without observable bending or deformations and with independent positioning control for the two sets of source masses; they can move vertically along the interferometric tube with high accuracy. The holders are two disk-shaped platforms with a hole in the center large enough to fit the interferometric tube. The movement of the platforms is realized with two pairs of 480 mm long precision screws with a diameter of 15 mm and a pitch of 10 mm. The rotation of each screw is controlled by a step motor able to reach a 1.7 μm resolution in the vertical displacement of the source masses. The vertical position of the platforms is monitored with an optical ruler with an accuracy and reproducibility of 1 μm.

3.2   Control system

The timing of the experimental sequence poses stringent requirements on the experiment control system in terms of temporal precision. For most experimental actions a precision of 100 μs is required, but a much higher resolution is needed for the interferometric pulse sequence (100 ns).

We implement a software control system in which the particular experimental sequence to run can be directly programmed. Due to the stringent requirements on timing, the control system is based on Real Time Application Interface LINUX [68].

The communication between the control computer and the instrumentation is realized with the use of three boards:

- 2 general purpose Input/Output boards Measurement Computing PCI-DAS 1002 with 24 digital I/O channels, 2 DAC channels and 8 ADC channels used for data acquisition.

- one IEEE-488 control board.

The interferometer pulse sequence is programmed via GPIB on an arbitrary waveform generator (AWG) which is then triggered via a digital channel. With this configuration the actual timing of the interferometric pulses is managed by the AWG and the needed time resolution is reached. The time base of this AWG is phase locked to a common 10 MHz reference which is used also for the phase locking of the Raman lasers (see the next section).

3.3 Laser system

During the experimental sequence ^{87}Rb atoms are manipulated both on the external and internal degrees of freedom by exploiting the interaction of the atoms with laser light. The manipulation processes are controlled by tuning the emission frequency and intensity of the various lasers described in this section.

In our set-up the most used transition for the ^{87}Rb manipulation is the D2 line ($|5^2S_{1/2}, F\rangle \rightarrow |5^2P_{3/2}, F'\rangle$) which frequency from now on we label as $\nu_{F\rightarrow F'}$. The wavelength required to excite this transition is $\simeq$780 nm which is easily produced using standard semiconductor laser diodes (LDs). For this reason the majority of the laser sources of the MAGIA-Adv apparatus are derived from this kind of technology. The remaining light sources are obtained from fibre lasers with an emission centred at 1560 nm; the light from these sources is then doubled in frequency to obtain the required wavelength for the ^{87}Rb manipulation.

Standard LD sources are cheap and easy to use but present the drawback of having a spectral emission width ~ 40 MHz, i.e. larger than the natural width of the D2 atomic transition ($\Gamma \simeq 6$ MHz). However it is possible to increase the spectral purity of the laser emission mounting the LD in an external cavity configuration (ECDL configuration)

External cavity diode lasers

A standard LD can be mounted in the external cavity configuration with the addition of two optical elements: an external resonant cavity which produces an optical feedback on the LD and a wavelength selector element (e.g. a diffraction grating or an interference filter) which allows the fine frequency tuning of the light emission. Due to the optical feedback, the external cavity reduces the threshold current for laser action of the diode, narrows the laser linewidth and provides broad tunability of the laser emission.

When mounted on an ECDL configuration the source linewidth can be expressed as [69]

$$\Delta\nu_{\text{ECDL}} = \left(\frac{nl}{L}\right)^2 \Delta\nu_d, \tag{3.1}$$

with n the diode refractive index, l the diode internal cavity length, L the external cavity length and $\Delta\nu_d$ the LD original linewidth. Using typical values ($n = 2$, $l = 1$ mm, $L = 10$ cm) the linewidth reduction can be more than a factor 100.
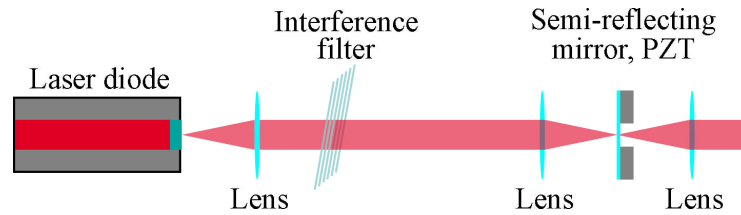
FIGURE 3.3: Schematic representation of the ECDL configuration used for the LDs of the MAGIA-Adv apparatus. The wavelength selection is guaranteed by the interference filter, while the optical feedback on the LD is provided by the semi-reflecting mirror. The semi-reflecting mirror is mounted on a piezo-electric actuator which allows to change the cavity length. The transmitted portion of the beam from the semi-reflecting mirror is finally collimated and constitutes the output of the ECDL.

The mode of emission in an ECDL depends on the LD gain profile, the internal cavity modes and the external cavity modes. Since the gain profile of LDs is broad, several modes might experience similar gain and multi-mode emission might occur. The introduction of a frequency selective optical element can avoid this problem by giving different weight to adjacent internal cavity modes. Furthermore, the external cavity allows accurate frequency control by adjusting the cavity length with a piezoelectric crystal (PZT).

One of the most common ECDL set-up is the Littrow configuration [70]. In this scheme the LD output beam is collimated and sent on a diffraction grating; the first diffracted order is then used as optical feedback while the zero order constitutes the output beam from the ECDL system. The selected wavelength $\lambda = 2d \sin(\alpha)$ depends on the grating line spacing d and on the incident angle α which equals the angle of first order diffraction.

We note that in the Littrow configuration the diffraction grating carries out the double task of providing the optical feedback on the LD and managing the frequency selection of the light emission. This aspect does not works favourably in terms of long term frequency stability[1]. For this reason in the MAGIA-Adv experiment, where is necessary to achieve long integration times without frequent unlocks of the lasers, a different and more stable ECDL configuration is currently employed. In the adopted ECDL a partially reflecting mirror is used to produce the optical feedback on the LD, while an interference filter provides the wavelength selection [72]. Fig. 3.3 shows a schematic view of the optical elements involved in this configuration which is referred to as Filter External Cavity Laser (FECL).

The FECL scheme has several advantages: it preserves the LD injection even in presence of cavity misalignments, the movement of the semi-reflecting mirror does not change the direction of emission and finally, since the used interference filters have a maximum transmission acceptance angle of $\pm 1°$, the selected frequency will be less sensitive to mechanical misalignments of the wavelength selecting element if compared to the sensitivity obtained with Littrow schemes. Indeed in the Littrow configuration we achieve a sensitivity to mechanical misalignments of the diffraction grating of $(d\lambda/d\theta) \sim 1.4$ nm/mrad, while with an interference filter we obtain a sensitivity of $(d\lambda/d\theta) \sim 23$ pm/mrad [73].

---

[1]Another disadvantage of the standard Littrow configuration is the change in emission directionality when the frequency is tuned by changing the incidence angle on the grating. However this problem can be solved with a more complex Littrow mounting [71]
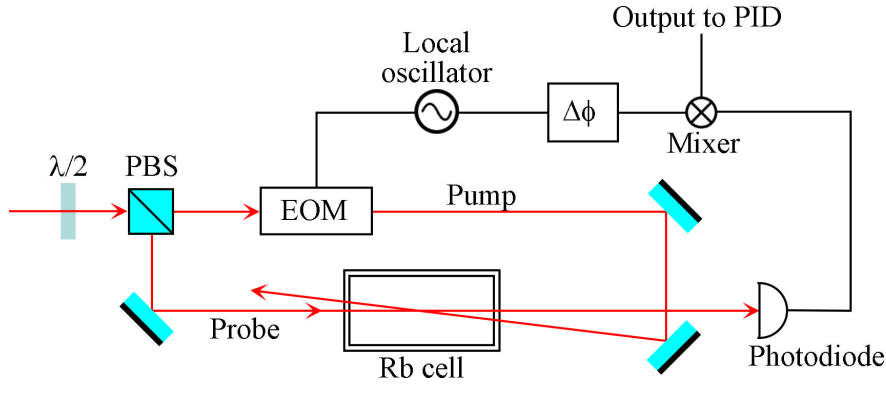
FIGURE 3.4: Scheme of the MTS technique. We show in red the laser optical path, while in black the electronic links. A first polarizing beam-splitter (PBS) divides the laser beam in two parts: the Pump beam and the Probe beam. The Pump beam is modulated with an Electro-Optic modulator (EOM) and intersects the Probe beam inside a rubidium spectroscopy cell. The modulation is transferred to the probe beam which is then detected with a photodiode; the signal is then demodulated with a mixer. The output of the mixer is processed in a Proportional-Integral-Derivative (PID) controller which generates the feedback signal for the laser source.

To stay in resonance with a ^{87}Rb D2 transition a laser cannot drift in frequency more that the natural linewidth $\Gamma \simeq 6$ MHz. Since the emission of a free-running ECDL will drift or jump by up to a few GHz per day it is necessary to stabilize (lock) the laser frequency to an atomic resonance or to some other laser already locked[2].

In order to lock the frequency of a laser to that of a reference oscillator it is necessary to measure the frequency difference between the two and to convert this difference into a voltage with zero-crossing at the desired locking point. This voltage signal can therefore be used to produce a feedback on the laser.

In the MAGIA-Adv apparatus one laser is directly locked to the ^{87}Rb D2 transition $\nu_{2\to3}$ through the technique of Modulation Transfer Spectroscopy (MTS) [75], [76]. All the other light sources are stabilized with respect to this reference oscillator.

Modulation Transfer spectroscopy

The Modulation Transfer technique is a particular kind of frequency modulation spectroscopy which is based on the modulation of the spectroscopy laser with a frequency ω_m and the subsequent demodulation of the spectroscopy signal with the same frequency ω_m.

The MTS technique is particularly suited for the frequency lock of lasers on atomic transitions, because it is able to generate signals with dispersive trends as a function of the laser frequency without any residual background. For this reason, the zero crossing of the dispersive electrical signal precisely corresponds to the atomic transition which generated it.

The conceptual scheme of this technique is reported in Fig. 3.4. The light beam from the spectroscopy laser is split with a polarizing beam-splitter (PBS) cube in

---

[2]Lots of techniques to control the frequency and the phase of a laser oscillator can be found in [74]

order to obtain the classical Probe/Pump geometry of sub-Doppler spectroscopy. The Pump beam is then frequency modulated with the use of an Electro-Optic modulator (EOM), which receives an external RF signal at frequency ω_m produced by a stable electronic oscillator.

The electric field of the Pump beam after the modulation can be written as a term at the carrier frequency ω_c plus side bands separated by the modulation frequency ω_m

$$E = E_0 \left[\sum_{n=0}^{\infty} J_n(\delta) \sin(\omega_c + n\omega_m)t + \sum_{n=1}^{\infty} (-1)^n J_n(\delta) \sin(\omega_c - n\omega_m)t \right], \qquad (3.2)$$

with δ the modulation index and $J_n(\delta)$ the Bessel function of order n. Assuming $\delta < 1$, the spectral composition of the beam is given by a strong carrier component, with frequency ω_c plus two other weaker components with frequency $\omega_c \pm \omega_m$ (we can therefore neglect all the components with $n > 1$ in the above equation).

At the output of the modulator, the Pump is sent through a heated and magnetically shielded rubidium vapour cell for optically pumping the atoms. In its path inside the cell, the Pump beam intersects the counter-propagating Probe beam which has no frequency modulation. At this point, due to the nonlinear behaviour of the absorber, the modulation of the Pump beam is transferred also to the Probe beam [75], [77]. One of the major advantages of the process is that this modulation transfer happens only when the sub-Doppler resonance condition is exactly verified. For this reason, any thermal background of the produced dispersive signal is zero.

After traversing the rubidium cell, the Probe beam is detected with a fast photodiode which reveals a beat note signal between the side bands produced in the vapour and the carrier frequency of the Probe beam. The output of the photodetector is a signal at the modulation frequency ω_m [78]

$$\begin{aligned} S(\omega_m) = \frac{C}{\sqrt{\Gamma^2 + \omega_m^2}} & J_0(\delta) J_1(\delta) \times \\ & \times \Big[\left(L_{-1} - L_{-1/2} + L_{1/2} - L_1 \right) \cos(\omega_m t + \phi) + \\ & + \left(D_1 - D_{1/2} - D_{-1/2} + D_{-1} \right) \sin(\omega_m t + \phi) \Big], \end{aligned} \qquad (3.3)$$

where

$$L_n = \frac{\Gamma^2}{\Gamma^2 + (\Delta - n\omega_m)^2}, \qquad D_n = \frac{\Gamma(\Delta - n\omega_n)}{\Gamma^2 + (\Delta - n\omega_m)^2},$$

with Γ the natural width of the atomic transition, Δ the laser frequency detuning from the atomic transition and ϕ an additional phase with respect to the modulation signal applied by the external oscillator. Finally the C constant represents the properties of the medium and the Probe beam which do not depend on the already expressed parameters.

The sine term, i.e. the quadrature component of the signal is a consequence of the absorption part of the sub-Doppler signal, while the cosine term, i.e. the in-phase component represents the dispersive part of the sub-Doppler signal. With a mixer it is possible to recover the quadrature or in phase components of $S(\omega_m)$, acting on the phase of the external oscillator signal. However, both of them have a dispersive trend (see Fig. 3.5) and the zero crossing corresponds to the resonance frequency of the atomic transition. This characteristic makes them particularly suited to be used as locking signals for the stabilization of lasers on atomic transitions. The dispersive
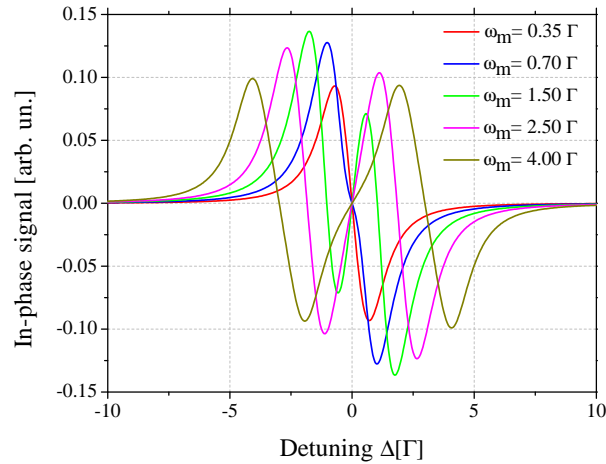
FIGURE 3.5: Theoretical calculation of the in-phase components of the photo-diode signal, versus the laser detuning Δ with respect to the atomic transition. The signals are calculated for different values of the modulation frequency ω_m / Γ.

signal is then processed with a Proportional-Integral-Derivative (PID) controlled to produce the feedback signal on the laser source.

Phase stabilization

In Sec. 2.1.2 we presented the formalism for Raman transitions and saw that to connect the two hyperfine levels of ^{87}Rb (F=1→F=2) the frequency difference between the two exciting lasers must be the one of the hyperfine transition, i.e. 6.834 GHz. For an atom interferometer the relative phase between the Raman lasers is also a crucial parameter to control (see Sec.2.2.2), since it affects directly the interferometer phase. For this reason a phase lock between the two Raman lasers is necessary for the interferometer operation.

Like in the case of frequency locking, also for phase locking two oscillators is necessary to measure the phase difference between the two and to translate this difference into a voltage signal with zero crossing at the locking point which can be used to produce a feedback.

Fig. 3.6 reports the general scheme of a Phase-Locked-Loop (PPL). With such a scheme the phase of a noisy RF source can be stabilized with respect to a clean Local Oscillator (LO) signal. Let us consider a LO with frequency $\omega_{\text{LO}} = 2\pi f_{\text{LO}}$ and phase $\phi_{\text{LO}}(t) = 2\pi f_{\text{LO}} t + \phi_{\text{LO}}^0$ and a RF signal with

$$\omega_{\text{RF}} = 2\pi f_{\text{LO}} + 2\pi f_{\text{N}}(t), \qquad \phi_{\text{RF}}(t) = 2\pi f_{\text{LO}} t + 2\pi \int_0^t f_{\text{N}}(t') dt' + \phi_{\text{RF}}^0,$$

with $f_{\text{N}}(t)$ the frequency noise. The PLL is realized with a phase detector which converts the phase difference $(\phi_{\text{LO}}(t) - \phi_{\text{RF}}(t))$ into a voltage with a gain k_{PD}. The signal at the output of the phase detector is the error signal

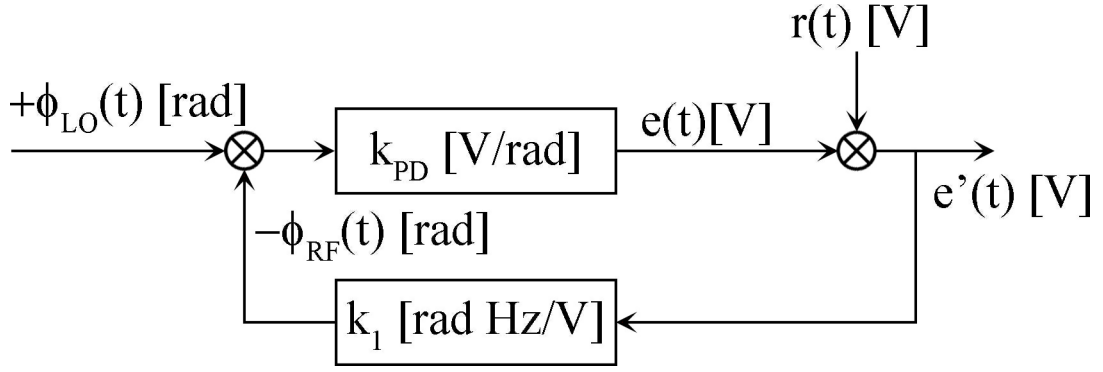$$e(t) = k_{\text{PD}}(\phi_{\text{LO}}(t) - \phi_{\text{RF}}(t)),$$

FIGURE 3.6: Conceptual scheme of a Phase-Locked-Loop (PLL). The Phase Detector (PD) converts the phase difference between the local oscillator and a RF signal ($\phi_{LO} - \phi_{RF}$) into an error signal with a gain k_{PD}. The signal $r(t)$ represents the noise added by the loop, while $e'(t)$ is the correction signal which is converted to a frequency with gain k_l.

to which we add a noise $r(t)$ due to the loop itself

$$e'(t) = e(t) + r(t).$$

The above error signal is used as feedback on the RF signal. For the stabilization of a laser oscillator the error signal is directed to the laser driver which in a time τ converts it to a frequency change with a gain k_l

$$\delta f(t) = \frac{k_l}{2\pi} e'(t). \tag{3.4}$$

When the correction is active the RF phase becomes

$$\phi_{RF}(t + \tau) = 2\pi f_{LO}(t + \tau) + k_l \int_t^{t+\tau} e'(t)dt + \phi_{RF,0}. \tag{3.5}$$

We note that since the feedback is on the laser frequency the loop includes an integrator. After a time τ the signal $e'(t)$ will change by

$$
\begin{aligned}
e'(\tau) - e'(0) &= (e(\tau) + r(\tau)) - (e(0) + r(0)) \\
&= k_{PD}(\phi_{LO}(\tau) - \phi_{RF}(\tau)) - k_{PD}(\phi_{LO}(0) - \phi_{RF}(0)) + r(\tau) - r(0) \\
&= -k_{PD}k_l \int_0^\tau e'(t)dt + r(\tau) - r(0).
\end{aligned}
$$

Switching to frequency space with the Laplace transform of the above signal we obtain for $f \neq f_{LO}$

$$E'(f) = \frac{R(f)}{1 + k_{PD}k_l/(if)}, \tag{3.6}$$

where the capital letters indicate the transforms. The frequency response of the loop is like a first order low pass filter and the unity gain frequency of the loop is $f_1 = k_{PD}k_l$.

The central part of the PLL is the phase detector which can be analog or digital. An analog phase detector is a mixer which multiplies the RF signal $s_{RF} = A_{RF}\cos(\phi_{RF}t)$ and the LO signal $s_{LO} = A_{LO}\sin(\phi_{LO}t)$ with a gain k_m. Setting $\phi_{LO,0} =$

0 and $\phi_{RF,0} = \pi/2$ the output signal from the mixer is

$$m(t) = k_m A_{RF} A_{LO} \sin(\phi_{LO}(t)) \cos(\phi_{RF}(t))$$
$$= \frac{1}{2} k_m A_{RF} A_{LO} \Big(\sin(\phi_{LO}(t) - \phi_{RF}(t)) + \sin(\phi_{LO}(t) + \phi_{RF}(t)) \Big)$$
$$= \frac{1}{2} k_m A_{RF} A_{LO} \Big(\sin(\phi_N(t)) + \sin(2\omega_{LO} + \phi_N(t)) \Big).$$

The second term can be filtered out with a low pass filter and the remaining term depends only on the phase difference between the two oscillators. For small phase differences the sine can be linearised and the error signal is proportional to the phase difference

$$e(t) = m(t) = k_{PD}(\phi_{LO}(t) - \phi_{RF}(t)), \tag{3.7}$$

with $k_{PD} = \frac{k_m A_{RF} A_{LO}}{2}$.

When in presence of big phase differences ($> \pi$) the error signal changes sign (due to the sine term). The feedback increases the phase difference between the oscillators and relocks at 2π; the locking range is then limited to $\pm\pi$. An analog phase detector has the advantages of a fast response and low noise.

The locking bandwidth f_{BW} of a phase lock is limited by the delay τ which the signal acquires in one loop of correction ($f_{BW} < 1/(2\tau)$). Furthermore, the locking bandwidth defines the capture range of our PLL, i.e. the maximum frequency difference between the two oscillators which can be corrected. Indeed if two lasers have a frequency difference Δf they will acquire a phase difference of 2π in a time $T = 1/\Delta f$. During this time the analog phase detector will produce a null error signal since the sine averages to 0. This means that in order to capture the correct lock the loop has to correct the frequency difference in order to stop the phase deviation before it arrives at 2π.

For the PLL of the Raman lasers we use a digital Phase and Frequency Detector (PFD). The PFD compares the digitalized RF and LO signals and generates an output signal in its two output channels when the phase or frequency of both signals differ. If the phase of the LO signal leads with respect to the RF signal the pulse difference between the signals is sent to the PFD output channel UP. If the opposite happens the difference signal is sent to channel DOWN. With this discrimination the difference between the signal is either positive or negative (the output signal is zero if there is no phase difference). If the phase difference between the two signals is $< 2\pi$ the error signal is proportional to the phase difference

$$e(t) = k_{PD}(\phi_{LO}(t) - \phi_{RF}(t)). \tag{3.8}$$

Differences in frequency are treated in a similar way; depending on which frequency is higher the UP or DOWN channel is used as output channel. The ability to correct also for frequency changes ensure a big capture range.

Let us now start to describe all the main laser light sources used in the MAGIA-Adv experiment.

3.3.1 Reference laser system

In order to have well defined light frequencies a first LD, the Reference laser (ADL-78901TX, Roithner Lasertechnik), is frequency stabilized to a ^{87}Rb sub-Doppler transition and constitutes the frequency reference for all the remaining lasers.

The LD is mounted in the FECL configuration and provides ~ 100 mW of output power at 780 nm. The laser emission has its frequency increased of +184.2 MHz with a double pass through an Acousto-Optic Modulator (AOM) and then performs a Modulation-Transfer Spectroscopy (MTS) on a rubidium sample. For this laser the modulation frequency sent on the EOM (Nova Phase) is $\omega_m = 5$ MHz and the rubidium vapour cell is held at a temperature of about 35°C.

We use a double loop-control to lock the laser frequency on the desired atomic resonance. A low frequency loop (bandwidth up to 1 kHz) is realized with a feedback on the piezoelectric of the semi-reflecting mirror which controls the cavity length in the FECL laser system. A second fast frequency loop (bandwidth up to 120 kHz) is realized acting on the laser driving current.

The Reference laser is locked on the sub-Doppler resonance corresponding to the transition $\nu_{2\to3}$, but due to the double pass in the AOM the actual emission frequency is $\nu_{\text{ref}} = \nu_{2\to3} - 184.2\text{MHz}$.

Part of the light of the Reference laser is picked-up with a beam-splitter before the double pass through the AOM for frequency locking all the other laser sources.

3.3.2   Cooling and Re-pumping laser systems

For trapping and cooling ^{87}Rb atoms we need light of two different frequencies [79] which are provided by two independent laser systems. These two sources are both necessary to realize an optimized cooling and trapping process in the 3D-MOT. We use a first light source, the Cooling laser, with an emission red detuned from the atomic transition $\nu_{2\to3}$ of about $3\Gamma = 3 \cdot 6.065$ MHz (Γ is the natural transition width of the ^{87}Rb D2 line) together with a second source, the Re-pumper laser which prevents the accumulation of atoms in dark states for the cooling light, i.e. in states which do not interact with the Cooling laser. This accumulation happens because when an atom of ^{87}Rb interacts with the cooling radiation, instead of being excited in the level $|5P_{3/2}, F' = 3\rangle$ can end up in $|5P_{3/2}, F' = 2\rangle$. From this level the atom can decay in the fundamental state $|5S_{1/2}, F = 1\rangle$. When this happens the atoms cannot interact with the cooling light any more and tend to accumulate in this state, i.e. the level $|5S_{1/2}, F = 1\rangle$ is a dark state for the cooling radiation. Furthermore, since the absorption and spontaneous emission processes happen with a rate Γ, all the atoms would rapidly end up in this state with no possibility of participating again in the cooling process. This problem is solved with the addition of the Re-pumping light; its frequency is slightly detuned from the $\nu_{1\to2}$ transition and can transfer the atoms from the dark state $|5S_{1/2}, F = 1\rangle$ to the state $|5P_{3/2}, F' = 2\rangle$, draining the dark state.

The Cooling laser is also used for the vertical launch of the atomic samples. This requires a differential control of the frequencies of the upwards and downwards propagating beams of the 3D-MOT.

The cooling laser system consists of a FECL laser diode (L785P090, Thorlabs) which injects a 1 W tapered amplifier (EYP-TPA-0780, Eagleyard Photonics Gmbh). The amplifier emission is split in two beams which propagate in two independent optical paths. Each beam first passes through a double pass AOM (AOMO 3080-122, Crystal Technology, Inc) for independent frequency control and then is injected in an optical fibre which delivers the light to a three-way splitter for the production of the three upward/downward 3D-MOT beams. The output from the three-way splitter is then coupled to the trap chamber. During the trapping phase of the experimental sequence the two AOMs are driven with the same radio-frequency signal of +83.4 MHz, but for the launch steps the two driving RF signals have a frequency difference proportional to the desired launch velocity.

The Cooling laser frequency is stabilized against the Reference laser. Indeed a minor portion of the Cooling laser emission is picked-up before the tapered amplifier injection, superposed with light from the Reference laser and sent on a fast photodiode (Hamamatsu G 4176-03) to produce a beat note signal. The beat note is compared with a RF signal at 194 MHz in a PFD that provides the PLL error signal. The loop is finally closed acting both on the diode current and on the FECL cavity PZT voltage.

The Re-pumping laser system is composed of two diode lasers arranged in a Master/Slave configuration. The Master Re-pumper laser is a FECL diode (L785P090, Thorlabs) and his frequency is stabilised on the $\nu_{1\to 2}$ transition. Part of its emission is superposed with light from the Reference laser on a beam-splitter and their beat note is then recorded with a fast photodiode. The beat note is then down-converted in a mixer with the third harmonic of a 2216.6 MHz RF signal produced with a programmable synthesizer (ADF4360-1 stabilized VCO). The signal is finally compared with a 40 MHz reference oscillator in a PFD to obtain the error signal for frequency locking the laser. Also in this case we have a low frequency servo loop acting on the cavity PZT voltage and a high frequency correction loop acting on the laser driving current. The frequency of the Master Re-pumper is ($\nu_{1\to 2} - 62.4$ MHz). A portion of its light is used to inject the Slave Re-pumper while the rest injects a 1 W tapered amplifier (EYP-TPA-0780, Eagleyard Photonics Gmbh).

The amplifier emission is sent through a double pass AOM and shifted of -172.2 MHz in order to reach a frequency ($\nu_{1\to 0} - 5.5$ MHz). This light is used to blow away unwanted freely falling atoms in the $F = 1$ state just after the launch and during the vertical velocity selection.

The Slave Re-pumper (Sharp GH0781JA2C) is injected using the side port of an optical isolator. The output beam is sent to an AOM driven with a +68.0 MHz RF signal. The resulting light frequency is ($\nu_{1\to 2} + 5.6$ MHz) and it is used as re-pumper during atom trapping and during the detection procedure.

3.3.3 2D-MOT laser system

The 2D-MOT laser system is composed of two laser sources. The first one provides the cooling and pushing light for the 2D-MOT and it is based on a 1 W tapered amplifier (EYP-TPA-0780, Eagleyard Photonics Gmbh) injected with the beam from a FECL diode laser (L785P090, Thorlabs). The amplifier output is split and used for the cooling beams of the 2D-MOT trap and for the pushing beam. The laser is locked in frequency with respect to the Reference laser with a double control loop on the FECL cavity PZT voltage and on the laser driving current.

The second source is a re-pumper laser obtained injecting a LD with a portion of the light from the Slave Re-pumper. The injection is performed using the side port of an optical isolator.

3.3.4 Detection laser system

We produce the detection light with a laser diode (Sharp GH0781JA2C) directly injected with the Reference laser light. For the injection we use the side port of the Detection laser optical isolator. The output beam from the Detection laser is sent through a double pass AOM and shifted of +183.6 MHz resulting in a frequency $\nu_{\text{det}} = \nu_{2\to 3} - 800$ kHz. The light is finally injected in two different optical fibres; one for the atomic state detection after the interferometric sequence which is delivered
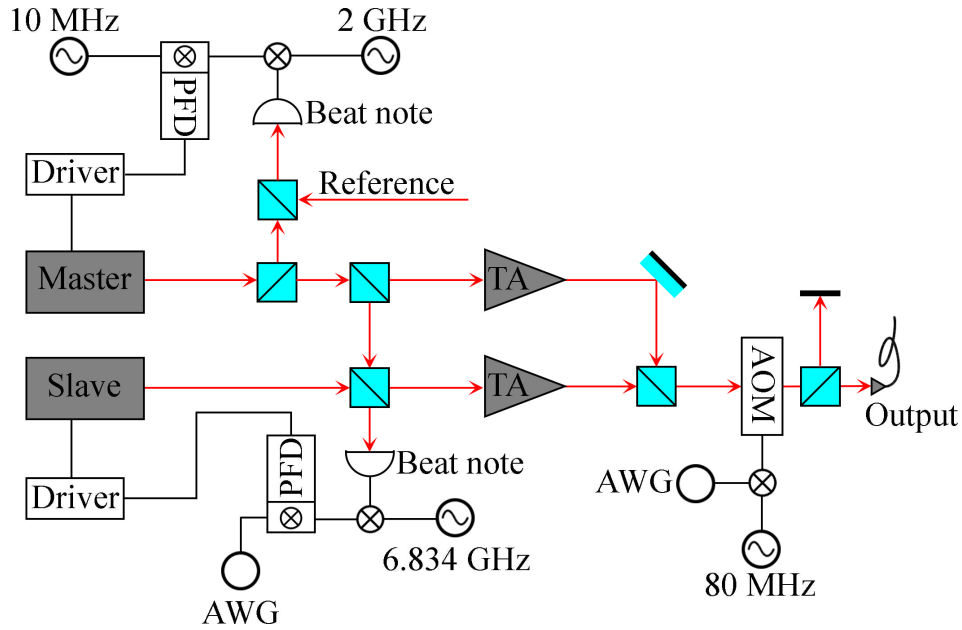
FIGURE 3.7: Conceptual scheme of the Raman laser system. Two FECL lasers are arranged in a master-slave configuration and inject two independent 1 W tapered amplifiers. The Master Raman emission frequency is stabilised with respect to the Reference laser frequency with a detuning of $\sim$2 GHz. The Slave Raman emission frequency and phase are stabilized with respect to the Master Raman. The frequency difference between the two lasers is the hyperfine frequency splitting of the ^{87}Rb fundamental state (6.834 GHz). The AOM is used for shaping the pulses before the delivery on the atoms. Before the fibre injection the Raman beam polarization is filtered with a polarizing beam-splitter. The optical fibre which delivers the light to the atoms is polarization maintaining.

to the detection chamber and the other for vertically blowing away unwanted atoms in the $F = 2$ state during the vertical velocity selection procedure.

3.3.5   Raman laser system

The Raman laser system provides the light necessary to stimulate Raman transitions during the velocity selection procedure and during the interferometric sequence. It is composed of two phase-locked FECL diodes (L785P090, Thorlabs) organized in a Master/Slave configuration and two independent 1 W tapered amplifiers (EYP-TPA-0780, Eagleyard Photonics Gmbh). In Fig. 3.7 we report the schematic representation of this laser system.

Master Raman frequency lock

The frequency lock of the Master Raman laser is realized by superposing its light with the one of the Reference laser and by collecting the beat note signal on a fast photodiode (G4176-03, Hamamatsu). The beat note is down-converted using a mixer with the RF signal from a synthesizer (ADF4350, Analog Devices) centred at 2.0 GHz. The mixer output is then compared in a PFD with a stable 10 MHz signal. For this laser the lock acts only on the cavity PZT voltage (bandwidth of few kHz). The Master Raman frequency is therefore $\nu_{2\rightarrow 3} - 2.184$ GHz.

Slave Raman phase lock

For the phase locking of the Slave Raman laser a portion of its light is superposed with light from the Master Raman and the beat note is recorded with a fast photodiode (G4176-03, Hamamatsu). After an amplification stage the beat note at 6.834 GHz is down-converted by mixing it with the signal from a low phase noise microwave synthesizer (Anritsu MG3692A). The mixer output is again amplified and sent to a directional coupler (not shown in Fig. 3.7). The 10% output channel is used for signal monitoring, while the 90% channel is sent to a combined digital/analog PFD [80] together with a RF signal from an arbitrary waveform generator (AWG, Agilent 33600A Series) in sweep mode; the AWG is phase locked to the same 10 MHz time base used for the Master Raman locking. The AWG sweep is performed during the experimental sequence in order to compensate for the changing Doppler effect experienced by the freely falling atoms. The resulting error signal from the PFD is filtered and used to control the voltage applied on the cavity PZT of the FECL and the LD current.

The Raman lasers emission is amplified with two independent 1 W tapered amplifiers[3]. The two light beams are superposed on a polarizing beam-spitter and pass through an AOM (AOMO 3080-122, Crystal Technology, Inc) used for pulse timing control. This AOM basically works as a fast shutter which allows us to obtain short ($\sim 10\ \mu$s) light pulses with arbitrary time envelopes[4]. After the shaping AOM a PBS aligns the two beams polarizations. Finally the two beams are injected in a common polarization maintaining optical fibre; the fibre output passes through a Glan-Taylor polariser for additional polarization cleaning and is then collimated with a lens to a waist of $\sim$15 mm before entering the vacuum system from the bottom. The two Raman beams have the same linear polarization and propagate vertically. After traversing all the vertical length of the vacuum system the beams exit from the top, pass through a $\lambda/4$ wave-plate and are retro-reflected by a mirror thus obtaining a lin$\perp$lin polarization configuration in the interferometer region for the counter-propagating Raman couple.

The retro-reflection mirror is not seismically isolated but its alignment is controlled with a tilt-meter.

3.3.6 Bragg laser system

The Bragg laser system is responsible for producing the laser light required for the excitation of Bragg transitions during the interferometric sequence. Since the effective Rabi frequency for this kind of multi-photon processes has a strong dependence on laser intensity (see Eq. 2.43), in order to efficiently drive high-order Bragg transitions high power laser sources are mandatory. Fig. 3.8 shows a schematic view of the optical set-up for the Bragg laser system. We use a seed laser source (NP Photonics, Rock$^{\text{TM}}$ source) to inject a high-power Erbium doped fibre amplifier (EDFA) (Keopsys, CEFA-C-BO-HP). The seed laser has an emission centred around 1560 nm and can be tuned either with a piezo control or with temperature. The light from this source injects an EDFA with a peak emission power of 15 W. The amplified light is then frequency doubled using two periodically-poled lithium niobate crystals (PPLN) and stabilized in frequency with a feedback loop on the piezo actuator

---

[3]Recently we added the possibility of controlling the output intensity of the amplifiers with a digital servo loop acting on the amplifiers driving current (bandwidth 3 Hz).

[4]When implementing Raman transitions we will always use square pulses. However for Bragg transitions the pulse timing control is critical for a high transfer efficiency.
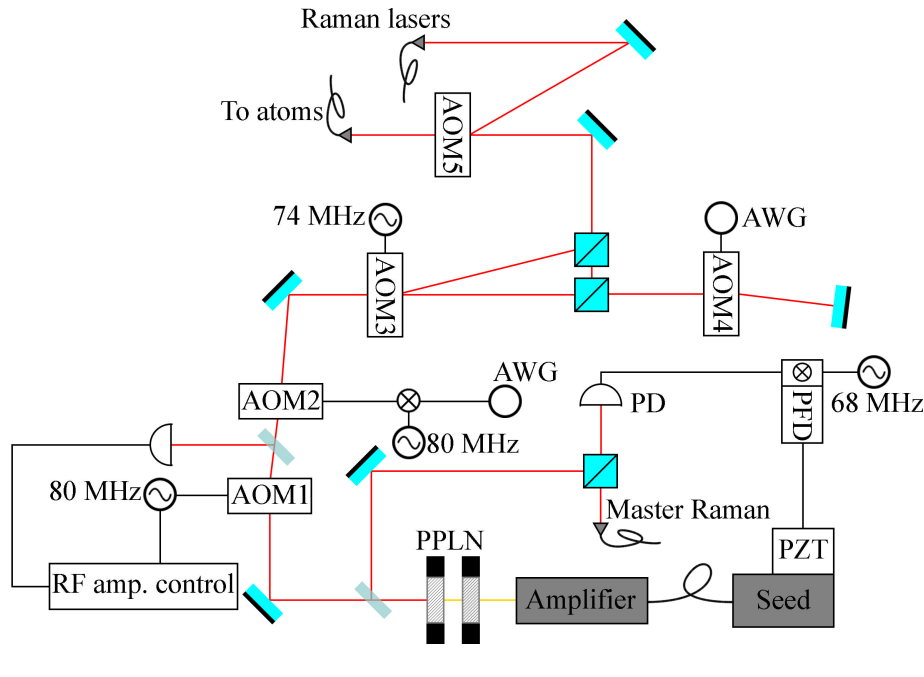
FIGURE 3.8: Schematic representation of the optical set-up for the production of the Bragg beams. The light is derived from an IR seed laser amplified and then frequency doubled with two PPLN crystals. The seed laser emission frequency is stabilised with respect to the Master Raman emission with a servo loop acting on the PZT of the seed laser cavity. AOM 1 is used to stabilize the emission power, AOM 2 controls the temporal profile of the interferometric pulses, AOM 3 generates the two Bragg beams while AOM 4 steers the frequency difference to account for the change in the Doppler effect during the atomic free fall. The two interferometric beams are superimposed on the last beam splitter and injected in a polarization maintaining optical fibre which delivers the light to the experiment. AOM 5 allows us to select wether to switch on the Bragg beams or the Raman beams during the experimental sequence.

of the seed laser. The seed frequency is locked with respect to the Master Raman laser frequency by detecting the beat note signal between the two sources with a fast photodiode. The beat note is then compared with a 68 MHz RF signal in a PFD which produces the error signal.

The amplifier output power is monitored right after AOM1 where a little portion of light is picked-up and sent on a photodiode. The signal from this photodiode is then used to stabilize the power output with a servo loop acting on the amplitude of the RF signal which drives AOM1. AOM2 (AOMO 3080-122, Crystal Technology, Inc) is used as a fast shutter for the Bragg light and to shape the temporal profile of the interferometric pulses. AOM3 basically works as a beam-splitter and defines the two laser beams needed for the Bragg transitions. One of these beams is steered in frequency with a double pass in AOM4 which is driven by a linear frequency sweep from an AWG (Agilent 33600A Series) to account for the changing Doppler effect of the freely falling atoms. Finally AOM5 is used as a selective shutter; when the driving RF signal is on, the Bragg beams are diffracted away from the optical fibre which delivers the light to the vacuum system and the Raman beams can reach the atoms (this happens during the velocity selection part of the experimental sequence); the opposite happens when the driving RF signal is off (this is the case during the interferometric interrogation part of the experimental sequence).
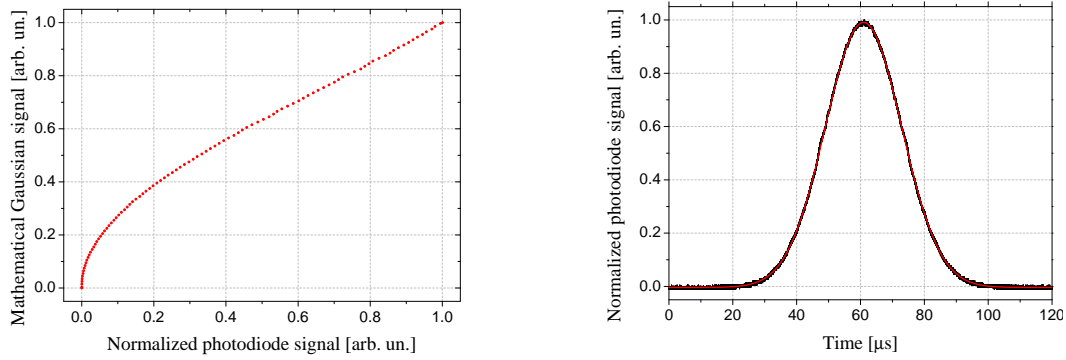
FIGURE 3.9: (Left) Calibration curve obtained sectioning the measured transfer function in 100 points and averaging in each interval. When applied to the desired waveform each point of the curve is linearly interpolated. (Right) Normalized light signal measured with a photodiode after the calibrated AOM. In black we report the measured data points, while in red a gaussian fit of the data. The AOM was driven with a Gaussian signal with $\sigma = 12$ μs while from the fit we derive a $\sigma = 11.98$ μs for the measured output.

Light is delivered to the atoms with a polarization maintaining optical fibre. The output of this fibre is filtered with a Glan-Taylor polariser and collimated to a beam waist of about 20 mm; each Bragg beam can reach a maximum power of about 500 mW when delivered on the atoms. Before entering the apparatus from the bottom the Bragg beams traverse a $\lambda/4$ wave-plate. They are finally retro-reflected from the top mirror after traversing an additional $\lambda/4$ wave-plate in order to have a $\sigma^+ - \sigma^-$ polarization configuration in the interferometer region for the counter-propagating Bragg beams.

With this set-up we were able to efficiently excite up to 3rd order Bragg transitions. The main limitations in achieving a higher diffraction order are found in the transversal temperature of the atomic cloud and in its transversal dimensions which forced us to use large, i.e. low intensity laser beams.

Calibration of the shaping AOM

Since for Bragg diffraction the temporal pulse shape is decisive for an efficient transition process, particular care was devoted to the realization of the optimal pulse shape. For this reason we developed a new calibration procedure for the shaping AOM (AOM2 in Fig. 3.8) which allowed us to have very accurate Gaussian pulses.

The old calibration procedure for the shaping AOM was realized with a polynomial fit of the AOM transfer function. The transfer function is obtained plotting the driving signal from the AWG, versus the signal from a photodiode which detects the light diffracted by the AOM.

The new calibration procedure does not rely on a polynomial fit any more to reproduce the transfer function. This time the measured transfer function is sectioned in 100 intervals; for each interval we calculate the average value of the mathematical signal and the experimental data and realize a calibration curve of 100 points which reproduce the original complete AOM transfer function (see Fig. 3.9 (left)). This calibration curve is then applied to the original mathematical signal to obtain

the desired output from the AOM[5].

Fig. 3.9 shows an example of a transfer function and of a Gaussian pulse with a time width of $\sigma = 12 \ \mu$s obtained with the new calibration procedure. We note that with this new calibration procedure the pulse shape can accurately reproduce a Gaussian envelope even on the tails of the pulse where the old calibration procedure failed.

---

[5]When producing the waveform that drives the AOM each point of the calibration curve is linearly interpolated
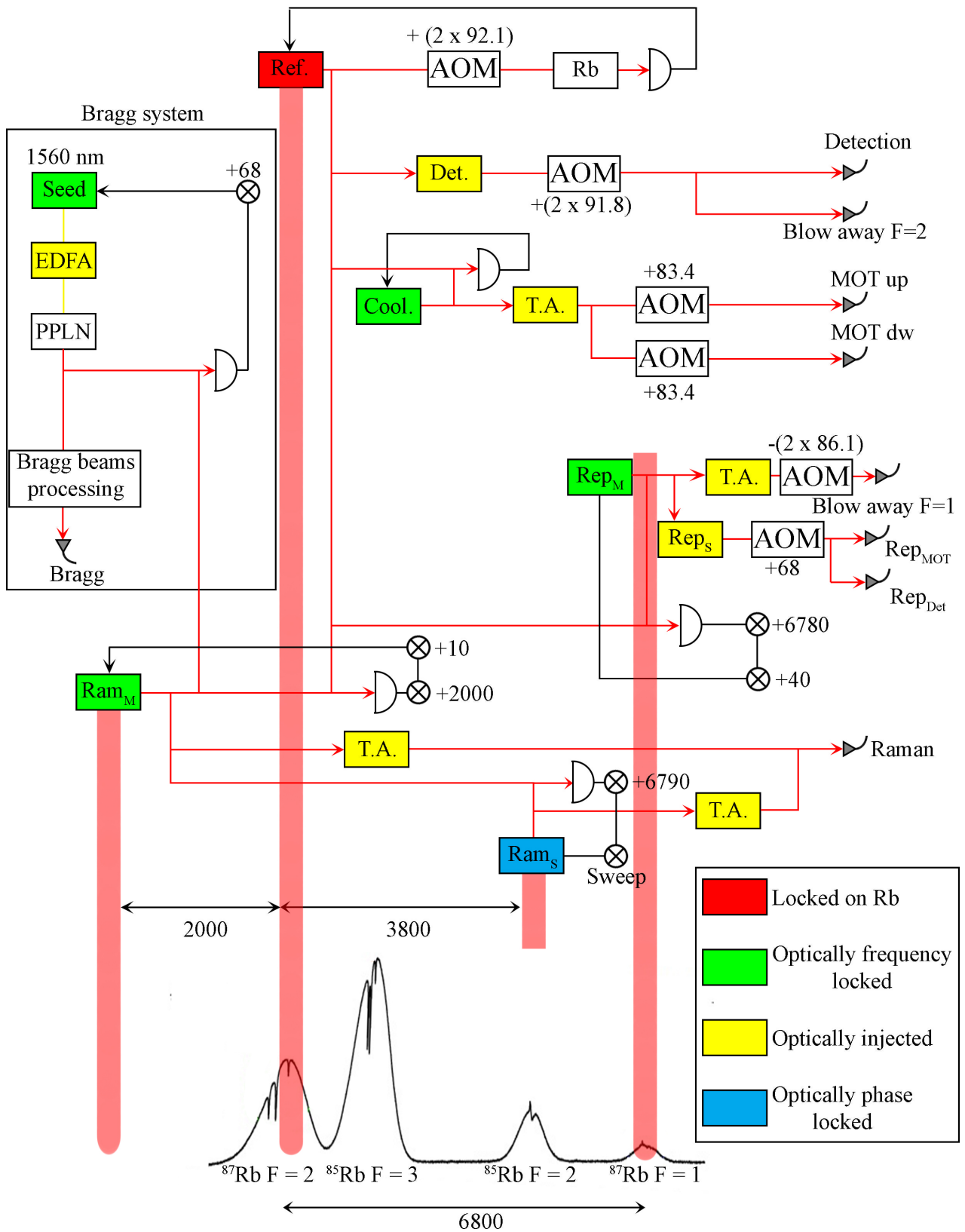
FIGURE 3.10: Summary of the main laser system. The 2D-MOT laser system is not shown. All the frequencies are measured in MHz.

Chapter 4

Main experimental sequence

In this chapter we describe the main experimental sequence, present some examples of the typical signals and introduce the data analysis procedure.

We will start with the atom trapping and cooling in the 3D-MOT providing also a conceptual description of the MOT underlying mechanisms. We will then present the launch technique used to obtain freely falling atomic samples inside the interferometric tube and the velocity and state selection procedure realized before the interferometric pulse sequence. We will continue introducing the interferometric sequence and the detection procedure realized at the end of the experimental cycle. Finally we present typical signals for both the Raman and the Bragg atom gradiometer together with the data analysis procedure.

4.1   Atomic trapping and cooling

The MAGIA-Adv apparatus is an AI realized with an atomic fountain of cold atoms [81]. The first step of the experimental sequence is therefore dedicated to the collection and cooling of the atomic ^{87}Rb sample inside a 3D-MOT [82]; the collected sample is then launched vertically with a moving optical molasses [83].

The underlying principle of the MOT is best described starting from a one-dimensional example [79] (see Fig. 4.1). We consider the interaction of two counter-propagating laser beams with a simple two-level atomic system with $F = 0$ and $F' = 1$. However, the principle discussed is applicable to any two-level system of the kind F, $F' = F + 1$. The confining potential is realized from the interplay between the effect of laser interaction and the effect of a magnetic gradient on the atoms. The two counter-propagating laser beams have the same frequency ω_L, red detuned from the resonant atomic transition $F = 0 \rightarrow F' = 1$ and opposite circular polarizations σ^+, σ^-. The magnetic field gradient is generated with two anti-Helmholtz coils; the coils generate a quadrupole magnetic field with a zero crossing exactly in the middle of the axis connecting the two coil centres, which we consider as the origin of the reference system ($z = 0$). Moving along the z axis the modulus of the magnetic field increases linearly with the distance from the origin, while the direction of the field inverts when the origin is crossed. In this configuration we have a linear magnetic field gradient capable of removing the degeneracy of the Zeeman magnetic sub-levels of the atomic state $F' = 1$.

Let us consider an atom in the fundamental state, which is on the right of the z axis origin ($z > 0$) and which moves away from the origin. The magnetic sub-level with $m_F = -1$ is lowered in energy due to the Zeeman shift caused by the external magnetic field and is brought closer to resonance with the laser beam of polarization σ^-, which propagates towards the origin. The atoms to the right of the origin will thus absorb more photons from the counter-propagating beam with σ^- polarization
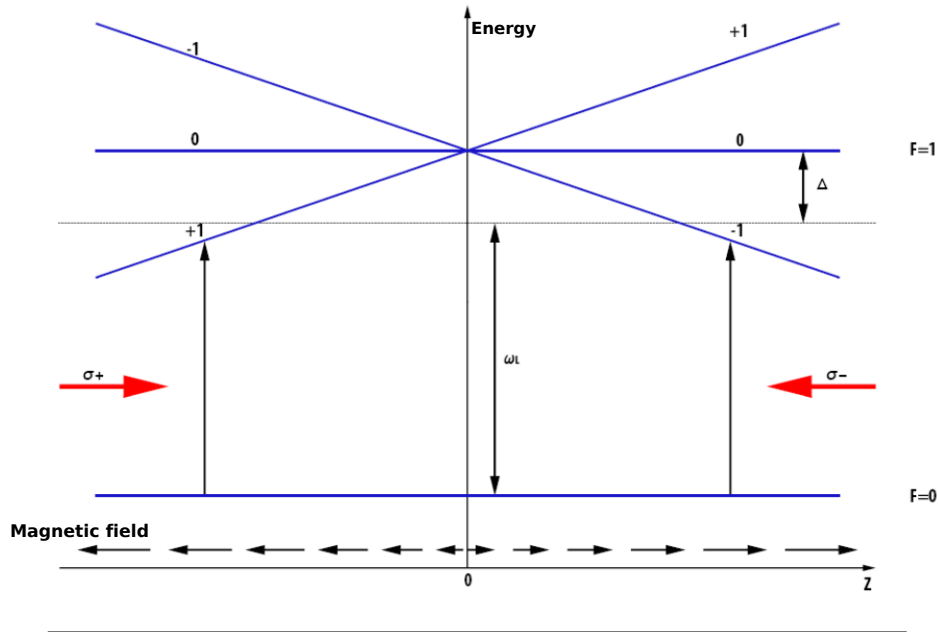
FIGURE 4.1: Scheme of the working principle of a one-dimensional MOT. In blue we indicate the energy levels of a two level atomic system with $F = 0$ and $F' = 1$. The counter propagating, circularly polarized laser beams are drawn in red. The frequency of the lasers is ω_L and it is red detuned with respect to the atomic resonance condition (in the absence of an external magnetic field). The black arrows at the bottom show the behaviour of the magnetic field generated by a pair of anti-Helmholtz coils.

rather than from the co-propagating beam with polarization σ^+. After an absorption process, the atom de-excite through spontaneous emission towards the fundamental level $F = 0$. Since the spontaneous emission is isotropic the final result of the process is that the atoms to the right of the origin feel a net force which pushes them towards $z = 0$ and vice-versa for the atoms to the left of the origin.

We note that in this configuration the result of the sole laser interaction is the production of a viscous damping force for the moving atoms (i.e. a force with modulus proportional to the atomic velocity) typical of optical molasses and capable of slowing down the atoms. Indeed due to the Doppler effect and the red detuning of the laser beams an atom has a higher probability of absorbing photons from the counter-propagating laser beam. This produces a net force opposite to the atom velocity. However only in presence of the magnetic field gradient there is also a confining potential, i.e. a force which depends on the atomic position and which always points towards the trap center. This is due to the spatially varying Zeeman effect which in turn produces a spatially varying excitation probability for the moving atoms (see Fig. 4.1). The total force exerted on the atoms can therefore be expressed as a term proportional to the atomic velocity, which constitutes the dissipative term responsible of the cooling, plus a term proportional to the distance from trap center which determines the trapping of the atoms.

In three dimensions the working principle is analogous, but instead of a single pair of counter-propagating laser beams there are three orthogonal pairs.

In our set-up, the loading rate of the 3D-MOT is enhanced with the use of a 2D-MOT. The trapping beams for our 3D-MOT are arranged in the usual $1 - 1 - 1$

configuration. Indeed our trap is composed of three orthogonal pairs of counter-propagating σ^+/σ^- polarized laser beams, tilted from the vertical direction (the vertical direction has to remain free for the injection of the interferometric beams). As already mentioned, the optical frequency of the three upper beams and of the three lower beams can be independently controlled; the detuning of the beams during trapping is -3Γ from $\nu_{2\to3}$. The beams are collimated ans have a waist of 11 mm. The maximum single beam intensity is 25 mW/cm^2 ($\sim 15 \, I_S$).

The quadrupole magnetic field is produced with a pair of coaxial coils in anti-Helmholtz configuration arranged in order to obtain the zero field point at the center of the laser beams crossing region. The coils have a circular shape with a radius of 7 cm; they have 50 windings and are separated by 16 cm. When operated with a 25 A current they produce an axial magnetic field gradient of 8.3 G/cm at the center (on the radial plane the gradient is half the axial one). The maximum capture velocity for our 3D-MOT is 22 m/s.

4.1.1 Sub-Doppler cooling and launch

After the 3D-MOT loading the next step in the experimental sequence consists in the further cooling of the atomic ensemble and in its vertical launch with a moving optical molasses [83].

During the loading the 3D-MOT beams have the same frequency. This produces an optical molasses which slows atoms down to a zero mean velocity in the laboratory reference frame. However if there is a relative frequency detuning between the three upwards and the three downwards propagating beams, the atoms will acquire a certain mean velocity v_z due to the Doppler effect and still be cooled. Basically the action of the detuning is to create a static optical molasses in the reference frame moving at velocity v_z with respect to the laboratory reference frame. In our set-up we apply a frequency detuning of $+\delta$ for the upwards propagating beams and a frequency detuning of $-\delta$ for the downwards propagating beams. Considering that the wave-vector of the 3D-MOT beams is tilted by an angle α ($\cos\alpha = 1/\sqrt{3}$) the launch velocity v_z is

$$v_z = \frac{\lambda\delta}{\cos\alpha}, \tag{4.1}$$

which corresponds to 1.35 m/(s MHz). In our usual experimental conditions the launch velocity is $v_z \simeq 4$ m/s.

At the start of the launch sequence the magnetic field of the 3D-MOT is turned off in $\sim 200 \, \mu$s while the beams detuning is increased from $\Delta = -3\Gamma$ to $\Delta = -3.8\Gamma$; the relative detuning δ is also added and the optical molasses starts to move vertically. At this point a polarization gradient cooling stage is applied in order to reach lower temperatures than what is possible in a standard optical molasses, i.e. lower than the Doppler temperature $T_D = \hbar\Gamma/(2k_B)$ ($\sim 140 \, \mu$K for the ^{87}Rb D2 transition)[1]. With the polarization gradient cooling mechanism the final temperature scales as I/Δ, with I the cooling beams intensity and Δ their detuning from the cooling optical transition. In our set-up after 2.5 ms from the launch start (i.e. from the introduction of δ) we again change the detuning $\Delta = -3.8\Gamma \to -8\Gamma$ and decrease the beam intensity to $I = 15 I_S \to 6.6 I_S$ for 1.8 ms and then to $I = 6.6 I_S \to 2 I_S$. An RC filter (with $\tau = 500 \, \mu$s) is used to make the intensity changes not too much abrupt in order for the atoms to follow them adiabatically. At the end of the cooling cycle the

---

[1]The Doppler temperature limit is due to the random nature of the spontaneous emission which constitutes the dissipation mechanism in an optical molasses. T_D is calculated by considering the competition between the laser cooling and the diffusion heating introduced with the spontaneous emission.
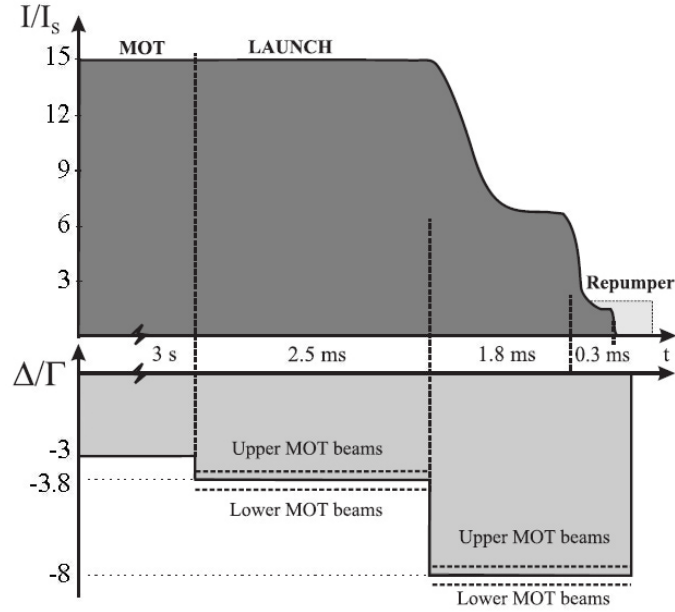
FIGURE 4.2: Trend of the 3D-MOT beams intensity and detuning during the launch sequence. The time axis is not to scale. Figure adapted from [38].

Cooling laser light is completely turned off and only the re-pumping light remains for 3 ms more. With this procedure the atoms are pumped in the $F = 2$ fundamental state with a 99.9 % efficiency and reach a final temperature of $\sim 4\,\mu$K. Fig. 4.2 reports the described launch sequence.

The launched sample can be partially recaptured when it falls back in the trapping chamber by turning on the 3D-MOT again. Indeed, when the sample falls back in the trapping region its velocity is obviously the same as the initial launch velocity (same modulus, opposite direction) which is smaller than the maximum capture velocity of our 3D-MOT ($|v_z| = 4$ m/s $< v_c = 22$ m/s). The main losses for the recapture efficiency are due to the expansion of the cloud during the free fall. With a temperature of 3 μK the thermal velocity is ~ 30 mm/s; this velocity determines an increase of the cloud radius of $\sim$25 mm after a free fall time of 0.8 s (considering a launch velocity of 4 m/s). This radius is larger than the 3D-MOT capture range which is determined by the laser beams dimensions and by the magnetic field gradient.

Launch of multiple samples

The MAGIA-Adv apparatus can be operated as a gradiometer, i.e. an instrument capable of measuring the gradient of the gravitational acceleration. The gradiometric information can be obtained by comparing the signal from two simultaneous gravimeters realized at different known heights. It is therefore necessary to perform two simultaneous interferometers vertically separated by a known distance; this in turn requires to have two atomic samples simultaneously in free fall inside the interferometric tube with the same falling speed (both have to be in resonance with the same interferometric pulses) and with a certain relative distance, which in our set-up is typically ~ 30 cm.

To obtain such a vertical separation the second cloud should be launched from the 3D-MOT within ~ 80 ms after the first one; however this time separation is not

enough to achieve a satisfactory atom number in the second sample. In order to have a good atom number in both the clouds we adopt a different launch strategy called juggling technique [84], [85]:

- A first atom cloud (cloud0) of $\sim 10^9$ atoms is loaded in the 3D-MOT in $\sim$500 ms.

- Cloud0 is launched to a height of $\sim$31 cm for a total flight time of $\sim$500 ms.

- After about 350 ms a second cloud (cloud1) is loaded in the 3D-MOT while cloud0 is still in free flight.

- When cloud0 is nearing the trapping region cloud1 is launched to a height of $\sim$ 91 cm.

- When cloud0 reaches the trapping chamber the 3D-MOT is turned on and the sample is recaptured.

- After $\sim$50 ms cloud0 is launched again to a height of $\sim$ 60 cm.

With this launch sequence[2] we obtain two samples simultaneously in free fall with ^{87}Rb atoms in the ground state with $F = 2$. The next step of the experimental sequence is the state preparation and vertical velocity selection of the samples.

4.2 State preparation and Raman velocity selection

The interferometric interrogation is a single atom process, i.e. any atom in the ensemble will provide an independent interferometric signal; for this reason one would like to have all the atoms in the ensemble contributing with the same phase that adds constructively without any contrast loss. However we note that after the launch:

- Not all the atoms are in the fundamental $F = 2$ state since a residual 0.1 % is in the fundamental $F = 1$ level.

- The atoms populate all the magnetic sub-levels.

- The velocity distribution has a HWHM of about 30 mm/s along each direction.

These characteristics influence the phase contribution of each atom participating in the interferometer and cause loss of contrast. Indeed atoms in different magnetic sub-levels interact differently with the surrounding magnetic fields and atoms with different velocities will experience various Doppler effects and gravitational interactions with the surrounding masses.

Before the interferometer pulse sequence it is therefore necessary to accumulate all the atoms in a preferred internal state and to choose a narrow vertical velocity class. We perform this selection with a series of vertical Raman pulses intertwined with resonant blow-away pulses which remove the unselected atoms. Fig. 4.3 shows the schematic representation of the applied selection procedure.

Before the selection procedure we shine a 10 ms light pulse resonant with the $\nu_{1 \to 0}$ transition. The light beam is divergent and slightly tilted from the vertical

---

[2]The numerical values reported here for the juggling sequence are just an example of a possible implementation. The launch sequence will change sensibly from experiment to experiment as we will see in Ch. 5
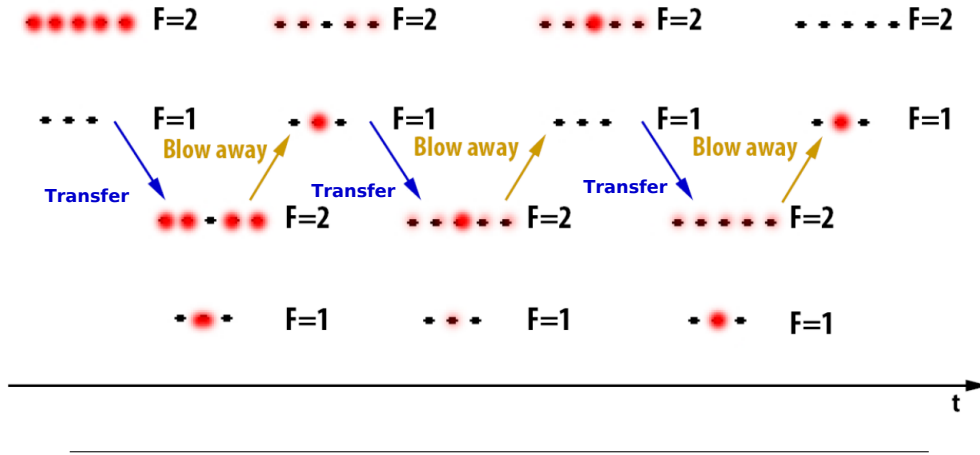
FIGURE 4.3: Triple velocity selection procedure. We show the two hyperfine levels of the fundamental ^{87}Rb state specifying the different magnetic sublevels with the black dots. The atomic population is represented with the red shading. Initially the atoms are uniformly distributed on all the magnetic sublevels of the $F = 2$ fundamental state; at the end of the procedure the atoms are accumulated on the $|F = 1, m_F = 0\rangle$ state. The blue arrows indicate the Raman pulses which transfer the atomic population from $|F = 2, m_F = 0\rangle$ to $|F = 1, m_F = 0\rangle$ and vice versa; the yellow arrows represent pulses of light resonant with the transitions $\nu_{2\rightarrow3}$ or $\nu_{1\rightarrow0}$ used to remove the unselected atoms in $F = 2, 1$.

direction so that it does not get retro-reflected from the mirror on the top of the interferometric tube. This pulse is a first blow-away used to reduce the number of atoms remaining in the $F = 1$ state after the launch by forcing them away.

We then apply a first velocity selective, vertical, Raman π pulse [12] shining on the atoms two counter-propagating Raman beams resonant with the $|F = 2, m_F = 0\rangle \rightarrow |F = 1, m_F = 0\rangle$ transition. The selected velocity class is determined by the Doppler shift of the transition frequency, $\delta_D = \mathbf{p} \cdot \mathbf{k}_L / m = \mathbf{v} \cdot \mathbf{k}_L$, while the velocity spread (i.e. the selectivity of the transition) is related to the frequency width of the Raman transition $\Delta\delta_D$ by the relation

$$\Delta v_z = \frac{\Delta\delta_D}{k_{\text{eff}}}. \tag{4.2}$$

In our case the Raman transition involves two long lived states and ω_{eff} (ω_{eff} is the frequency difference between the Raman lasers) is accurately stabilized. For these reasons the limiting factor for the linewidth comes from the finite interaction time between atoms and Raman light. For example a Raman pulse of duration 200 μs has a Fourier transform with FWHM of 5 kHz, which results in a $\Delta v_z \simeq 2$ mm/s. Considering that the ^{87}Rb recoil velocity is $v_r = 5.9$ mm/s, the atoms after the velocity selection have a velocity distribution with HWHM of $v_r/6$ which corresponds to a temperature $T_r/36 = 10$ nK along the vertical direction. In the transversal directions the velocity distribution maintains a HWHM of about $5v_r$.

After the Raman pulse the unselected atoms which remain in the $F = 2$ state are blown away with a pulse of resonant light with frequency $\nu_{2\rightarrow3}$. The pulse is applied with a divergent vertical beam slightly tilted from the vertical axis to avoid the retro-reflection.

After the $F = 2$ blow away pulse a second Raman π pulse, identical to the first

one, is applied. This time the pulse transfers the atoms back to the $|F = 2, m_F = 0\rangle$ state. The thermal background of unselected atoms in $F = 1$ is removed with the application of a blow-away pulse acting on the $\nu_{1\to 0}$ transition (the same as the one already used before the start of the velocity selection procedure). The sequence is concluded with another Raman π pulse which brings the atoms in the $|F = 1, m_F = 0\rangle$ state and a final $F = 2$ blow-away pulse.

The typical time separation between the Raman pulses is 18 ms and the duration of the blow away pulses is about 5-10 ms.

With this procedure any thermal background on the fluorescence atomic clouds signal is efficiently removed. All the Raman pulses have a square time envelope with equal duration; the frequency difference between the Raman lasers is steered linearly in time to account for the changing Doppler effect of the freely falling atoms (the slope of the linear frequency ramp is ~ 25 MHz/s). The entire procedure usually lasts about 40 ms.

The velocity selection procedure can of course be simplified by reducing the number of applied Raman pulses. However the use of three pulses ensure a complete elimination of the thermal background in the detected atomic signal. The drawback of this procedure lies in the reduced number of atoms participating in the interferometer; however, the obtained larger contrast of the interference fringes compensates the loss of atoms [65].

4.3 Atom interferometer

At the end of the state and velocity selection procedure the atomic sample is finally ready for the interferometric interrogation. The interferometer sequence is composed of three subsequent Raman or Bragg pulses spaced by a time T[3]; the three pulses are arranged in the $\pi/2 - \pi - \pi/2$ Mach-Zehnder configuration. The two interferometric beams enter from the bottom of the vacuum system and traverse all the apparatus until they are retro-reflected at the top of the interferometric tube. To compensate the changing Doppler effect of the freely falling atoms the frequency difference between the beams is linearly swept in time with a phase-continuous frequency ramp from an arbitrary waveform generator. Due to the retro-reflecting mirror, there are two pairs of counter-propagating interferometric beams. However depending on the sign of the applied frequency ramp only one pair is resonant with the atomic frequency in its reference frame. Changing the sign of the ramp thus changes also the direction of the imparted momentum to the atoms $\hbar k_{\text{eff}}$. If an interferometric pulse is applied when the atoms are at rest, i.e. at the apogee of the ballistic trajectory, both beam pairs will satisfy the resonance condition; in this case half of the atoms would exchange the wrong momentum (opposite direction from the one exchanged with the other pulses) and not contribute any more to the interferometer. However if the central π pulse is sent exactly at the apogee the complete MZ interferometer will be spatially symmetric (the two $\pi/2$ pulses will interrogate the atoms in the same vertical position) and systematic effects due to spatially varying fields would be completely compensated. A compromise between these two conditions can be found experimentally by sending the central π pulse when the atoms are close to the apogee, but also far enough so that they have a vertical velocity component sufficient to be in resonance only with one couple of interferometric beams. As we will

---

[3]This is true for the symmetric MZ interferometer that we usually implement; however in Sec. 5.3 we will use a different interferometric geometry based only on two $\pi/2$ pulses.

see in Ch. 5 we will not always respect this condition and perform complete AIs during the ascent of the atomic clouds or during their descent. In particular, when using Bragg diffraction, the interferometer will be performed entirely during the ascent of the atomic sample. This is necessary in order to spatially resolve the two interferometric outputs at the moment of detection. Indeed, since the Bragg diffraction only changes the atomic momentum state, a state selective detection is not possible and the two output ports of the interferometer need free fall time to spatially separate one from the other.

Considering that inside the interferometric tube a bias magnetic field defines the atomic magnetic quantization axis and the Raman beams polarization (lin⊥lin), only Raman transitions with $\Delta m_F = 0$ can be excited.

During the interferometric sequence the moving standing wave formed with the interferometric beams is aligned vertically, parallel to the direction of gravity. However, the Earth rotation during the atomic free fall produces a rotation of the interferometric beam axis with respect to the original direction. Since the atom free-fall trajectory and the interferometric beam axis do not coincide throughout all the interferometer sequence a systematic offset in the phase measurement is present; additionally, the atomic wave packets do not overlap perfectly at the end of the interferometer with a consequent loss of contrast. In our set-up we counteract the effects of Earth's rotation with the use of a tip-tilt mirror [60], [61] as the retro-reflection mirror of the interferometric beams. Applying the proper continuous rotation to the retro-reflection mirror, the momentum transferred to the atoms during the interferometric π and $\pi/2$ pulses, as seen from the atom's inertial reference frame has now a constant direction despite of the Earth's rotation.

Single AI signal

In Sec. 2.2 we derived the phase term induced by the gravitational acceleration g in a MZ interferometer as $\phi = -k_{\text{eff}}gT^2 + \delta\phi^0$. If the measurement is repeated several times with the same experimental conditions the output signal does not change and the interferometric fringe cannot be reconstructed. However we can add a controlled varying phase shift between the Raman lasers ϕ_{ext} in order to scan a complete interferometric fringe (see Fig. 4.4).

In our experimental apparatus the retro-reflecting mirror is not seismically isolated and the interferometric fringes are quickly (i.e. for low T) washed out due to the random phase term introduced by the seismic noise. However this problem can be solved in the gradiometric configuration, i.e. by using two simultaneous interferometers.

Simultaneous AIs signal

For the gradiometer we realize two simultaneous atom interferometers which share the same Raman/Bragg pulses and are vertically separated. The seismic noise is therefore common between the two AIs and can be efficiently suppressed by considering the differential signal.

In this case the two AI output fringes can be written as

$$\begin{cases} x = A\sin(\phi) + x_0, \\ y = C\sin(\phi + \Phi) + y_0, \end{cases} \tag{4.3}$$
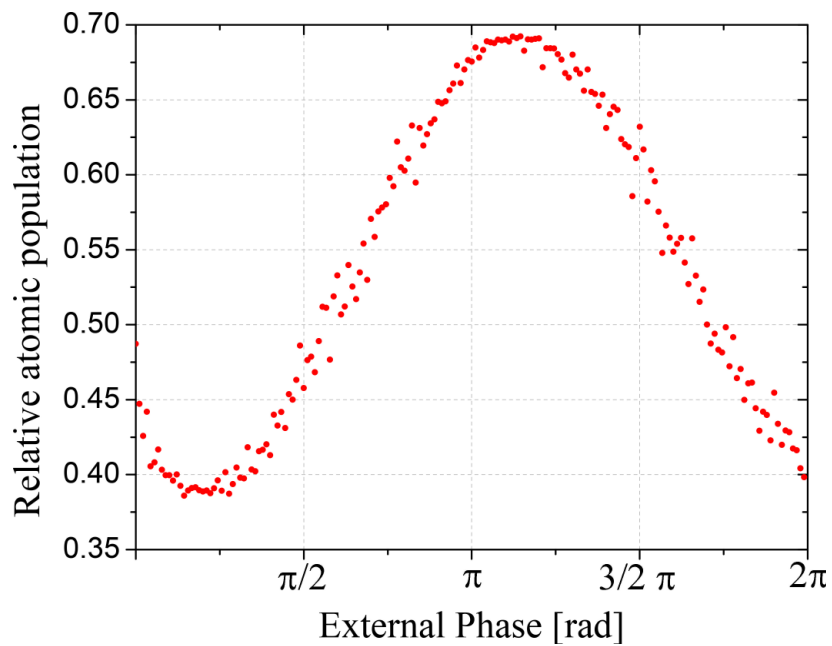
FIGURE 4.4: Normalized interferometric fringe for a Raman interferometer with $T = 1$ ms. The phase is scanned adding a controlled relative phase to the Raman lasers between the π and $\pi/2$ pulse. Each experimental point corresponds to a $2°$ phase change.
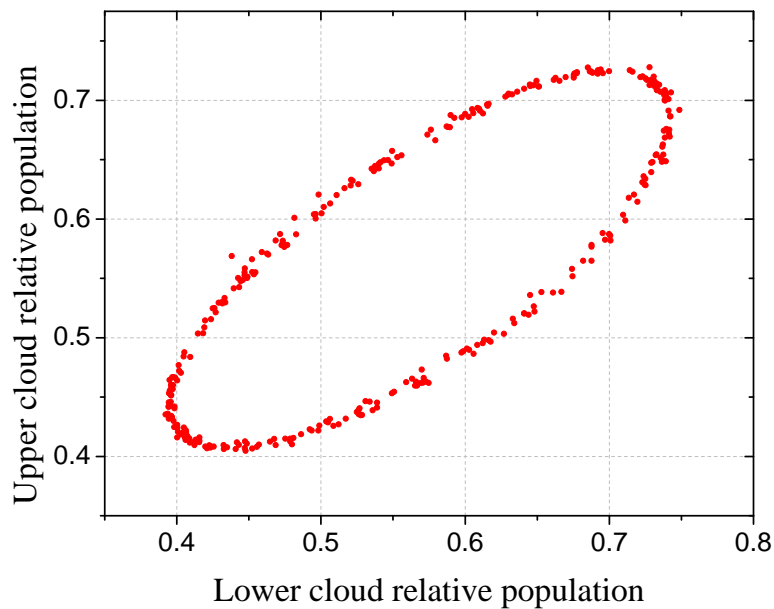

FIGURE 4.5: Gradiometric ellipse for $T = 160$ ms obtained plotting the signal from the upper AI versus the signal of the lower AI. The phase is scanned by the seismic noise on the retro-reflecting mirror.
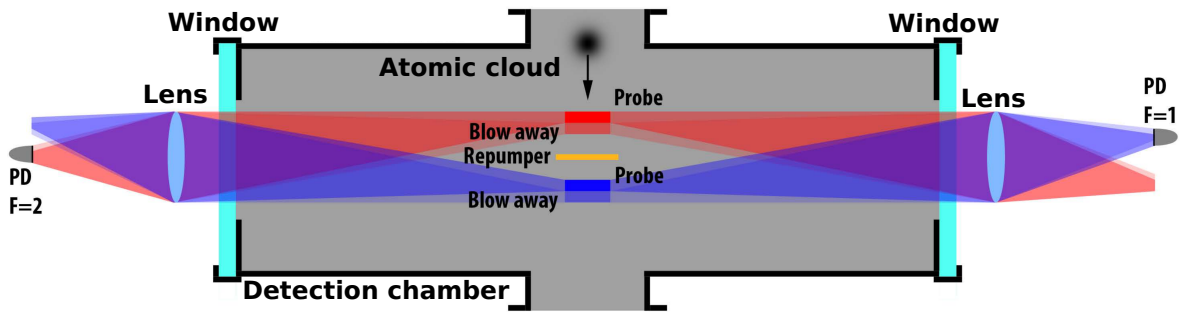
FIGURE 4.6: Side view of the detection chamber with the laser beams used for
the fluorescence detection of the atomic samples. The laser beams propagate
perpendicularly to the page and create three sheets of light which are traversed
by the falling atoms. The fluorescence light is measured with two photodiodes
which provide independent channels for the detection of atoms in the funda-
mental state with $F = 1$ and $F = 2$. The bottom halves of the first and last light
sheets are not retroreflected in order to create a blow away for the atoms which
interacted with the upper part of the beam.

where the term of interest here is the relative phase shift Φ which is due to the verti-
cal separation between the AIs and contains the information about the gravity gra-
dient. Φ can be retrieved fitting the Lissajous figure obtained by plotting the signal
from the upper interferometer versus the signal from the lower interferometer (or
vice versa) with an ellipse (see Fig. 4.5).

We note that in order to scan the interferometric fringes (and in turn scan the
gradiometric ellipse) we do not need to add an external artificial phase like in the
single AI case. Indeed for large T the seismic noise will provide a random phase
contribution $> 2\pi$ which is able to scan complete fringes.

4.4   Detection procedure

At the end of the interferometric sequence the interferometer phase ϕ can be re-
trieved measuring the relative atomic population of the two states involved in the
interferometer. For this purpose our system provides a state selective detection
scheme, i.e. two independent measurement channels for the atomic population in
states $F = 1$ or $F = 2$.

Fig. 4.6 shows a side view of the detection chamber with the basic optical ele-
ments needed for the state selective detection. A first, rectangular shaped (4 mm
$\times$ 15 mm with 3.3 I_S intensity), horizontal light beam with frequency $\nu_{2\to3}$, is used
to detect the atoms in $F = 2$. The upper part of the beam is retro-reflected after
traversing all the length of the detection chamber while the lower portion is not
retro-reflected in order to blow-away the detected atoms in $F = 2$. The fluorescence
light is directed on a photodiode with a $f = 50$ mm lens placed at a distance of 130
mm from the center image.

The atoms in $F = 1$ continue to fall towards the next light sheet (1 mm $\times$ 15, 200
μW/cm^2) with a frequency of $\nu_{1\to2}$. This beam pumps the atoms from $|F = 1\rangle$ to
$|F = 2\rangle$.

Finally the atoms traverse a last light sheet identical to the first one and the flu-
orescence light is collected with an optical system identical to the one already de-
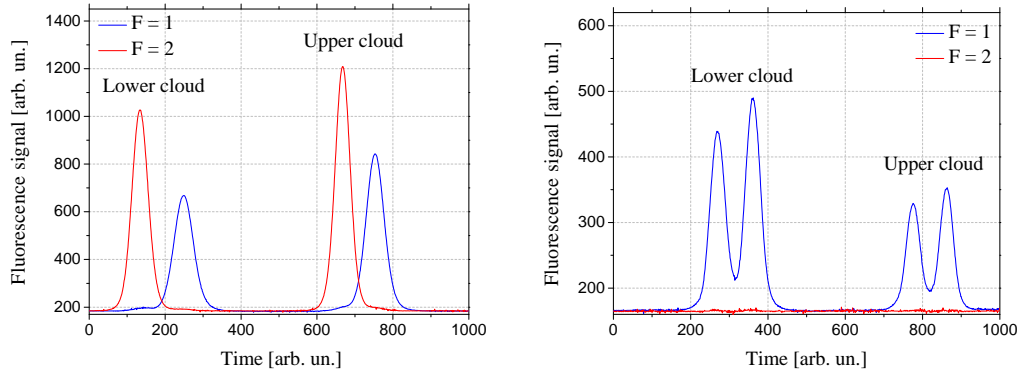scribed.

FIGURE 4.7: (Left) Fuorescence signal for a Raman gradiometer. The two inter-
ferometer output channels differ both in momentum and internal state. (Right)
Fluorescence signal for a Bragg gradiometer. The two peaks are the different
momentum states coupled with the Bragg transition which does not change
the internal atomic state.

In the detection chamber external coils provide a horizontal magnetic field along
the detection beams to define the quantization axis. The magnetic field changes from
vertical, inside the interferometric tube, to horizontal in the detection region in a way
so that atoms can follow the change adiabatically. The detectors are two Hamamatsu
S7510 large area photodiodes (11×6 of active area); the background light is filtered
with a 780 nm interference filter. The photodiode signal is derived from a 1 GΩ tran-
simpedance amplifier realized with an OPA627. The obtained bandwidth is $\sim$kHz
and the noise level was optimized following the scheme described in [86].

Fig. 4.7 shows two examples of the atomic fluorescence signal obtained with the
Raman (left) or the Bragg (right) gradiometer. From the area (A) of the peak we can
extract the atom number (N) in the corresponding state through the relation

$$A = N \frac{\Omega}{4\pi} R_{\mathrm{sc}} \tau \eta_{\mathrm{tot}} h \nu_{2 \to 3}, \tag{4.4}$$

where $h\nu_{2 \to 3}$ is the photon energy, τ is the atom crossing time through the detection
beam, η_{tot} is the photodiode responsivity, Ω the collecting solid angle and R_{sc} the
photon scattering rate. In our experimental conditions the fluorescence spectra show
an atom number of $\sim 10^5$ which translates in a quantum projection noise of $\delta N_q = \sqrt{10^5} \simeq 300$. Considering that the rms noise from the photodiode corresponds to
$\delta N_{\mathrm{ph}} \sim 140 < \delta N_q$, we do not expect to be limited by detection technical noise.

After the detection procedure the sequence is completed and the system ready to
perform another measurement. Each cycle takes about 1.8 s to complete.

In Fig. 4.8 we report a summary of the entire experimental sequence in the case
of the atom gradiometer. With the juggling technique we launch two cold samples
of $\sim 5 \times 10^8$ atoms with a relative vertical displacement of $\sim$30 cm and same free
fall velocity. After the launch, three Raman pulses prepare both the ensembles in
a narrow longitudinal velocity class and in the $|F = 1, m_F = 0\rangle$ state. The three
interferometric pulses are then applied; they interact in the same way with both the
clouds simultaneously (no shadowing effect can be observed due to the low density
of the samples). The fluorescence from the atomic population is finally detected
when the samples fall through the detection chamber; first the lower cloud and then
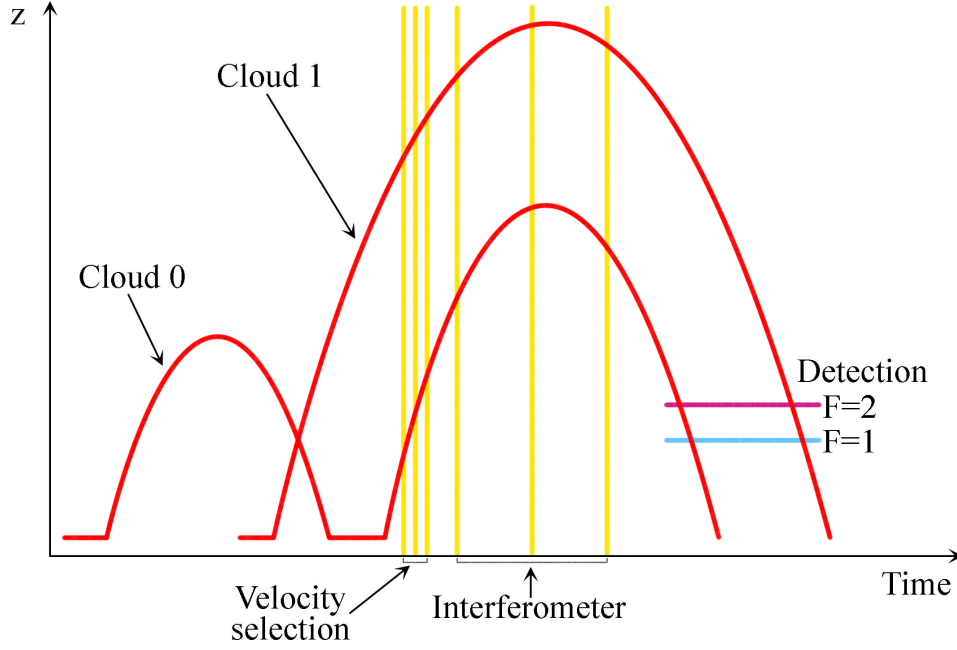the upper one.

FIGURE 4.8: Scheme of the experimental sequence for the gradiometer. The red lines represent the vertical position of the atomic clouds. The three velocity selection and interferometric pulses are represented with the vertical yellow lines while the detection beams are represented with the horizontal lines. Both the axes are not to scale.

4.5   Signal analysis

From Fig. 4.7 we see that in the case of the gradiometer the measured signal consists of two pairs of peaks (one pair for each launched sample) from which we can reconstruct the relative atomic population in the two states involved in the interferometer. To retrieve the amplitude of the peaks we fit the signal with Gaussian functions and a background linear slope. From the fit we obtain the area of each peak A_F^z which is a measure of the number of atoms in the corresponding state. Since the total atom number fluctuates from one experimental shot to next we are interested in the relative atomic number in each state which for a Raman interferometer can be written as

$$n_1^{\text{up}} = \frac{S_1^{\text{up}}}{S_1^{\text{up}} + S_2^{\text{up}}} \qquad n_2^{\text{up}} = \frac{S_2^{\text{up}}}{S_1^{\text{up}} + S_2^{\text{up}}},$$
$$n_1^{\text{dw}} = \frac{S_1^{\text{dw}}}{S_1^{\text{dw}} + S_2^{\text{dw}}} \qquad n_2^{\text{dw}} = \frac{S_2^{\text{dw}}}{S_1^{\text{dw}} + S_2^{\text{dw}}}. \tag{4.5}$$

A gradiometric ellipse can therefore be obtained plotting the normalized atom number from the upper cloud signal versus the one from the lower cloud, e.g. n_1^{up} VS n_1^{dw}.

As already mentioned (see Eq. 4.3) in a gradiometer the signal of interest is the relative de-phasing Φ accumulated between the two simultaneous AIs. If the phase noise is low and the single interferometer fringes maintain a high visibility the relative phase shift could be extracted directly from a sinusoidal fit of the single interferometer signals. In this case the fringes need to be artificially scanned by varying the relative phase between the interferometric lasers.

For the typical interrogation times T employed this approach cannot be applied without any seismical isolation of the retro-reflecting mirror or some post-correction process of the interferometer signal. Indeed, since any mechanical vibration of the retro-reflecting mirror is converted to phase noise, the fringes will be rapidly deteriorated for increasing interrogation times T (the MZ interferometer sensitivity to accelerations scales quadratically with T).

This effect is rejected adopting a differential measurement configuration. With this strategy any common mode noise, affecting both the simultaneous interferometers in the same way (e.g. the seismical noise) is efficiently rejected. With a differential measurement what is detected is basically the acceleration of a sample with respect to the other one and the samples are vibration free due to their free fall in vacuum.

We already mentioned that from the Lissajous figure obtained plotting the signal of the upper cloud versus the one of the lower cloud, we can extract the relative phase Φ with an elliptical fit [87]. We now rewrite the expression for the two interferometric fringes in a gradiometer

$$\begin{cases} x = A\sin(\phi) + x_0, \\ y = C\sin(\phi + \Phi) + y_0. \end{cases} \tag{4.6}$$

The fringes can be described with two independent amplitudes (A and B) and two independent vertical offsets (x_0 and y_0) and a the relative phase shift Φ which is the quantity of interest that we want to determine. The offsets can be removed with a translation

$$\begin{cases} x' = A\sin(\phi), \\ y' = C\sin(\phi + \Phi), \end{cases}$$

and the above equations can be reorganized to obtain the equation of an ellipse

$$\frac{x'^2}{A^2} + \frac{y'^2}{C^2} - x'y'\left(\frac{2\cos\Phi}{AC}\right) - \sin^2\Phi = 0. \tag{4.7}$$

We rotate the reference system by the angle $\alpha \to \tan\alpha = 2AC\cos\Phi/(C^2 - A^2)$, in order to eliminate the term in $x'y'$. The new coordinates will be

$$\begin{cases} x'' = x'\cos\alpha + y'\sin\alpha \\ y'' = -x'\sin\alpha + y'\cos\alpha, \end{cases}$$

and the ellipse equation becomes the canonical expression

$$\frac{x''^2}{a^2} + \frac{y''^2}{b^2} - 1 = 0, \tag{4.8}$$

where

$$\begin{cases} a^2 = \frac{2A^2C^2\sin^2\Phi}{A^2+C^2+\sqrt{A^4+C^4+2A^2C^2\cos 2\Phi}} \\ b^2 = \frac{2A^2C^2\sin^2\Phi}{A^2+C^2-\sqrt{A^4+C^4+2A^2C^2\cos 2\Phi}}. \end{cases}$$

If we consider a set of n experimental points (x_i, y_i) with experimental errors $(\sigma_{xi}, \sigma_{yi})$ the best fitting curve can be found by calculating the n mathematical points

$(\bar{x}_i, \bar{y}_i)$ which minimize the χ^2

$$\chi^2 = \sum_{i=1}^{n} \frac{(x_i - \bar{x}_i)^2}{\sigma_{xi}^2} + \frac{(y_i - \bar{y}_i)^2}{\sigma_{yi}^2}, \tag{4.9}$$

with the condition that they belong to a curve $f(x,y) = 0$ with p parameters to be determined. With the method of the Lagrange multipliers we thus obtain a system of $3n + p$ variables, n from $\bar{x}_i$, $\bar{y}_i$ and the Lagrange multipliers λ_i and p from the curve parameters α_p which are the parameters of interest to be determined. Assuming $\sigma_{xi} = \sigma_{yi}$ the problem can be simplified from a least χ^2 method to a least squares method which is solved minimizing

$$S = \sum_{i=1}^{n} (x_i - \bar{x}_i)^2 + (y_i - \bar{y}_i)^2 - \lambda_i f(\bar{x}_i, \bar{y}_i). \tag{4.10}$$

The differential equation system to be solved is then

$$\begin{cases} \frac{\partial S}{\partial \bar{x}_i} = -2(x_i - \bar{x}_i) - \lambda_i \frac{\partial f}{\partial \bar{x}_i} = 0 \\[2ex] \frac{\partial S}{\partial \bar{y}_i} = -2(y_i - \bar{y}_i) - \lambda_i \frac{\partial f}{\partial \bar{y}_i} = 0 \\[2ex] \frac{\partial S}{\partial \lambda_i} = f(\bar{x}_i, \bar{y}_i) = 0 \\[2ex] \frac{\partial S}{\partial \alpha_p} = \sum_{i=1}^{n} \frac{\partial f(\bar{x}_i, \bar{y}_i)}{\partial \alpha_p} = 0. \end{cases}$$

This system can be treated numerically. We adopt the following algorithm:

- A numerical minimization software (our fitting software uses MINUIT libraries [88]) works on the parameters A, x_0, C, y_0 and Φ.

- The minimizer receives initial values for the five parameters. Since our experimental points are usually uniformly distributed along the entire ellipse we can average over the phase angle ϕ

$$\begin{cases} \frac{1}{n} \sum_{i=1}^{n} x_i \simeq \frac{1}{2\pi} \int_0^{2\pi} x(\theta) d\theta = x_0 \\[2ex] \frac{1}{n} \sum_{i=1}^{n} x_i^2 \simeq \frac{A^2}{2} \\[2ex] \frac{1}{n} \sum_{i=1}^{n} y_i \simeq y_0 \\[2ex] \frac{1}{n} \sum_{i=1}^{n} y_i^2 \simeq \frac{C^2}{2} \\[2ex] \frac{1}{n} \sum_{i=1}^{n} x_i y_i \simeq \frac{AC \cos \Phi}{2} \end{cases}$$

  The minimizer is therefore initialized with the set of parameters $[A, x_0, C, y_0, \Phi]_j$.

- The experimental points (x_i, y_i) are translated and rotated in order to transform the initial ellipse to the canonical form (see Eq.4.8). The parameters a and b are calculated and S_j is determined. The calculation of S is reduced to n systems of 3 equations with 3 variables which basically consists in calculating the
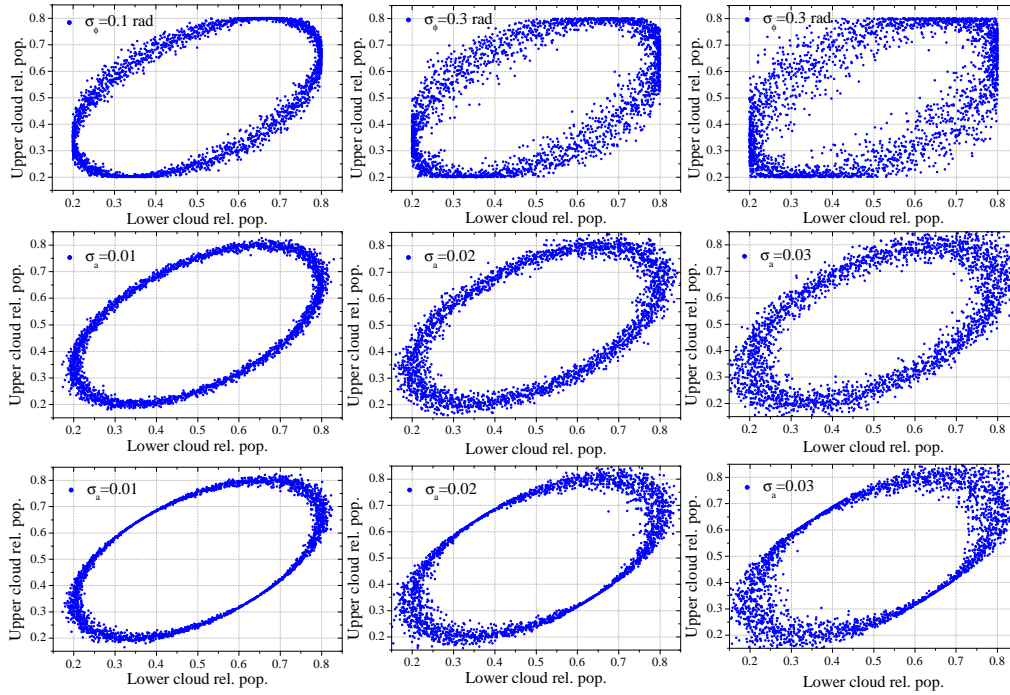
FIGURE 4.9: Simulations of gradiometric ellipses affected by different noise levels on the phase angle Φ (top set of ellipses), the amplitude (middle set of ellipses) and on the offsets (bottom set of ellipses). For the simulation we set A = B = 0.5, $x_0 = y_0 = 0.5$ and $\Phi = 1$ rad. The noise is Gaussian with $\sigma_\phi = 0.1$ rad (left), 0.2 rad (middle) and 0.3 rad (right) for the phase and $\sigma_a = \sigma_\phi = 0.01$ (left), 0.02 (middle) and 0.03 (right) for the amplitude and offset.

geometric distance of the experimental point from the mathematical model

$$
\begin{cases}
(x_i - \bar{x}_i) = \frac{\lambda_i \bar{x}_i}{a^2} \\[2mm]
(y_i - \bar{y}_i) = \frac{\lambda_i \bar{y}_i}{b^2} \\[2mm]
\frac{\bar{x}_1^2}{a^2} + \frac{\bar{y}_1^2}{b^2} - 1 = 0
\end{cases}
$$

The sum of the squares of the distances for all the experimental points (x_i, y_i) is S_j.

- The minimizer is used to derive the minimum value of the multi-parameter function S_j. A new set of parameters is produced $[A, x_0, C, y_0, \Phi]_{j+1}$ and the procedure is repeated until S is minimized.

- The parameter Φ is then determined.

Noise sensitivity

The gradiometric ellipse signal can be affected by three kinds of noise

$$
\text{Phase noise} \quad
\begin{cases}
x = A\sin(\phi), \\
y = C\sin(\phi + \Phi + \sigma_\Phi) + y_0.
\end{cases}
$$

Amplitude noise $\quad\begin{cases} x = (A + \sigma_a)\sin(\phi) + x_0, \\ y = (C + \sigma_a)\sin(\phi + \Phi) + y_0. \end{cases}$

Offset noise $\quad\begin{cases} x = A\sin(\phi) + x_0 + \sigma_0, \\ y = C\sin(\phi + \Phi) + y_0 + \sigma_0. \end{cases}$

In order to understand the effect of these different noise contributions on the gradiometric ellipse signal we simulated the experimental data for three values of the phase noise σ_ϕ, the amplitude noise σ_a and the offset noise σ_0. We report the result of these simulations in Fig. 4.9. We note that the different kinds of noise produce ellipses with different characteristics. The phase noise for example can derive from fluctuations in spurious electromagnetic fields and it is amplified between the minima and maxima of the single interferometer fringe signal. On the contrary, the amplitude noise, which can derive from variations of the two-photon Rabi frequency is amplified at the maxima and minima of the fringe signals. The offset noise moves the ellipse around the x-y plane and can be caused by instabilities in the frequency of the re-pumper light.

A more thorough analysis of the noise contributions can be found in [38], [65], together with comparisons between simulated and real experimental data points. The results of the analysis show that the dominant noise is the amplitude noise. Furthermore the bias in the measured value of Φ due to the noise is minimum when $\Phi \simeq \pi/2$. Whenever possible it is thus convenient to add a controlled relative phase shift which brings the differential phase Φ close to $\pi/2$ (more informations on this in [38], [65]).

Chapter 5

Experimental results

In this chapter we present the measurements performed in the last three years with the MAGIA-Adv apparatus. The chapter is divided in four sections.

The first one is dedicated to the characterization measurements realized with the Bragg atom gradiometer. These measurements are important since Bragg transitions were never being implemented in the MAGIA-Adv apparatus before and allowed us to set the best experimental conditions for the successive measurements with the Bragg interferometer.

In the second section we present the results obtained for a test of the Weak Equivalence Principle in the classical and quantum regime. For these measurements we used the previously characterized Bragg gradiometer.

In the third section we demonstrate a new experimental method to perform a gravimetric measurement through matter-wave velocimetry. These measurements were realized with the Raman interferometer and with a different interferometric geometry than the usual MZ configuration; we used two subsequent Ramsey interferometers to measure the velocity variation of freely falling cold atom samples, thus determining the experienced gravitational acceleration. We also compare the obtained sensitivity with the one of a standard MZ interferometer and the one of a Ramsey-Bordé interferometer.

Finally, in the fourth section we report the experimental demonstration of a novel method to compensate the effects introduced by gravity gradients in a MZ atom interferometer. Using the Raman interferometer we apply this technique to provide a measurement of the local gravity gradient and the gravity field curvature.

Since the main experimental apparatus and experimental procedure have already been described in the previous chapters, here we will only describe the changes that we needed to introduce for each of the presented measurements without going into all the details of the apparatus and sequence.

5.1 Characterization of the Bragg gradiometer

In this first section we report the characterization measurements realized with the Bragg interferometer [89]. These measurements are focused on finding the most convenient experimental conditions for the Bragg gradiometer. In the following we will always consider 3rd order Bragg transitions.

The laser system dedicated to the production of the Bragg pulses has been described in Sec. 3.3.6. We note that in order to have the right beam polarizations for the Bragg diffraction we added a $\lambda/4$ wave-plate at the bottom of the vacuum system. The polarization of the Bragg beams is therefore modified into circular $\sigma^+ - \sigma^-$.

5.1.1 Optimization of gradiometric contrast

Using the Bragg gradiometer, with two atomic samples vertically separated by 30 cm, we analysed the dependence of the contrast for the upper and lower interferometer versus different experimental parameters. The contrast for the upper and lower interferometer can be derived from the normalized atomic population interval explored by the gradiometric ellipse along the vertical and horizontal axes respectively.

For the excitation of the Bragg transitions we initially use Gaussian pulses with $\sigma = 24$ μs. We launch two atomic samples with the juggling procedure and select a narrow vertical velocity class in the $|F = 1, m_F = 0\rangle$ state with the three velocity selection pulses. We then apply three subsequent 3$^{\text{rd}}$ order Bragg pulses and obtain two simultaneous MZ interferometers vertically displaced of about 30 cm.

In the first characterization we varied the free evolution time T between the successive MZ interferometric pulses. The results are reported in Fig. 5.1 (top). We note that the upper cloud interferometer tends to lose contrast faster than the lower one. This behaviour is due to the 80 ms longer expansion time that the upper atomic sample has to experience before the interferometric interrogation. Furthermore, due to the juggling launch procedure the upper sample is usually hotter (in terms of the transversal temperature) than the lower one. This is due to the heating induced by the light scattered from the lower atomic cloud when it is loaded in the 3D-MOT.

As mentioned in Sec. 4.3, the Bragg interferometer needs to be realized completely during the ascent of the atomic clouds for the two interferometric output ports to be spatially resolved at the moment of detection. This requirement ultimately limits the achievable interrogation time T.

We then set the free evolution time to $T = 40$ ms and analysed the behaviour of the interferometric contrast for different velocity selection pulse lengths. The longitudinal velocity selection is described in detail in Sec. 4.2, we recall here that it is realized before the interferometer with three square Raman pulses of duration T_{sel}. The results for this characterization are reported in Fig. 5.1 (middle). We note a slight increase in contrast when the velocity selection pulses become longer. We attribute this improvement to the narrower vertical velocity distribution obtained with longer selection pulses. Despite the contrast increase in the next measurements we chose to work with selection pulses of $T_{\text{sel}} = 192$ μs. Increasing further T_{sel} would indeed produce just a slight increase in the contrast at the expense of major losses in terms of detected atoms without any improvement at the signal to noise ratio.

For the last contrast characterization we varied the interferometric pulse width σ. Each time σ is changed the pulse peak power as to be adjusted accordingly in order to maintain efficient π and $\pi/2$ pulses. The contrast behaviours obtained with these measurements are reported in Fig 5.1 (bottom). We note a pronounced contrast increase for shorter Bragg pulses which convinced us to use Gaussian pulses with $\sigma = 12$ μs for the successive measurements. Furthermore, our present laser system cannot deliver enough optical power for shorter pulses.

The contrast improvement obtained with the shorter Bragg pulses was enough to allow us to increase the interrogation time from 40 ms to 80 ms thus increasing the overall instrument sensitivity to inertial effects of a factor 4.

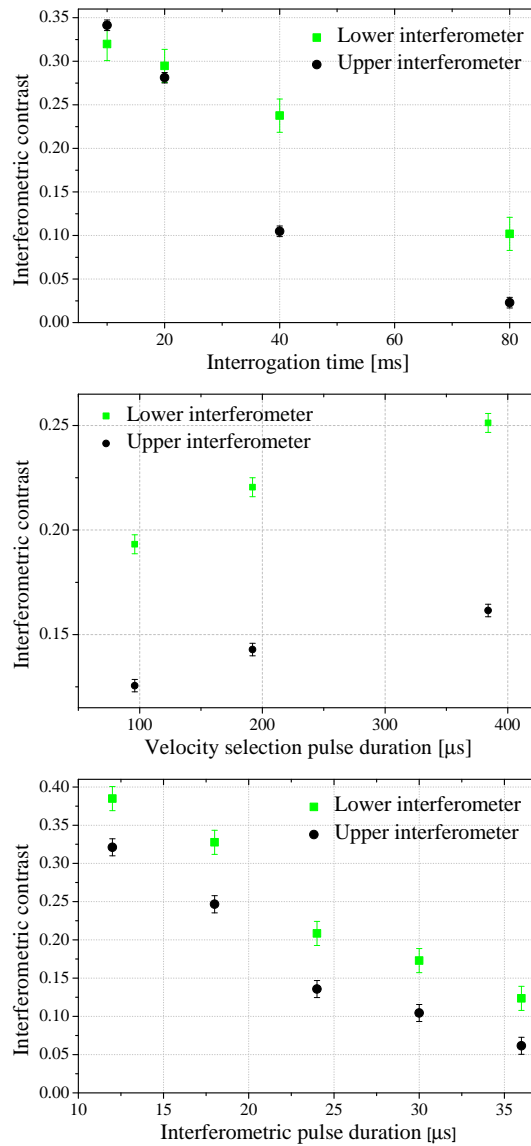Fig. 5.2 (left) reports an example of the gradiometric ellipses acquired in these experimental conditions.

FIGURE 5.1: (Top)Contrast of the lower and upper interferometer versus the free evolution time between the Bragg diffraction pulses of the MZ interferometer. (Middle) Contrast of the lower and upper interferometer in function of the velocity selection pulse length T_{sel}. (Bottom) Contrast of the lower and upper interferometers versus the interferometric pulse width.
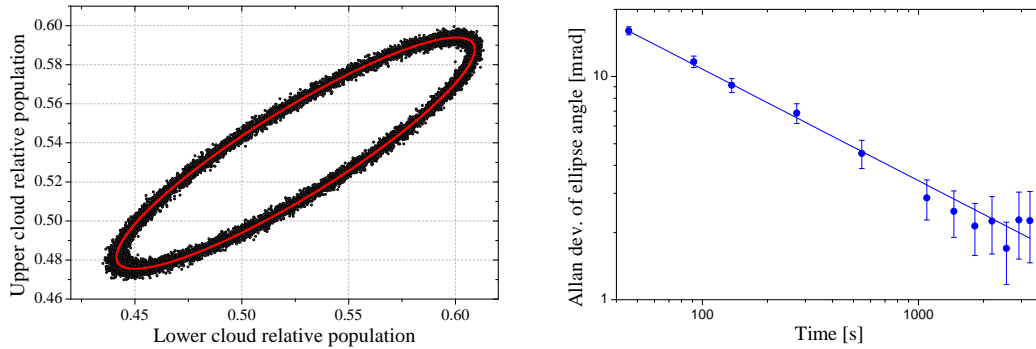
FIGURE 5.2: Stability analysis of the Bragg gradiometer. (Left)Gradiometric ellipse acquired with an interrogation time $T = 80$ ms and an interferometric pulse width of $\sigma = 12$ μs. An elliptical least squares fit of the data is shown with the red line. (Right) Allan deviation of the gradiometric phase angle. The blue line is a fit of the experimental data with the function $\sigma_\Phi = a/\sqrt{t}$, with t the integration time.

5.1.2   Allan deviation of phase angle

To evaluate the phase stability and the sensitivity of our set-up we extracted the Allan deviation of the gradiometric phase angle using the data points shown in Fig. 5.2 (left) which are obtained in a measurement run of about 8 h.

The corresponding Allan deviation, reported in the right panel of Fig.5.2, shows the characteristic dependence as $1/\sqrt{t}$ (with t the integration time). We can conclude that the gradiometer is mainly affected by white phase noise. We exclude the presence of a flicker floor only up to 1000 s of integration time due to the large error bars at long times t. From a fit (blue line in the figure) of the experimental Allan deviation we can derive the short and long term sensitivity of the gradiometer. Considering that the interferometer vertical separation is of 30 cm, at 1 s of integration time the sensitivity to gravity gradients is 1.2×10^{-6} s^{-2} which translates to a sensitivity for differential accelerations of $3.6 \times 10^{-8}g$. After 2000 s of integration time the sensitivity to gravity gradients reduces to 2.6×10^{-8} s^{-2} which corresponds to $8.0 \times 10^{-10}g$ of differential acceleration sensitivity.

5.1.3   Phase angle dependence on magnetic quantization field

We now analyse the dependence of the gradiometric phase angle from the magnetic quantization field produced inside the interferometric tube.

For the next measurements we apply the k-reversal procedure [90]. This technique permits to reject all the systematic effects that depend on even powers of k_{eff}. Indeed the gradiometric signal can be decomposed in two contributions: a part that depends on odd powers of k_{eff} which we call Φ_{odd} (e.g. the signal from the gravity gradient itself and the signal from residual Coriolis acceleration) and a part which depends on even k_{eff} powers which we label as Φ_{even} (e.g. the one due to single photon light shifts); the total gradiometric phase angle will result from the sum of these two contributions $\Phi = \Phi_{\text{odd}} + \Phi_{\text{even}}$. The k-reversal procedure consists in reversing the direction of the imparted momentum k_{eff} for each experimental cycle; we thus obtain two different gradiometric phase angles $\Phi_{\text{dir}} = \Phi_{\text{odd}} + \Phi_{\text{even}}$ and $\Phi_{\text{rev}} = -\Phi_{\text{odd}} + \Phi_{\text{even}}$ which differ for the sign of the phase term which depends on

odd powers of k_{eff}; therefore the combination

$$\Phi_{\text{odd}} = \frac{\Phi_{\text{dir}} - \Phi_{\text{rev}}}{2},\tag{5.1}$$

permits to reject all the systematics effects which depend on even powers of k_{eff}.

Let us now consider the effect of magnetic fields on the gradiometric signal. Inside the interferometric tube we can model the magnetic field as the sum of a bias term B_0 and a magnetic field gradient term B', i.e.

$$B(x) = B_0 + B'(x),\tag{5.2}$$

The two contributions take into account the effect of the solenoid wrapped around the tube, which we can control by changing the current flowing in the coil and any other spurious source which is not completely rejected by the magnetic shielding. We can therefore decompose them as the sum $B_0 = B_{\text{sol}} + B_{\text{res}}$ and $B' = B'_{\text{sol}} + B'_{\text{res}}$, where we have distinguished the contribution of the solenoid from the contribution of the residual fields.

The effect of a magnetic field on the interferometer signal can be calculated considering the Lagrangian for the second order Zeeman effect

$$\mathcal{L}(x, \dot{x}) = 2\pi\hbar\beta B^2(x),\tag{5.3}$$

where $\beta = 28.8\,\text{GHz/T}^2$. Substituting the expression for the magnetic field in Eq. 5.2 we obtain

$$\mathcal{L}(x, \dot{x}) = 2\pi\hbar\beta(B_0^2 + 2B_0B'x + B'^2x^2) = K + ma_Bx + m\frac{\gamma_B}{2}x^2,\tag{5.4}$$

with m the ^{87}Rb mass, $a_B = 4\pi\hbar\beta B_0 B'/m$ and $\gamma_B = 4\pi\hbar\beta B'^2/m$.

The above Lagrangian is equivalent to that produced in presence of a uniform gravitational acceleration a_B plus a linear gravity gradient γ_B. The corresponding single interferometer phase shift can then be written as [15], [59]

$$\phi^B = k_{\text{eff}}\left[a_BT^2 + \gamma_BT^2\left(-\frac{7}{12}a_BT^2 + v_0T + z_0\right) + O(\gamma_B^2)\right],\tag{5.5}$$

and it will not be rejected with the k-reversal procedure. If we now consider the gradiometric configuration and label with u and l the magnetic bias field and magnetic field gradient experienced by the upper and lower atom interferometers we can write their effect on the gradiometric phase angle as

$$\Phi^B = \alpha[B_0^u B'^u - B_0^l B'^l],\tag{5.6}$$

with $\alpha = 4\pi\hbar k_{\text{eff}}\beta T^2/m \simeq 82 \times 10^6\,\text{rad m/T}^2$.

The effect of the magnetic field will appear in the term Φ_{odd} of the total gradiometric phase angle and since Φ^B takes into account both the field generated by the solenoid and any residual magnetic field we can expect a quadratic dependence of Φ_{odd} on the solenoid current, i.e. $\Phi_{\text{odd}} = \Phi_{I^2} + \Phi_I + A$. The I^2 term derives from the product of B_{sol} and B'_{sol}, the I term contains the mixed products $B_{\text{sol}}B'_{\text{res}}$ and $B_{\text{res}}B'_{\text{sol}}$, while the last term takes into account the contributions of B_{res} and B'_{res}.

We acquired gradiometric phase angles for different values of the current injected in the solenoid, I. The corresponding results are reported in Fig. 5.3 together with a second order polynomial fit of the experimental data $\Phi_{\text{odd}} = aI^2 + bI + A$.
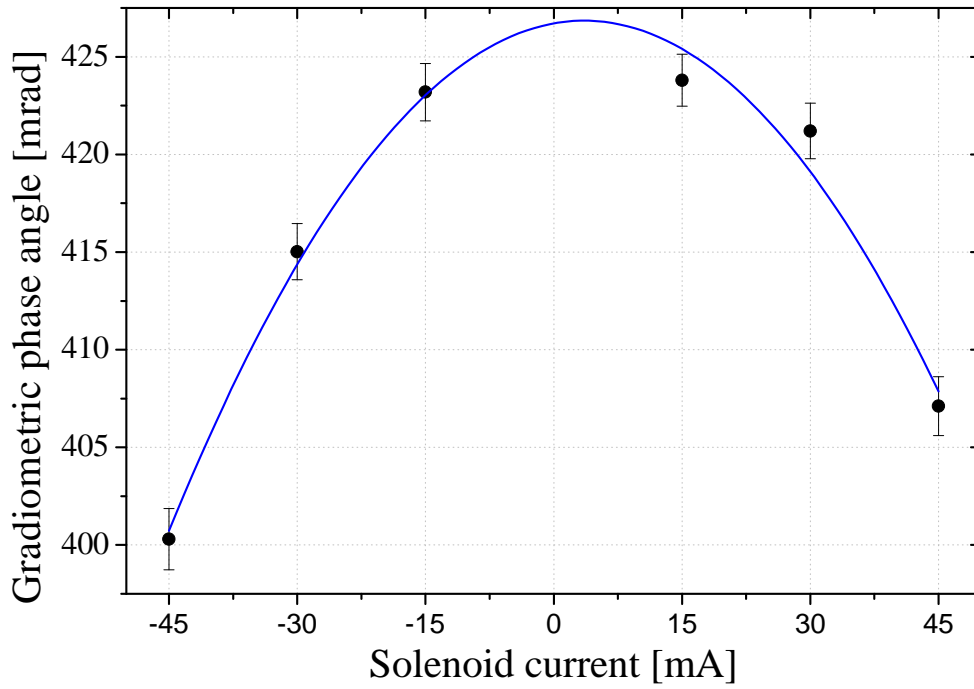
FIGURE 5.3: Gradiometric phase angle dependence on the current injected in the bias solenoid wrapped around the interferometric region. The blue line is a second order polynomial fit of the data.

Since in our apparatus $B_{\text{sol}} = 1.1\ \mu\text{T/mA}$, from the fit results we can estimate $B'_{\text{sol}} = |a|/(\alpha B_{\text{sol}}) = 0.1\ \mu\text{T/(m mA)}$. At this point we can derive an upper limit for the residual magnetic gradient and the residual magnetic field as

$$
\begin{aligned}
B'_{\text{res}} &< \frac{b}{\alpha B_{\text{sol}}} = 0.88\ \mu\text{T/m,} \\
B_{\text{res}} &< \frac{b}{\alpha B'_{\text{sol}}} = 7.9\ \mu\text{T.}
\end{aligned}
\tag{5.7}
$$

From these two results we can establish an upper limit for the systematic shift introduced by the residual magnetic fields as

$$
\Phi^B_{\text{res}} < \alpha B_{\text{res}} B'_{\text{res}} \simeq (0.6 \pm 0.4)\text{mrad.}
\tag{5.8}
$$

We expect that the major fraction of this systematic shift comes from the lower atomic sample of the gradiometer; this is because the lower sample is the one nearer the interferometric tube entrance, i.e. where the magnetic shielding is less effective.

5.1.4 Phase angle dependence on Bragg beams detuning

The standard working condition for our Bragg lasers is with a blue detuning of 3.269 GHz from the Reference laser. We acquired gradiometric ellipses varying this detuning in steps of 50 MHz around its nominal value. A variation in the detuning can affect the amount of atom losses via spontaneous emission, however since this mechanism affects both the simultaneous interferometers in the same way we expect
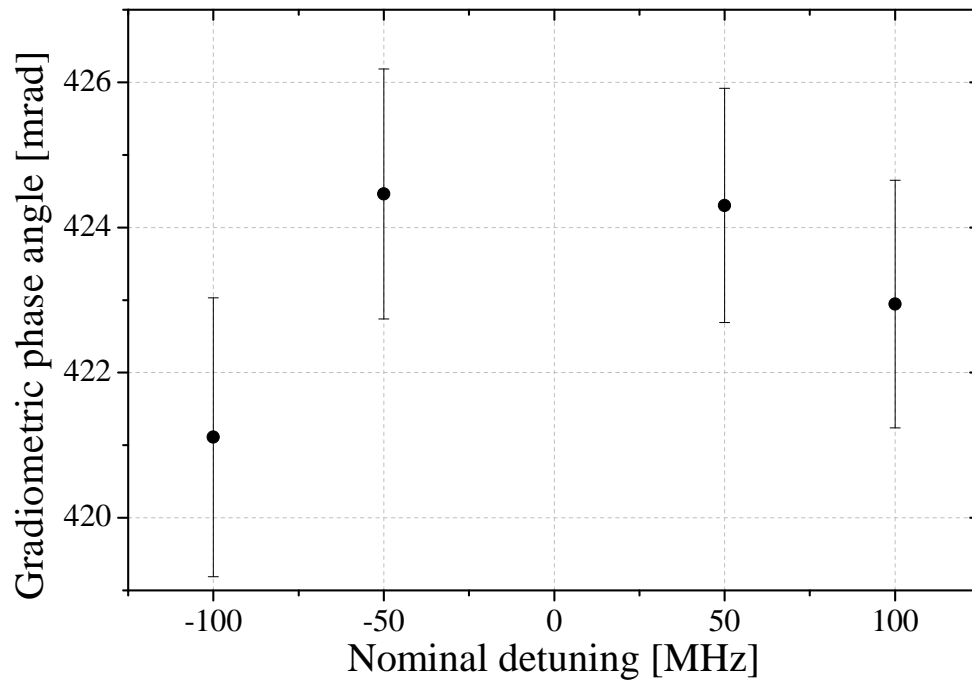
FIGURE 5.4: Dependence of the gradiometric phase angle as a function of the detuning of the Bragg beams.

a strong rejection of any related systematic shift. We report the experimental gradiometric phase angles in Fig. 5.4; the results are all compatible within our experimental errors; we therefore cannot detect any effect of the detuning at this level.

5.2   Test of the Weak Equivalence Principle in classical and quantum regimes

The characterization measurements presented in the previous section allowed us to set the experimental conditions used in our Bragg gradiometer for the realization of a test of the Weak Equivalence Principle (WEP).

Since a Bragg transition does not change the internal atomic state, but only acts on the momentum degrees of freedom of the atoms, the Bragg gradiometer could be used to perform a test of the WEP between ^{87}Rb atoms in different internal states; in particular the test involved ^{87}Rb atoms with a defined spin orientation and in a superposition state of two orthogonal spins. This last configuration allowed us to test genuinely quantum features of the WEP, remained so far unexplored [25].

5.2.1   Theoretical overview

There have been lots of theoretical and experimental efforts in the attempt to detect WEP violations. Usually in these experiments the free fall accelerations of different test bodies A and B are compared. A measure of the WEP violation is then provided by the so called Eötvös ratio $\eta_{\text{A-B}}$ which is defined starting from the measured differential acceleration as

$$\eta_{\text{A-B}} = 2\frac{|a_A - a_B|}{|a_A + a_B|} = 2\frac{|(m_i/m_g)_A - (m_i/m_g)_B|}{|(m_i/m_g)_A + (m_i/m_g)_B|}. \tag{5.9}$$

with m_i and m_g the inertial and gravitational mass respectively.

Today the most stringent bounds on the Eötvös ratio are provided by macroscopic experiments; in particular torsion balance [91] or Lunar Laser Ranging tests [92] which reach accuracy levels of 10^{-13}. Experiments with atom interferometers are flourishing even though they are still limited to accuracies in the $10^{-7} - 10^{-8}$ range, but are expected to improve their sensitivity by several orders of magnitude in the near future.

The Einstein Equivalence Principle (EEP) states the equivalence between three different mass-energies of a body: the rest mass-energy, the inertial mass-energy and the mass-energy that constitutes the weight of the body. Testing the EEP in classical physics requires to compare the values of these three mass-energies treating them as classical variables. In quantum mechanics this is not enough any more. Indeed, in this case, the internal energy is given by a Hamiltonian operator which takes into account the dynamics of internal degrees of freedom which finally contribute to the total mass-energy. Furthermore a general state of the internal energy can involve superposition of states with different eigenvalues of the internal energy. A quantum formulation of the EEP that states the equivalence between the rest, inertial and gravitational mass-energy quantum operators is therefore necessary. In particular the WEP requires the equivalence of only the inertial and gravitational mass-energy operators.

We note that the so far realized experimental tests of the WEP (including the tests with AIs) can all be considered as classical tests, i.e. experiments sensitive only to the diagonal elements of the mass-energy inertial and gravitational operators. The validity of the EEP in the quantum regime can be probed only with experiments which can access the off-diagonal elements of the mass-energy quantum operators. This characteristic necessarily requires the use of superposition states. In our experiment we therefore compare the free fall acceleration of ^{87}Rb atoms when they are prepared

in the two ground hyperfine energy levels $|1\rangle = |F = 1, m_f = 0\rangle$, $|2\rangle = |F = 2, m_f = 0\rangle$ or in their coherent superposition $|s\rangle = (|1\rangle + e^{i\gamma}|2\rangle)/\sqrt{2}$. The phase γ is a random phase with standard deviation $\gg 2\pi$ which cannot be controlled from one experimental cycle to the next and derives from the preparation process of the superposition state with a microwave pulse.

The mass-energy operators can be defined starting from the mass-energy equivalence as

$$\hat{M}_\alpha = m_\alpha \hat{I} + \frac{\hat{H}_\alpha}{c^2}, \tag{5.10}$$

where $\alpha = \text{i, g}$. The operators $\hat{H}_i$ and $\hat{H}_g$ are the contributions of the internal energy to the inertial and gravitational mass respectively. With this definition, the WEP principle requires $\hat{M}_i = \hat{M}_g$.

If we consider a test theory which allows violations of the quantum WEP then $\hat{M}_i \neq \hat{M}_g$ and the free fall acceleration of the centre-of-motion can be written as $\hat{a} = \hat{M}_g \hat{M}_i^{-1} g$, with g the local gravitational field. We note that the quantum formulation of the WEP in general requires $[\hat{M}_g, \hat{M}_i] \neq 0$, while the case $[\hat{M}_g, \hat{M}_i] = 0$ is equivalent to the classical WEP formulation. This means that the operator $\hat{M}_g \hat{M}_i^{-1}$ is not Hermitian; however, to lowest order in $1/c^2$ it can be approximated as a Hermitian operator which matrix form in the basis spanned by $|1\rangle$ and $|2\rangle$ is

$$\hat{M}_g \hat{M}_i^{-1} \simeq \begin{pmatrix} r_1 & r \\ r^* & r_2 \end{pmatrix}, \tag{5.11}$$

where $r = |r|e^{i\varphi_r}$. From this definition it is clear that a classical test of the WEP only accesses the parameters r_1 and r_2 and tests for deviations from $r_1 = r_2 = 1$. A search for quantum WEP violations instead has to access the parameter r using superposition states and tests for deviations from $r = 0$.

With this formalism, whenever $r \neq 0$ the two states $|1\rangle$ and $|2\rangle$ are not eigenstates of the acceleration operator and there is a coupling between them induced by the complex parameter r. In principle it should be possible to detect this coupling by measuring the relative atomic populations before and after a free fall experiment. However since the probability for such transitions will be at least of order r^2 the achievable accuracy with this measurement approach would not be appropriate, considering also that the typical stability of relative atom number measurements is $\sim 10^{-3}$. A much more stringent bound on the parameter r can be accessed by interfering atoms in a coherent superposition of the two energy eigenstates.

Phase shift in the AI

In the experiment, the atomic ensemble at the input of the interferometer can be prepared in three different internal states, i.e. the two energy eigenstates $|1\rangle$ and $|2\rangle$ and in their coherent superposition $|s\rangle$. During the interferometer the evolution of the initial state is governed by a unitary operator $\hat{U}_{MZ}$ which accounts for the interaction with the Bragg lasers and for the free evolution between the interferometric pulses, i.e. for the effect of the gravitational field, including WEP violating terms. Since we are employing Bragg pulses, the interaction with the laser can change only the momentum state without affecting the internal energy level. The coupling between different internal states is therefore only due to the WEP violating term of the Hamiltonian, which contains the operator $\hat{M}_g \hat{M}_i^{-1}$.

Indeed the test Hamiltonian for a particle in a gravitational field, including the quantum formulation of the WEP can be written as

$$\hat{\mathcal{H}} = \hat{M}_i c^2 + \hat{M}_i^{-1} \frac{\hat{p}^2}{2} + g(\hat{M}_g \hat{M}_i^{-1})\hat{M}_i \hat{z}, \tag{5.12}$$

with $\hat{p}$ and $\hat{z}$ the atomic momentum and position operators respectively; in the following we assume that the internal states $|1\rangle$ and $|2\rangle$ are eigenstates of the inertial mass-energy operator $\hat{M}_i$.

In order to calculate the complete phase shift acquired by the atomic wavefunctions in the interferometer when the evolution is governed by the Hamiltonian in Eq. 5.12 one in general needs to solve the full dynamics. Yet this problem is quite complicated due to the couplings between non-commuting internal mass-energies and position and momentum operators. However in the limit of homogeneous gravity the entire gravitational potential can be treated as a perturbation of the free evolution Hamiltonian [42] when evaluating transition amplitudes in the atom interferometer. The same approach can be used also in our case since the parameter $|r|$ cannot be arbitrarily large if the spectrum of $\hat{M}_i$ and $\hat{M}_g$ has to remain positive when violations are present. The total Hamiltonian can therefore be written as $\hat{\mathcal{H}} = \hat{\mathcal{H}}_0 + \epsilon \hat{V}$ where the unperturbed part is $\hat{\mathcal{H}}_0 = \hat{M}_i c^2 + p^2/(2\hat{M}_i)$ while the perturbation part which contains the WEP violating term is $\epsilon \hat{V} = (\hat{M}_g \hat{M}_i^{-1})\hat{M}_i g \hat{z}$. The unitary operator which describes the evolution under the action of $\hat{\mathcal{H}}$ is

$$\hat{U}(t) = e^{-\frac{i}{\hbar}\hat{\mathcal{H}}_0(t-t_0)} - \frac{i\epsilon}{\hbar}\int_{t_0}^{t} dt' e^{-\frac{i}{\hbar}\hat{\mathcal{H}}_0(t-t')}\hat{V}(t')e^{-\frac{i}{\hbar}\hat{\mathcal{H}}_0(t'-t)}, \tag{5.13}$$

to lowest order in ϵ.

The atoms propagate in the two different interferometric arms which are separated only on the momentum degrees of freedom. The time evolution operator in the upper arm is

$$\hat{U}^u = e^{-\frac{i}{\hbar}\int_u dt \hat{H}_0} - i(\hat{M}_g \hat{M}_i^{-1})\frac{3}{2}k_{\text{eff}}gT^2, \tag{5.14}$$

where the second term derives from the integral in Eq. 5.13 which in the above equation corresponds to integrating the atomic trajectory along the upper arm. On the lower arm we analogously have

$$\hat{U}^d = e^{-\frac{i}{\hbar}\int_d dt \hat{H}_0} - i(\hat{M}_g \hat{M}_i^{-1})\frac{1}{2}k_{\text{eff}}gT^2. \tag{5.15}$$

Here $k_{\text{eff}} = 6k$ is the effective wave-number for a 3rd order Bragg diffraction process. The dynamics of the atomic wave-function in the interferometer is finally described by the evolution operator $\hat{U} = \frac{1}{2}(\hat{U}^u - \hat{U}^d)$.

At the output of the interferometer we measure the relative atomic populations in the momentum state $n = 0$ (i.e. the non deflected momentum state). We can choose to count the atoms in $|1\rangle$ and $|2\rangle$ with the same detection channel or to selectively probe them in two state selective detection channels. Depending on the initial atomic state at the input of the interferometer we measure the following transition probabilities:

- Initial state $|1\rangle$

$$|\langle 1|U|1\rangle|^2 = \frac{1}{2}[1 - \cos(k_{\text{eff}}gT^2 r_1)]. \tag{5.16}$$

- Initial state $|2\rangle$

$$|\langle 2|U|2\rangle|^2 = \frac{1}{2}[1 - \cos(k_{\text{eff}}gT^2r_2)]. \tag{5.17}$$

- Initial state $|s\rangle$

$$
\begin{aligned}
|\langle 1|U|s\rangle|^2 &= \frac{1}{2}|\langle 1|U|1\rangle + e^{i\gamma}\langle 1|U|2\rangle|^2 \\
&= \frac{1}{2}[|\langle 1|U|1\rangle|^2 + |\langle 1|U|2\rangle|^2 + 2\mathrm{Re}(\langle 1|U|1\rangle e^{-i\gamma}\langle 1|U|2\rangle^*)]
\end{aligned} \tag{5.18}
$$

or

$$
\begin{aligned}
|\langle 2|U|s\rangle|^2 &= \frac{1}{2}|\langle 2|U|1\rangle + e^{i\gamma}\langle 2|U|2\rangle|^2 \\
&= \frac{1}{2}[|\langle 2|U|2\rangle|^2 + |\langle 2|U|1\rangle|^2 + 2\mathrm{Re}(\langle 2|U|2\rangle^* e^{-i\gamma}\langle 2|U|1\rangle)]
\end{aligned} \tag{5.19}
$$

From Eqs. 5.16, 5.17 we obtain the expected interference fringes of the atomic population, oscillating with a phase proportional to $a_1 = gr_1$ and $a_2 = gr_2$. A measurement of the differential free fall acceleration experienced by atoms in $|1\rangle$ and $|2\rangle$ provides a classical WEP test which can access only the parameters r_1 and r_2.

Let us now consider Eqs. 5.18, 5.19. In both of them the first term is the leading one since it depends on the acceleration a_1 or a_2. The second term accounts for the transitions between $|1\rangle$ and $|2\rangle$ stimulated by the WEP-violating terms in U. This term is expected to be very small since it is of order r^2; the last term is of order r instead. We note also that $\langle 1|U|2\rangle = \langle 2|U|1\rangle^*$.

To lowest order in $|r|$, r_1 and r_2 we obtain

$$
\begin{aligned}
|\langle 1|U|s\rangle|^2 &\simeq \frac{1}{4}[1 - \cos(k_{\text{eff}}gT^2(r_1 + |r|\cos(\gamma\varphi_r)))], \\
|\langle 2|U|s\rangle|^2 &\simeq \frac{1}{4}[1 - \cos(k_{\text{eff}}gT^2(r_2 + |r|\cos(\gamma\varphi_r)))].
\end{aligned} \tag{5.20}
$$

Furthermore, when working with the superposition state the detection can be simultaneous in both the $|1\rangle$ and $|2\rangle$ states (only one detection channel for both states). In this case we measure

$$|\langle 1|U|s\rangle|^2 + |\langle 2|U|s\rangle|^2 \simeq \frac{1}{2}\left[1 - \cos\left(k_{\text{eff}}gT^2\left(\frac{r_1 + r_2}{2} + |r|\cos(\gamma + \varphi_r)\right)\right)\right]. \tag{5.21}$$

Our experiment is thus sensitive to the following accelerations

$$
\begin{aligned}
a_1 &= g\langle 1|\hat{M}_g\hat{M}_i^{-1}|1\rangle = gr_1, \\
a_2 &= g\langle 1|\hat{M}_g\hat{M}_i^{-1}|1\rangle = gr_1, \\
a_s &= g\langle s|\hat{M}_g\hat{M}_i^{-1}|s\rangle = g\left[\frac{r_1 + r_2}{2} + |r|\cos(\varphi_r + \gamma)\right].
\end{aligned} \tag{5.22}
$$

When using the superposition state the phase shift accumulated by the atoms shows a term proportional to $|r|$. We remark that in the experiment we do not have control over the phase term γ which stems both from the preparation of the atomic sample at the input of the interferometer and the free evolution. This random phase term varies from one measurement to the other and introduces excess phase noise in the data. From this result we obtain that a measurement of the mean value of the
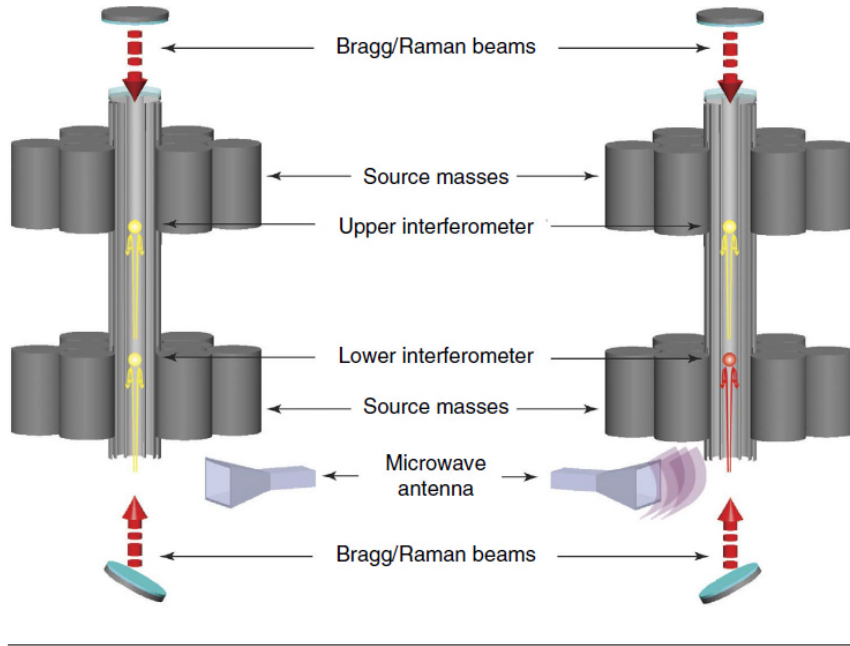
FIGURE 5.5: Schematic view of the experiment. Two cold clouds of ^{87}Rb atoms are launched vertically and prepared in the $|1\rangle$ state with three velocity selective Raman pulses. Before the interferometric sequence, we can apply a microwave pulse on the lower sample to prepare it in the state $|2\rangle$ or $|s\rangle$, while the upper sample is always in state $|1\rangle$. The acceleration of the lower sample is then measured with respect to the upper sample which is used as a common reference. The position of the source masses was chosen in order to maximize the gravity gradient between the two samples. Figure taken from [25].

interferometric phase can provide a classical WEP test, but a measurement of the phase noise affecting the data set yields an upper limit for the parameter $|r|$ thus testing the quantum formulation of the WEP.

5.2.2 Experimental realization and data analysis

The measurements are performed with the gradiometer based on third order Bragg diffraction processes for the atom-optical elements. We use the juggling technique, already introduced in Sec. 4.1.1 to produce the two freely falling samples with a vertical separation of 30 cm which are then simultaneously probed in the gradiometer. After the launch the velocity selection is obtained with three Raman square pulses, each of them with a duration of 192 μs. After this procedure the atomic samples are composed of $\sim 10^5$ atoms in the $|F = 1, m_F = 0\rangle$ state with a transversal temperature of ~ 4 μK and a vertical velocity distribution of $\sim 0.16 v_r$ at full-width at half maximum ($v_r = 5.8$ mm/s).

For this experiment, we added the possibility of applying a microwave pulse on the lower sample before the interferometer sequence; the pulse is applied with a patch antenna when the atoms traverse the detection chamber during their ascent; it is resonant with the ^{87}Rb ground state hyperfine transition $|F = 1, m_f = 0\rangle \rightarrow |F = 2, m_f = 0\rangle$ and can be used to prepare the lower cloud in each of the three states $|1\rangle$, $|2\rangle$ or $|s\rangle$.

The interferometer takes place when the two atomic samples are well inside the magnetically shielded region of the interferometric tube. The position of the source masses is set in order to maximize the gravity gradient experienced by the samples,
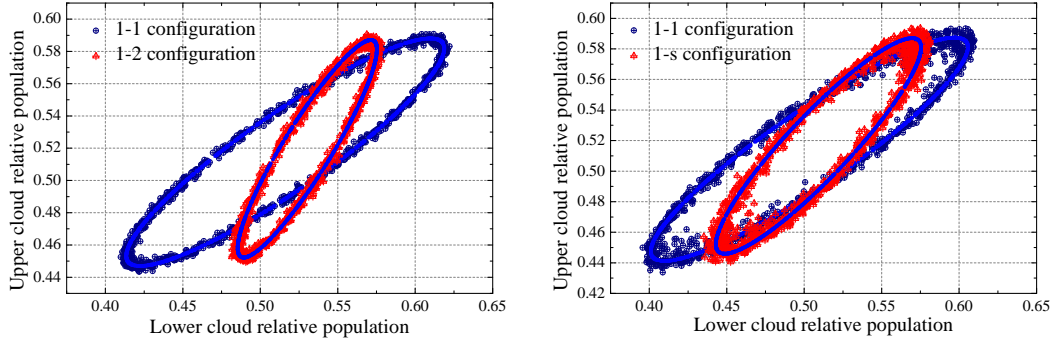
FIGURE 5.6: Gradiometric ellipses for the three different configurations of the Bragg gradiometer and respective best fitting ellipses (in blue). (Left) Ellipses for the 1-1 configuration (blue crosses) and for the 1-2 configuration (red crosses) from which we derive a classical WEP test. (Right) Ellipses for the 1-1 configuration (blue crosses) and 1-s configuration (red crosses) from which we derive the quantum WEP test. For the interferometer on the $|2\rangle$ state we always observe a loss of contrast which we attribute to the defocusing effect experienced by the atoms and due to the blue detuning of the Bragg lasers.

thus maximising also the gradiometric signal. The Bragg interferometric pulses realize a symmetric MZ geometry ($\pi/2 - \pi - \pi/2$ pulses) and have a Gaussian time envelope with a width $\sigma = 12$ μs (~ 28 μs FWHM). The experimental apparatus for this measurement is reported in Fig. 5.5.

Since the upper atomic cloud is always in the $|1\rangle$ state, while the lower one can be manipulated with the micro-wave pulse, our gradiometer can be operated in three different configurations: with both samples in state $|1\rangle$ (1-1 configuration), with the upper sample in state $|1\rangle$ and the lower in state $|2\rangle$ (1-2 configuration), with the upper sample in state $|1\rangle$ and the lower in the superposition state $|s\rangle$ (1-s configuration). Given that the gradiometric signal reflects the difference in acceleration between the two simultaneous interferometers, in our experiment the acceleration of the lower cloud, in each different internal state, is measured using the upper cloud as a common reference.

We note that the two atomic samples of the gradiometer are interrogated during the interferometer with the same Bragg lasers irrespective of the atomic internal state; i.e. the same Bragg lasers are used to realize two atom interferometers acting on the two orthogonal internal states $|1\rangle$ and $|2\rangle$. For the first interferometer the Bragg transitions are red detuned, while for the second interferometer they are blue detuned. However the detuning of the Bragg lasers with respect to the transition $5^2S_{1/2}|F = 2\rangle \rightarrow 5^2P_{3/2}|F' = 3\rangle$ satisfies the condition

$$\Omega_{\text{eff}}^{F=1} = \Omega_{\text{eff}}^{F=2}, \tag{5.23}$$

with $\Omega_{\text{eff}}^{F=1,2}$ the effective Rabi frequency for Bragg transitions starting from the hyperfine ground state with $F = 1, 2$. This detuning is 3.1816 GHz and can be calculated considering that we use two counter-propagating Bragg lasers of equal intensity with $\sigma^+ - \sigma^-$ polarizations.

From the three gravity gradiometer configurations we can derive three different phase angles Φ_{1-1}, Φ_{1-2}, Φ_{1-s}. Indeed for each configuration we obtain a Lissajous figure by plotting the normalized population of the upper interferometer as a function of the normalized population measured at the lower interferometer. The phase

TABLE 5.1: Measurement systematics

Effect	Uncertainty on $\delta g/g (\times 10^{-9})$
AC Stark shift	2.6
Second order Zeeman shift	0.6
Ellipse fitting	0.3
Other effects	<0.1

angle is then derived from the eccentricity and rotation angle of the best fitting ellipse [93]. Combining these three results we obtain the differential acceleration experienced by the lower sample when prepared in the $|2\rangle$ or $|s\rangle$ states with respect to the $|1\rangle$ state: $\delta g_{1-2} \propto \Phi_{1-1} - \Phi_{1-2}$ and $\delta g_{1-s} \propto \Phi_{1-1} - \Phi_{1-s}$.

We stress again that the final detection can be realized by counting the atoms in $|1\rangle$ and $|2\rangle$ with the same detection channel[1] (combined detection) or by independently addressing them in two distinct detection channels (state selective detection). We realize two experiments using both the detection techniques.

In a first measurement we use the combined detection, avoiding in this way any systematic shift coming from asymmetries in the distinct detection channels. During the data acquisition we apply the k-reversal protocol by periodically reversing the sign of the atomic imparted momentum and we alternate the different gradiometric configurations: 1-1 and 1-2 for the classical WEP test; 1-1 and 1-s for the quantum WEP test. With this procedure we acquired the two data sets reported in Fig. 5.6.

The systematic error budget for this measurement is reported in Tab. 5.1. We note that a strong point of our experiment is its robustness against the typical systematics that affect WEP tests with AIs. The use of microwave photons for the preparation of the lower sample ensures that the atomic motion is basically not perturbed and the atoms in $F = 1$ and $F = 2$ does not separate spatially. Therefore any phase shift introduced by the Coriolis acceleration and by local gravity gradients is negligible. The use of the detuning for which $\Omega_{\text{eff}}^{F=1} = \Omega_{\text{eff}}^{F=2}$ guarantees equal losses for the Bragg interferometers on the $F = 1$ and $F = 2$ states and the implementation of the k-reversal protocol rejects the effects which do not depend on the direction of the Bragg lasers wave-vector.

The major source of systematic error arises from AC Stark shifts due to intensity variations of the Bragg lasers wave-front along the propagation direction. The intensity variations are mainly due to diffraction from the limited apertures of the optics needed to deliver the Bragg beams on the atoms. The phase shift is introduced at the moment of the π pulse, when the spatial splitting between the interferometric arms is maximum. The sign of the systematic shift depends on the detuning of the Bragg lasers while its amplitude is proportional to their spatial intensity gradient. We provide an upper limit for the corresponding phase shift by calculating the intensity profile of the Bragg beams along the propagation direction [94]; we then average it over the atomic sample dimensions and finally evaluate the phase shift where the intensity gradient is maximum. The calculation was validated by comparing the phase angle measured with the gradiometer in the 1-1 configuration operated with red or blue detuned Bragg lasers.

---

[1]Considering the scheme of our detection chamber in Fig. 4.6 this is possible by blocking the first layer of resonant light and by using the channel usually dedicated to the detection of atoms in $F = 1$ to measure also atoms originally in $F = 2$.
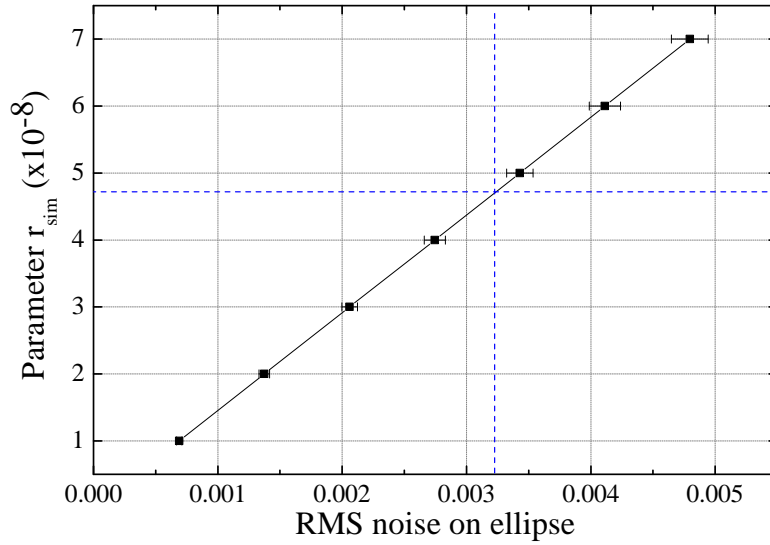
FIGURE 5.7: The parameter r_{sim} of our model for the phase noise as a function of the RMS noise level derived on the simulated ellipses with respect to the best fitting ellipse. The experimental 1-s ellipse shows a RMS noise of 0.0032 which corresponds to a bound of 5×10^{-8} on $|r|$. The error bars are calculated as $\sigma_{RMS} = RMS/\sqrt{N}$ with N the number of data points in the ellipse.

The systematic contribution from the ellipse fitting procedure derives from the Bayesian analysis of the experimental data that we use to extract the gradiometric phase angle from the elliptical signals. The systematic contribution introduced by this method depends on the knowledge of the noise power spectral density affecting the data [93]. We can evaluate its contribution by simulating gradiometric data sets affected by Gaussian differential phase noise with RMS similar to the one present in our experimental data.

Taking into account these contributions we derive the following Eötvös ratios

$$
\begin{aligned}
\eta_{1-2} &= (1.4 \pm 2.8) \times 10^{-9}, \\
\eta_{1-s} &= (3.3 \pm 2.9) \times 10^{-9}.
\end{aligned}
\tag{5.24}
$$

These two values test the classical WEP since they both provide a direct measurement of $r_1 - r_2$ (see Eq. 5.22).

The parameter $|r|$ can be accessed considering the phase noise observed on the ellipse for the 1-s configuration (see Fig. 5.6 (Right)). An upper bound on $|r|$ can be established by attributing all the observed phase noise to a quantum WEP violation. The upper limit is derived simulating ellipses after the introduction of non-common phase noise between the two simultaneous interferometers. The model for the phase noise is $k_{eff}gT^2 r_{sim} \cos(\theta) = 6kgT^2 r_{sim} \cos(\theta)$ (see Eq. 5.21) with θ randomly varied between 0 and 2π. We then measure the root mean square (RMS) noise level on the simulated data points for different values of the parameter r_{sim} (see Fig. 5.7) and confront it with the one measured on the experimental data points for the 1-s ellipse. By attributing all the noise observed on this ellipse to a quantum WEP violation we can provide the upper limit for $|r|$ as the amplitude r_{sim} which provides the same
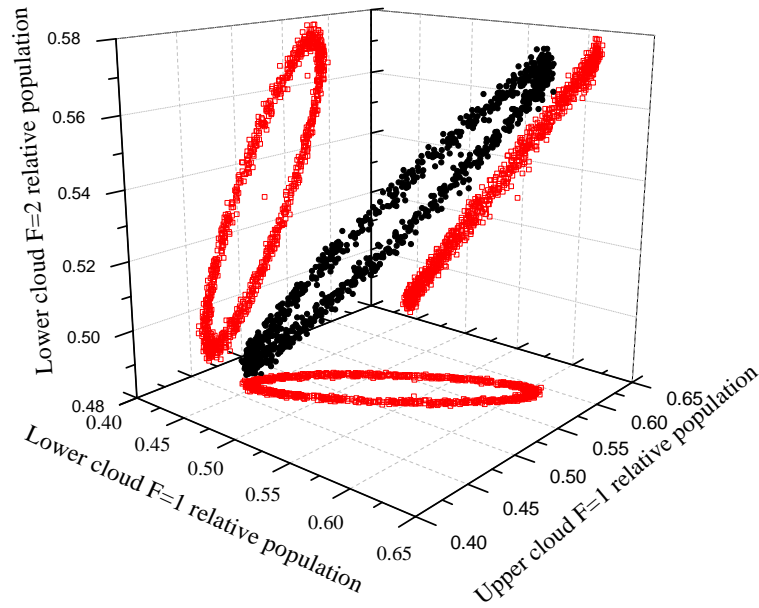
FIGURE 5.8: Three-dimensional Lissajous figure obtained plotting the data from the Bragg gradiometer in the 1-s configuration when the detection is realized with the state selective procedure. We also show the orthogonal projections of the ellipse on the Cartesian axes.

observed RMS noise (see blue line in Fig. 5.7). We estimate an upper limit of

$$|r| < 5 \times 10^{-8}. \tag{5.25}$$

We then perform a second measurement, this time operating the gradiometer only in the 1-s configuration and using the state selective detection procedure. We acquired a total of 4320 points applying the k-reversal procedure; Fig. 5.8 shows the three-dimensional ellipse obtained from the three conjugated gradiometers. Since the ^{87}Rb atoms in $F = 1$ and $F = 2$ are detected with two independent channels, we have to consider the systematic effect introduced by any asymmetry between the two channels. This systematic can be evaluated by operating the gradiometer in the 1-2 configuration and by comparing the phase angles Φ_{1-2} measured when counting $F = 2$ atoms via the first or the second detection channel. We found a discrepancy between the two detection channels which amounts to (38 ± 3) mrad. After considering this effect we obtained an Eötvös ratio of

$$\eta_{1-2} = (1.0 \pm 1.4) \times 10^{-9} \tag{5.26}$$

for the classical WEP test and an upper limit on the $|r|$ parameter again of

$$|r| < 5 \times 10^{-8} \tag{5.27}$$

In summary, we provided a test of the Weak Equivalence Principle both in the classical and quantum regimes. To our knowledge this was the first time that such a quantum test was performed experimentally and we detected no violation at the level of a few parts in 10^{-8}. Furthermore we improved by almost two orders of magnitude the result on the Eötvös parameter for classical WEP tests performed with AIs on atoms in different energy eigenstates. The measurement is presently limited by

the AC Stark shift due to the intensity gradients of the interferometric beams. Improvements to the achievable sensitivity could be obtained employing higher power laser beams together with light shift compensation schemes [95]. Using states with an energy difference larger than the one of the ^{87}Rb ground state hyperfine splitting could be advantageous assuming that WEP violations increase with the considered energy difference [96].

5.3 Measurement of the gravitational acceleration through matter-wave velocimetry

We already stated that the state of the art for the precision measurement of inertial forces and accelerations, in particular the gravitational acceleration, is represented by cold atom interferometry. However, especially in the case of transportable apparatuses, the seismic noise along the measurement axis often poses limits on the achievable sensitivity. There are two possible mitigation strategies for this problem.

The more direct approach relies on the use of seismic isolation systems installed directly on the measurement platform to reduce the acceleration noise; in this case a possible drawback derives from the bulky structure of the typical seismic isolation systems. This can constitute a major obstacle in the development of transportable and sturdy set-ups devised to work in severe environmental conditions and in presence of high vibration noise.

The second approach uses an additional mechanical accelerometer to perform two simultaneous acceleration measurements; the data from the mechanical accelerometer is then used to calculate the correction to be applied to the transition probabilities of the AI [97], [98]. Regarding this second approach we have to consider that the mechanical accelerometer can introduce errors depending on its response function; furthermore, below a few tens of Hz the rejection ratio of typical mechanical accelerometers reduces drastically because of their typical low-pass filter behaviour.

We also note that a conceptually similar post correction technique was applied in [99] where the mechanical accelerometer was replaced by a second AI. The two atomic clouds were interrogated in a gradiometer configuration and the signal of one AI was used to reconstruct the interferometric fringes of the other. In this way, when the phase noise due to mechanical vibrations is comparable with the 2π phase folding interval, it is possible to extract the gravitational acceleration.

We now present a gravimetric scheme which could be particularly useful in presence of high vibration noise. The method relies on high-sensitivity velocimetry measurements done with a Ramsey type AI [100]. We also present a comparison between the sensitivities achievable with our velocimetry measurement scheme and with a Ramsey-Bordé interferometer.

5.3.1 Theoretical overview

In Sec. 2.2 we saw that the phase shift ϕ of a vertical MZ interferometer, in presence of a uniform gravity field, is proportional to the gravitational acceleration g (see Eq. 2.58). This phase shift can therefore be used to realize a measurement of the gravity acceleration. The new gravimetric scheme that we introduce is instead based on a simpler Ramsey interferometric geometry which uses only two Raman $\pi/2$ pulses in rapid sequence. Indeed, in our set-up the typical free evolution time between the two interferometric pulses is limited to T=200 μs, i.e. three orders of magnitude shorter than our usual free evolution time for the MZ interferometer (e.g. see Fig. 5.20). This is due to the absence of the central π mirror pulse used to redirect the atomic trajectories towards each other before the last $\pi/2$ pulse which closes the interferometer. In the Ramsey scheme the two interferometric arms do not overlap perfectly at the moment of the last pulse; however, due to the short free evolution time T employed, we still maintain a sufficient wave-packet superposition at the moment of the closing $\pi/2$ pulse to observe interference. In Fig. 5.9 we report the conceptual scheme of the employed Ramsey geometry.
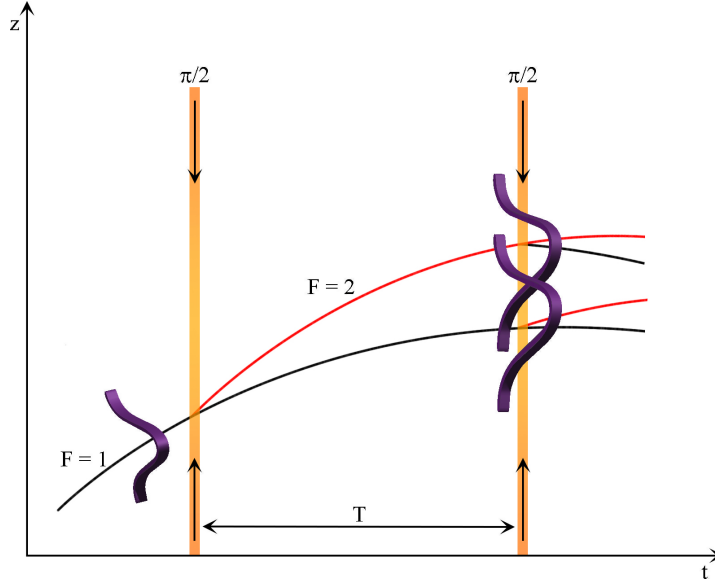
FIGURE 5.9: Conceptual scheme of the Ramsey interferometer. The geometry is composed of only two $\pi/2$ pulses realized with counter-propagating Raman transitions. The free evolution time T between the two pulses has to be short enough to ensure a considerable spatial superposition of the atomic wave-functions at the moment of the last $\pi/2$ pulse in order to maintain the interferometer contrast. The chosen T is therefore the result of a trade-off between interferometer sensitivity and contrast.

In the Ramsey scheme the interferometric phase can be written as

$$\phi = \left[k_{\mathrm{eff}}(v + v_{\mathrm{rec}}/2) - \omega_D\right]T, \tag{5.28}$$

with v the atomic velocity and v_{rec} the recoil velocity; the frequency $\omega_D = \omega_{\mathrm{eff}} - \omega_{\mathrm{HFS}}$ takes into account the changing Doppler effect due to the atomic free fall and it is derived from the effective Raman frequency ω_{eff} and the resonance frequency of the hyperfine doublet of the ^{87}Rb ground state $\omega_{\mathrm{HFS}} = 6.835$ GHz. From the above equation we note that the interferometer sensitivity to atomic velocities increases linearly with the free evolution time T; for this reason the chosen $T = 200$ μs is the result of the trade-off between interferometric sensitivity and contrast. In Fig. 5.10 we compare the interferometric fringes for three different interrogation times T. The fringes are scanned adding a detuning to the Doppler compensation frequency ω_D in steps of 100 Hz. We note that as expected from Eq. 5.28 the periodicity of the interferometric fringes depends on the chosen T and for $T = 200$ μs (blue signal) we obtain a complete 2π phase scan when the detuning is varied in the interval [0 - 5] kHz.

In Fig. 5.11 we compare the sensitivities to acceleration noise of the Ramsey interferometer and of the Mach-Zehnder interferometer using their transfer functions $H(\omega)$ already defined in Sec. 2.2.3. Indeed we know that in presence of a noise power spectral density $S(\omega)$ of the Raman phase, the variance of the interferometer phase can be written as (see Eq. 2.83)

$$\sigma_\phi^2 = \int_0^\infty |H(\omega)|^2 S_\phi(\omega) \frac{d\omega}{2\pi}. \tag{5.29}$$
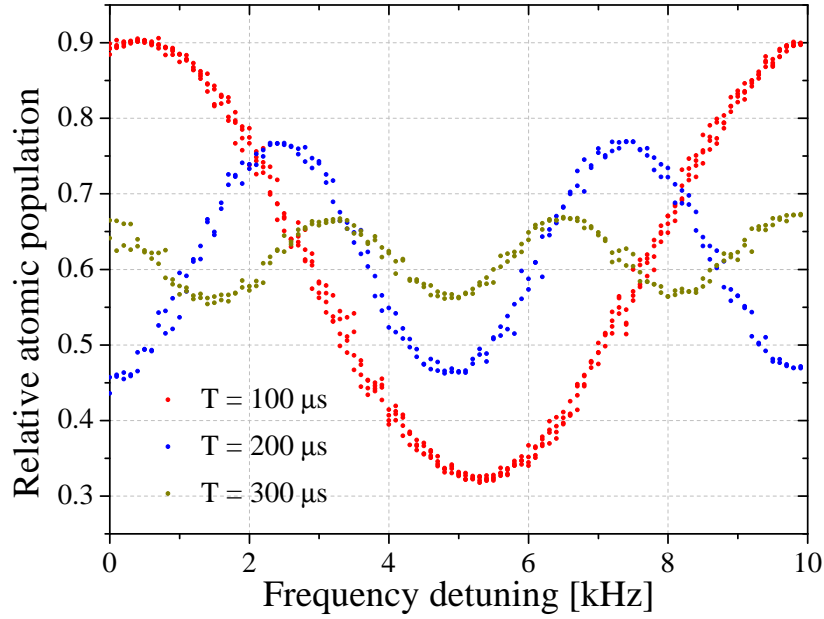
FIGURE 5.10: Interferometric fringes obtained in the Ramsey configuration for three different interrogation times T. The contrast decrease for higher T forced us to use pulses of $T = 200$ μs. The fringes are scanned adding a frequency detuning to the Doppler compensation frequency ω_D (each experimental point corresponds to a 100 Hz change).

Considering frequencies $\omega \ll \Omega_{\text{eff}}$ (with Ω_{eff} the effective Rabi frequency of the Raman pulses), the acceleration transfer function for a standard MZ interferometer is proportional to [43]

$$|H_a(\omega)| = 4\sin^2\left(\frac{\omega T}{2}\right), \tag{5.30}$$

while in the case of the Ramsey interferometer, in which the phase is proportional to the atomic velocity, we obtain

$$|H_v(\omega)| = 2\sin\left(\frac{\omega T}{2}\right). \tag{5.31}$$

The MZ transfer function reported in Fig. 5.11 (black trace) was calculated considering a MZ free evolution time of $T = 10$ ms which corresponds to the optimal value that we could obtain in the vibration noise conditions of our laboratory (without any seismic isolation or post correction). The Ramsey transfer function (green trace) is instead calculated for the optimal condition of $T = 200$ μs. In the frequency range from 0.5 Hz to 500 Hz we note that due to the dependence of the Ramsey interferometric phase on the atomic velocity (rather than the atomic acceleration as in the standard MZ case) and due to the short free evolution time T, the Ramsey interferometer is more robust against vibrational noise than the MZ interferometer. In the considered range of frequencies the seismic and acoustic noise is particularly problematic for AIs; however, the Ramsey scheme with its particular transfer function, can provide attenuation factors to the power noise spectral density which go up to two orders of magnitude with respect to the levels achieved with a MZ interferometer.
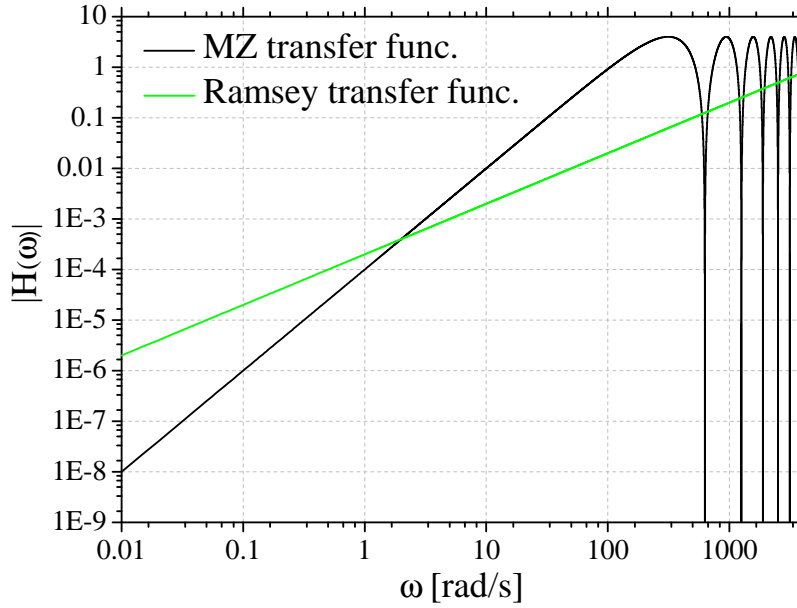
FIGURE 5.11: Absolute value of the transfer functions for a standard MZ interferometer in black and a Ramsey interferometer in green. The functions were calculated for a MZ free evolution time $T = 10$ ms and a Ramsey free evolution time $T = 200$ μs.

5.3.2 Experimental realization

In our set-up we exploit the velocity dependence of the Ramsey interferometer phase to realize a gravimetric measurement. To extract the gravity acceleration we perform two velocimetry measurements separated by a known time T_c; the measurements are realized on two different atomic samples in free fall inside the interferometric tube. The differential phase $\Delta\phi$ between the two Ramsey interferometers provides a measure of the velocity variation over the separation time T_c, i.e.

$$\Delta\phi = [k_{\text{eff}}(v_2 - v_1) - (\omega_{D,2} - \omega_{D,1})]T = (k_{\text{eff}}g - \alpha)TT_c, \tag{5.32}$$

where $\alpha = (\omega_{D,2} - \omega_{D,1})/T_c$ represents the slope of the linear frequency ramp applied to the Raman lasers to compensate for the changing Doppler effect due to the atomic free fall. From the measurement of the velocity variation we then recover the value of the gravitational acceleration which produced it.

The experimental set-up is the usual ^{87}Rb fountain. We collect $\sim 10^9$ atoms in the 3D-MOT and launch them vertically with the moving molasses. During the launch the temperature of the sample is further reduced with a sub-Doppler cooling stage down to ~ 4 μK. Before entering the tube, the sample is prepared in the $|F = 1, m_F = 0\rangle$ state and selected in a narrow vertical velocity class with our triple velocity selection procedure. For the velocity selection we use square Raman pulses with a duration of 192 μs which select a vertical velocity class corresponding to a temperature of $T_z \simeq 1$ nK.

The same launch and preparation procedure is repeated after 484 ms while the first launched sample is still in free fall inside the interferometric tube. We thus obtain two freely falling samples which are then probed in two independent Ramsey
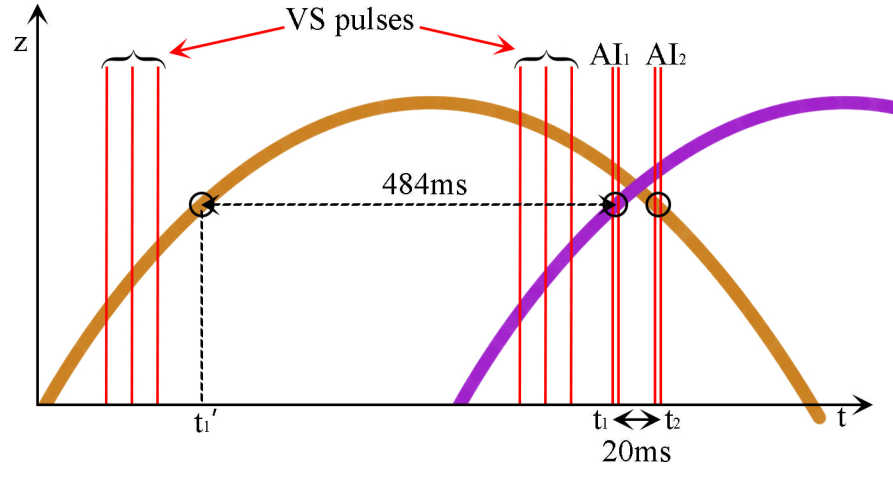
FIGURE 5.12: Parabolic trajectories of the two launched atomic clouds (in orange and purple). The time sequence of the Raman pulses is shown with the vertical red lines both for the velocity selection and the interferometric interrogation stages. The two atom interferometers are labelled as AI_1 and AI_2 and take place at time t_1 and t_2 respectively. The upward and downward moving samples can be interrogated independently thanks to the different Doppler effect that they experience. The effective separation between the two interferometric interrogations is $T_c = 504$ ms.

interferometers when they are moving with the same velocity in modulus, but opposite in sign. Fig. 5.12 reports the described procedure; the atomic sample launched last is interrogated at time t_1 while it is moving upward with velocity v; the second interferometer is realized at time t_2 and interrogates the atomic sample launched first while it is moving downward with a velocity $-v$. The actual time separation between the two successive interferometers is $t_2 - t_1 = 20$ ms, however considering that the trajectories followed by the two clouds are the same but with a time delay of 484 ms, probing the two clouds at t_1 and t_2 is thus equivalent to probing a single cloud twice at $t'_1 = t_2 - 20$ ms $- 484$ ms and t_2; the free fall time is therefore $T_c = t_2 - t'_1 = 504$ ms.

The interferometer pulses are realized with two Raman lasers resonant with the 6.8 GHz transition between the two hyperfine levels of the ^{87}Rb ground state. They have an effective wave-vector of $k_{\text{eff}} = 1.6 \times 10^7$ m^{-1}; the Master Raman laser has a detuning of 2.2542 GHz on the red with respect to the D2 $5^2 S_{1/2}|F = 2\rangle \rightarrow 5^2 P_{3/2}|F' = 3\rangle$ line. As usual the two counter-propagating Raman lasers are aligned vertically and retro-reflected by the top mirror of our apparatus. We stress out again that this mirror is not seismically isolated in our set-up and is the source of the vibration noise affecting our measurements. As described in Sec. 3.3.5 our Raman laser system is composed of two 1 W tapered amplifiers; for this measurement we added the possibility of stabilizing the amplifier emission power with a servo control on the tapered amplifiers current. The power stabilization loop is realized with a digital proportional-integral controller which acts independently on the two tapered amplifiers with a 3 Hz bandwidth.

In Fig. 5.13 we report the Allan deviation of the error signal of the closed power stabilization loop. The time constant of our correction loop is ~ 1 s. After 1 s we observe the characteristic white noise trend as $1/\sqrt{t}$ (with t the integration time) indicating that our correction loop is working properly.

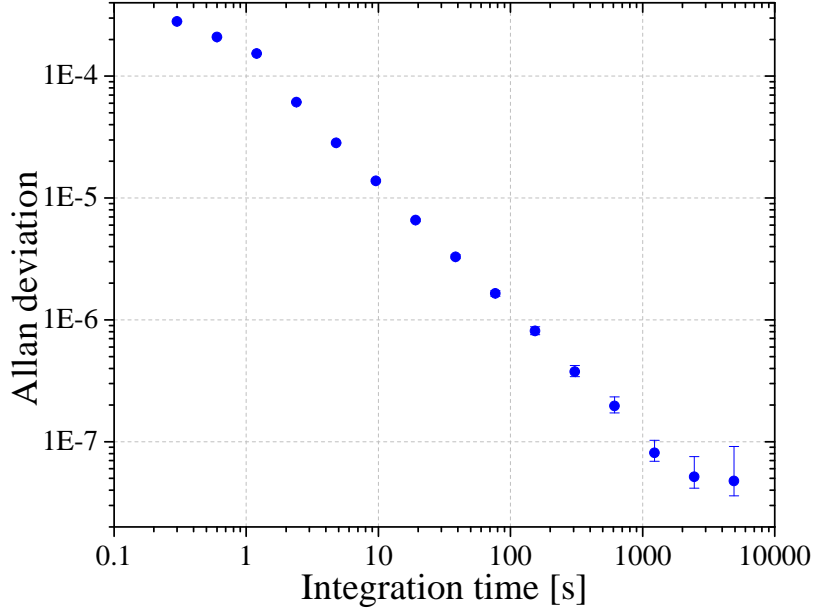When the power control is active we can then set and stabilize the correct power

FIGURE 5.13: Allan deviation of the error signal measured with the closed Raman power stabilization loop.

ratio between the Master and the Slave Raman lasers in order to cancel the systematics arising from the differential light shift [15]; in our apparatus we set $I_s / I_m = 0.47$. The interferometric pulses have a square envelope with a duration of $\tau = 12 \ \mu$s.

Due to the different Doppler effect experienced by the two freely falling samples, the two subsequent Ramsey interferometers interrogate only one atomic sample. Indeed different frequency detunings need to be applied to the Raman lasers during the interferometers AI_1 and AI_2. With the right detuning AI_1 only acts on the ascending cloud (i.e. on the sample launched last), while AI_2 acts on the descending one (i.e. on the sample launched first).

The optimal detuning for the two interferometers was chosen performing a large scan of the Doppler compensation frequency; the chosen ω_D is the one which maximizes the interferometer contrast as shown in Fig. 5.14 for the case of the descending cloud interferometer AI_2.

After the two successive interferometers the atomic population is detected with our state selective detection procedure. For each presented measurement we apply the already introduced k-reversal protocol; we thus reject any systematics which does not depend on the direction of the imparted atomic momentum k_{eff}. An entire experimental cycle lasts about 1.9 s.

In Fig. 5.15 we report the typical collected signals from the interferometers AI_1 (red squares) and AI_2 (blue squares). With the purple squares we also show the Lissajous figure obtained plotting the signal from AI_2 versus the signal from AI_1. The fringes are scanned adding a common varying frequency offset δ to the Doppler compensation frequency used during AI_1 ($\omega_{D,1}$) or AI_2 ($\omega_{D,2}$). At each experimental cycle δ is chosen randomly from a uniform frequency distribution which spans from 0 to 5 kHz and corresponds to a 2π phase shift for a Ramsey interferometer with $T = 200 \ \mu$s (see Fig. 5.10). Since the frequency offset δ is the same for both the interferometers, the frequency slope $\alpha = (\omega_{D,2} - \omega_{D,1})/T_c$ (see Eq. 5.32) is not modified
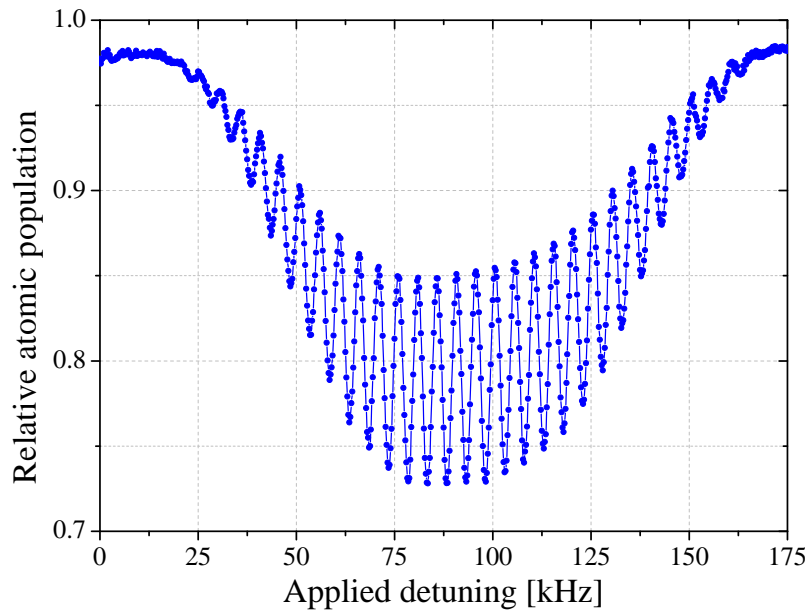
FIGURE 5.14: Interferometric fringe scanned varying the Doppler compensation frequency in steps of 250 Hz in a [0-175] kHz range. The signal is obtained from the descending interferometer AI$_2$. The fringe periodicity is 5 kHz since T = 200 μs. The working condition for the Doppler compensation frequency is set as the one which maximizes the fringe contrast.
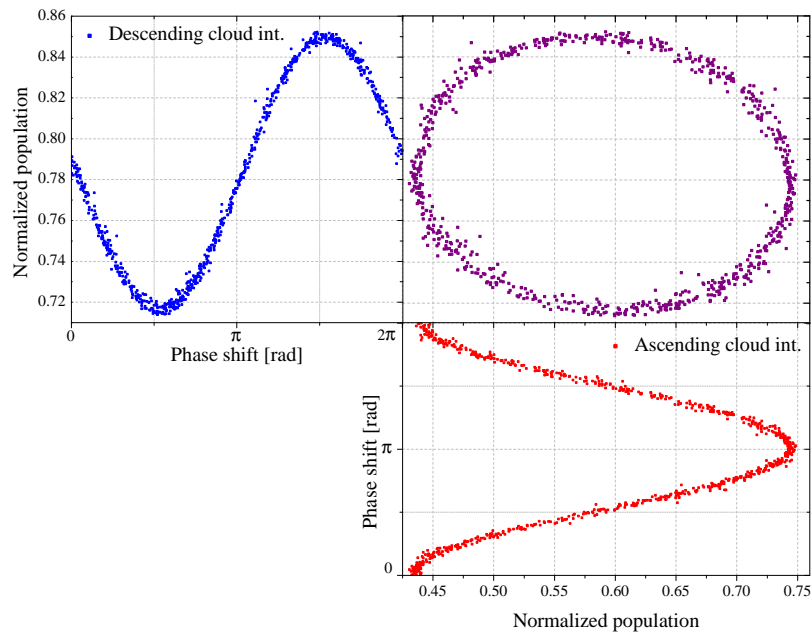

FIGURE 5.15: Interferometric fringe from AI$_1$ (signal from the ascending cloud with the red circles) and from AI$_2$ (signal of the descending cloud with blue circles) and corresponding Lissajous figure (purple squares). The relative phase difference $\Delta\phi$ between the fringes is a measure of the velocity difference between the two atomic samples interrogated by AI$_1$ and AI$_2$ and can be retrieved with an elliptical fit of the Lissajous figure.
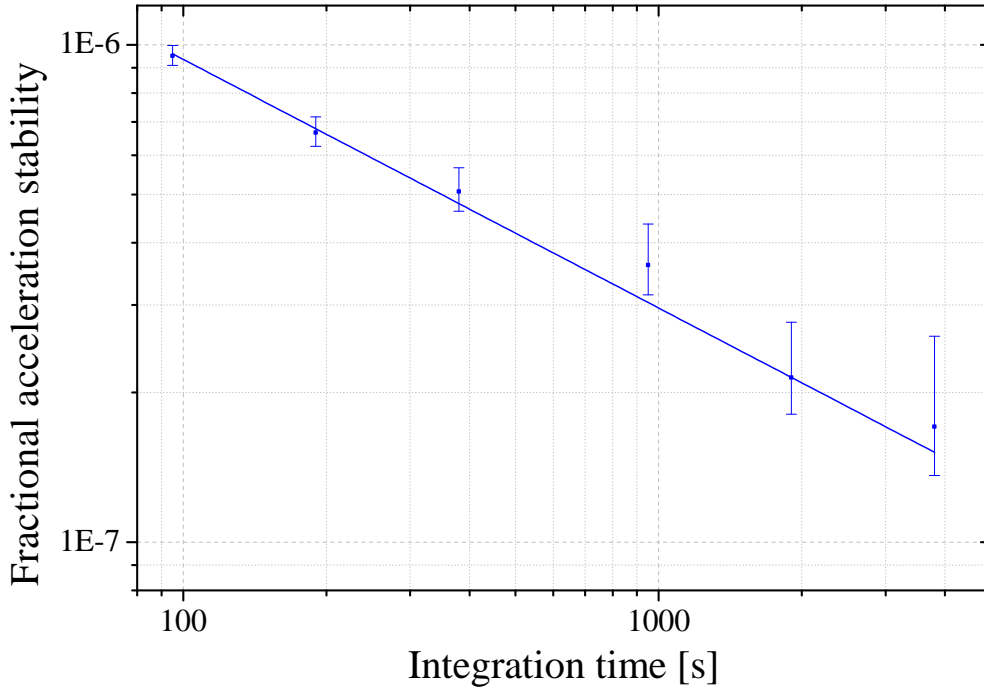
FIGURE 5.16: Allan deviation of the acceleration measurements from an 8-hours measurement run. At 1 s of integration time we measure a fractional acceleration stability of 9×10^{-6} which drops down to 1×10^{-7} after an integration of 6000 s. From this result we can register a performance one order of magnitude better than a standard MZ interferometer without seismic isolation or post correction.

from one experimental cycle to the next. We point out that the relative phase difference between the two interferometers AI_1 and AI_2 $\Delta\phi$ can be set varying the slope α; usually we work in the condition $\Delta\phi \sim \pi/2$ which optimizes the performance of our least squares elliptical fitting procedure.

$\Delta\phi$ contains the information about the velocity difference between the two atomic samples interrogated during the interferometric sequences. As in the case of a gradiometer, this phase angle can be retrieved with an elliptical fit of the Lissajous curve shown in the central panel of Fig. 5.15.

We note that the signal of the descending interferometer shows a lower contrast with respect to the ascending one. This behaviour is due to the 504 ms longer expansion time which the atomic cloud of AI_2 experiences before the interferometric interrogation. The cloud suffers from a stronger heating and thus experiences also larger inhomogeneities in the Raman wave-fronts along its transversal dimensions.

Considering that the differential phase $\Delta\phi$ depends linearly from the slope α (see Eq. 5.32), the gravitational acceleration g can be extracted by performing two measurements of $\Delta\phi$ for two different values of α; with a linear interpolation we then determine the slope $\alpha_0 = k_{\text{eff}} g$ for which $\Delta\phi(\alpha_0) = 0$ and extract the gravitational acceleration as $g = \alpha_0 / k_{\text{eff}}$. We finally note that due to the finite time duration τ of the interferometric pulses the phase shift in Eq. 5.28 is multiplied by an overall scale factor $A(\Omega_{\text{eff}})$ which depends on the effective Rabi frequency[2]. However since in

---

[2]We calculated the scale factor using the sensitivity function approach as $A(\Omega_{\text{eff}}) = \frac{1}{\Omega_{\text{eff}}}[\sin^3(\Omega_{\text{eff}}\tau(2 - 2\cos(\Omega_{\text{eff}}\tau) + \Omega_{\text{eff}} T \sin(\Omega_{\text{eff}}\tau))]$
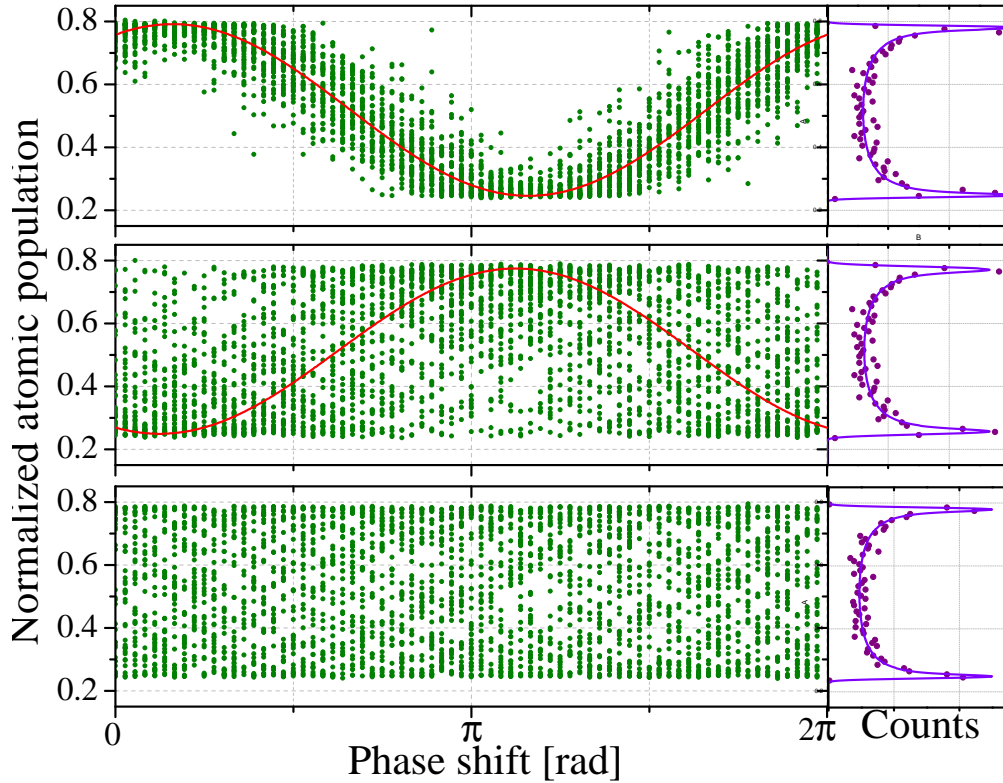
FIGURE 5.17: In the three left panels we plot the interference fringes measured with a standard MZ interferometer. We use three different interrogation times T and no seismic isolation or post correction; from top to bottom $T = 5, 10, 20$ ms. Each data set corresponds to an integration time of 90 min. The red lines are sinusoidal fits of the green experimental data. Due to the seismic noise, for $T = 20$ ms the fit fails to converge. In the right panels we show the histograms of the relative atomic populations together with the corresponding fits [98]. The best measurement conditions are achieved for $T = 10$ ms; in this case we obtain a fractional acceleration stability of 9×10^{-5} at 1 s of integration time.

our set-up we have $\tau = 12$ μs and $T = 200$ μs we do not consider this factor which is negligible in the limit $\tau \ll T$.

With the described technique we measured the gravitational acceleration in our laboratory and compared the result with a previous g determination realized with a mechanical FG5 gravimeter [101]. With a two hours measurement run we obtained the result

$$g = 9.8049234(21) \text{ ms}^{-2}, \tag{5.33}$$

consistent within 2σ with the FG5 measurement $g_{FG5} = 9.80492048(3)$ ms^{-2}.

5.3.3 Sensitivity analysis

We then performed an eight hours measurement run in order to evaluate the sensitivity achievable with our technique. For this measurement we still apply the k-reversal protocol, but we use only one Doppler compensation slope α. In Fig. 5.16 we report the Allan deviation computed for this measurement run. The data show the characteristic $1/\sqrt{t}$ slope (where t is the integration time) typical of white acceleration noise. The fractional acceleration stability at 1 s is 9×10^{-6} and averages down to 1×10^{-7} for an integration of 6000 s. We note than any velocity variation
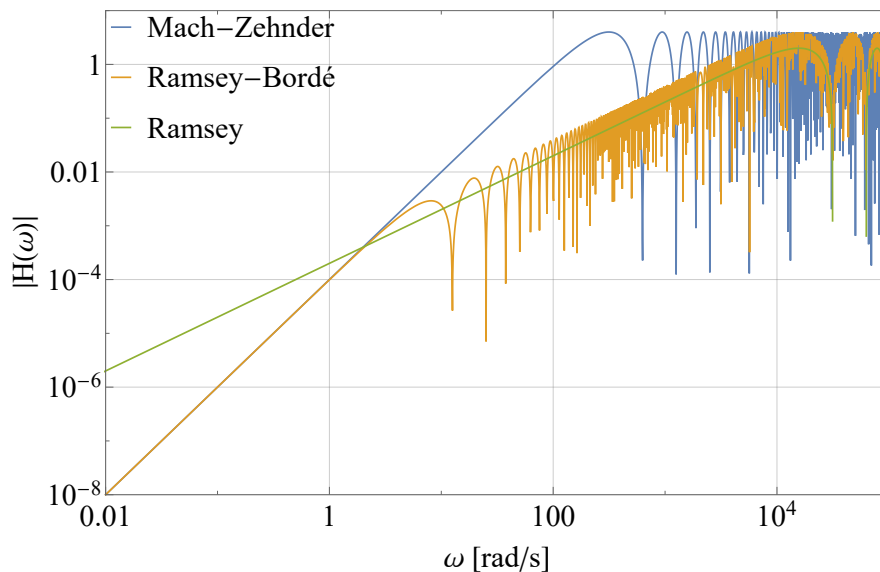
FIGURE 5.18: Transfer functions calculated for a MZ (T_{MZ}=10 ms), a RB (T_{RB}=200 μs, T' = 500 ms) and a Ramsey interferometer (T=200 μs). In the low frequency range the slope of the RB transfer function is the same as the one of the MZ interferometer ($\propto 1/\omega^2$), however in the range from 0.5 Hz to 1.5 kHz the slope changes to the one of the Ramsey interferometer ($\propto 1/\omega$) determining a better rejection of seismic noise than in the MZ case.

introduced during the velocity selection phase by residual light shift effects, limits the long term stability and accuracy of the measurement. In this regard, the power stabilization of our Raman lasers is of crucial importance to control this systematics.

We finally compared the stability results of our novel measurement method with the results obtained in the standard MZ configuration. Using the same experimental apparatus we implemented a MZ interferometer interrogating the atoms with a $\pi/2 - \pi - \pi/2$ Raman pulse sequence and we measured the gravitational acceleration with data acquisitions of 90 min. For these measurements the interferometric fringes are scanned acting on the relative phase between the Raman lasers. In Fig. 5.17 we report the results for three different interrogation times $T = 5, 10$ and 20 ms. We point out that since these measurements are performed with the same experimental apparatus as before they are affected by the same amount of vibration noise. Indeed the interferometric fringes are quickly (i.e. for low T) washed-out by seismic noise and the sinusoidal fit already fails to converge for $T = 20$ ms. We found the best measurement conditions for $T = 10$ ms; in this case we measure a fractional acceleration stability of 9×10^{-5} at 1 s of integration time, which is one order of magnitude lower than the result obtained with our novel measurement technique based on the Ramsey interferometric scheme and atom velocimetry.

We point out that another interesting comparison can be made between the experimental method proposed here and the Ramsey-Bordé (RB) interferometric scheme. The RB configuration is realized with four $\pi/2$ pulses in a T_{RB}-T'-T_{RB} temporal sequence, where T' can be made large compared to T_{RB}. In the RB configuration the part of the phase shift dependent on the gravitational acceleration can be written as [102]

$$\phi_{RB} = k_{eff}g(T_{RB} + T')T_{RB}. \tag{5.34}$$

Therefore, with T_{RB} = 200 μs and T' = 500 ms the sensitivity to inertial forces is the

same as the one of a MZ interferometer with $T_{MZ} = 10$ ms while the rejection of seismic noise is comparable to the one obtained with our proposed measurement method based on Ramsey velocimetry.

This last aspect can be understood considering the sensitivity function of the Ramsey-Bordé interferometer which in the limit of $\omega \ll \Omega_{\text{eff}}$ can be written as (the time origin is set in the middle between the two pairs of $\pi/2$ pulses)

$$
g_s^{RB}(t) = \begin{cases} 0 & \text{for} \quad t < -T'/2 - T_{RB}, \\ -1 & \text{for} \quad -T'/2 - T_{RB} < t < -T'/2, \\ 0 & \text{for} \quad -T'/2 < t < T'/2, \\ +1 & \text{for} \quad T'/2 < t < T'/2 + T_{RB}, \\ 0 & \text{for} \quad T'/2 + T_{RB} < t. \end{cases} \tag{5.35}
$$

From the above equation we note that during the time between the interferometric pulse pairs (of length T') the sensitivity function is null; the Ramsey-Bordé interferometer signal is therefore insensitive to any noise contribution during this period. From the sensitivity function we can derive the corresponding transfer function and compare it with the ones already calculated for the MZ and the Ramsey interferometers. In Fig. 5.18 we show such a comparison between the transfer functions of a MZ ($T_{MZ} = 10$ ms), a RB ($T_{RB} = 200$ μs, T' = 500 ms) and a Ramsey (T = 200 μs) interferometer.

A strong advantage of the RB scheme, with respect to the velocimetry scheme, relies on the fact that the interrogation time T_{RB} can be made larger than the 200 μs used in the Ramsey interferometer. This is due to the fact that in a RB interferometer the atomic trajectories do overlap at the moment of the final beam splitter pulse. Since the interferometer geometry closes at the end of the RB pulse sequence, the contrast does not change with the interrogation time T_{RB} as was the case for the Ramsey geometry (see Fig. 5.10). This allows us to increase the interrogation time in order to reach higher sensitivities. For example, with $T_{RB} = 5$ ms and $T' = 500$ ms the RB sensitivity to inertial effects is a factor of 25 better than the one of a MZ with $T_{MZ} = 10$ ms.

In order to test the sensitivity of the RB scheme we implemented this geometry in our experimental apparatus. The set-up is the same used for the already presented velocimetry measurements. As usual we load, cool and vertically launch a cold ^{87}Rb sample. After the triple velocity selection and during the ascent of the atomic cloud we apply the first pair of Raman $\pi/2$ pulses separated by a time T_{RB}. After these two pulses we shine a vertical resonant pulse to blow-away all the atoms in $F = 2$. The second Raman $\pi/2$ pulse pair is applied during the descent of the atomic cloud after $T' = 504$ ms. As was the case for the velocimetry measurements with this configuration the velocity of the cloud during the first $\pi/2$ pulse pair is the same in modulus as the one during the last $\pi/2$ pulse pair but the sign is opposite. We maintain the resonance of the Raman lasers during all the experimental sequence applying a linear frequency ramp which compensates the changing Doppler effect due to the atomic free-fall motion. The interferometric signal then becomes

$$
\phi_{RB} = (k_{\text{eff}} g - \alpha)(T_{RB} + T')T_{RB}, \tag{5.36}
$$

with α the Doppler compensation ramp. We can then scan the interferometric fringes varying the value of α. In principle the value of the frequency ramp $\alpha_0 = k_{\text{eff}} g$ which
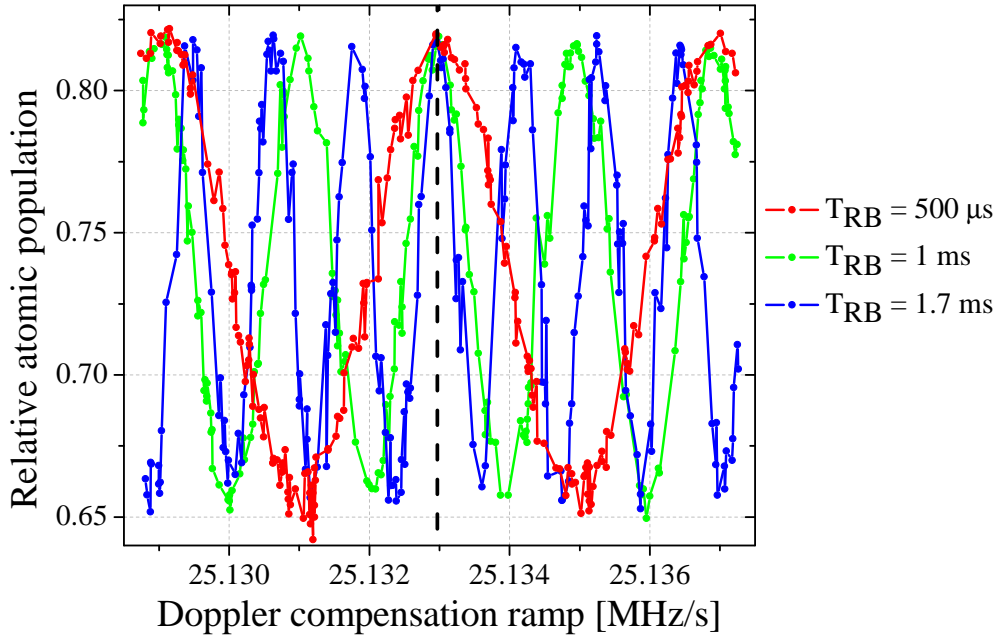
FIGURE 5.19: Interferometric fringes obtained with the RB interferometer for different interrogation times T_{RB}. The fringes are scanned varying the Doppler compensation ramp α. The value $\alpha_0 = k_{eff}g$ which exactly compensates the action of the gravitational acceleration can be identified as the one for which $\phi_{RB} = 0$ irrespective of the interrogation time (black dashed line). We note that since the RB interferometer closes at the end of the pulse sequence there is no contrast change associated to varying T_{RB}.

exactly compensates the change in Doppler effect permits to measure the gravitational acceleration as $g = \alpha_0/k_{eff}$. In particular, when α_0 is applied the interferometric signal is $\phi_{RB} = 0$ for every value of the interrogation time T_{RB}. In Fig. 5.19 we exploited this result to find the central interferometric fringe. The black dashed line in Fig. 5.19 indicates the value α_0. All the successive measurements were realized scanning the Doppler ramp α around the value α_0 in a range which provided a 2π phase span; this range of course depends on the chosen T_{RB}.

To evaluate the measurement sensitivity and stability of the RB interferometer we then performed an 8 h long measurement run; for this measurement we apply the k-reversal protocol already discussed. We use $T_{RB} = 5$ ms and $T' = 504$ ms.

In summary we tested a new gravimetric scheme based on two short Ramsey interferometers. The acceleration of the atomic samples is derived through two matter-wave velocimetry measurements separated by a known time T_c. The presented technique can offer superior performances, in terms of acceleration noise rejection, than a standard MZ gravimeter and can be particularly useful for acceleration measurements in presence of strong vibration noise.

5.4   Gravity gradient phase shift compensation in Atom Interferometers

In this section we report the experimental demonstration of a novel method to compensate the effects of gravity gradients in a MZ interferometer [103]. Taking advantage of the fact that in our apparatus more than one atomic sample can be interrogated simultaneously, we also use the proposed method to measure the gravity gradient and the gravity field curvature.

5.4.1   Theoretical overview

In Sec. 2.2.2 we introduced the phase shift obtained for a vertical atom interferometer in the MZ configuration in presence of a uniform gravity acceleration and gravity gradient γ (see Eq. 2.60). In this conditions we saw that the interferometric phase ϕ depends on the initial position z_0 and velocity v_{z0} of the atoms and that the interferometric trajectories do not close perfectly at the moment of the last beamsplitter pulse. We report here the interferometer phase shift ϕ considering that for the present discussion it is sufficient to focus on the dependence on the initial atomic position and velocity (the term proportional to $-7/12gT^2$ disappears in the gradiometer phase angle)

$$\phi = -k_{\text{eff}}gT^2 + k_{\text{eff}}\gamma_{\text{zz}}(z_0 + v_{z0}T)T^2, \qquad (5.37)$$

where γ_{zz} is the gravity gradient tensor component along the z axis, $\hbar k_{\text{eff}}$ is the momentum imparted to the atoms during the interferometric transitions and T the free evolution time between the interferometric pulses.

   The loss of contrast due to the non perfect closing of the interferometer and the dependence of the phase shift on z_0 and v_{z0} have raised some concerns on the proposed use of AIs for high sensitivity applications [104], e.g. for future tests of the WEP at the 10^{-15} level in the Eötvös ratio [105], [106] or for gravitational wave detection. Usually the WEP tests compare the accelerations measured with two simultaneous interferometers acting on two different atomic species [31]–[34], or on atoms in different internal energy eigenstates [24], [25] and in order to reach accuracies at the 10^{-15} level they would need a control on the relative position and velocity of the atomic samples to better than 1 nm and 0.3 nm/s respectively which are quite challenging requirements. We note that also for the atom interferometry measurement of the Newtonian gravitational constant G [21] the major source of systematic error is due to the limited control on the position and velocity of the atomic ensemble [30]. Also for measurements in geodesy, Earth observation and applied physics which require a precise knowledge of the Earth gravity gradient there are similar problems [107].

   A possible solution to these issues was theoretically proposed in [36]; the proposed solution allows to remove the dependence on the initial conditions from the MZ interferometric phase. We have experimentally demonstrated this technique and used it to measure the gravity gradient and gravity field curvature.

   The method consists in changing the momentum transferred to the atoms during the central π pulse of the MZ atom interferometer of a quantity Δk_{eff}; by appropriately tuning Δk_{eff} it is then possible to compensate the effects of the ambient gravity gradient. In particular with the variation Δk_{eff} the atom interferometer phase is modified by a term $2\Delta k_{\text{eff}}(z_0 + v_{z0}T)$; this extra accumulated phase shift compensates
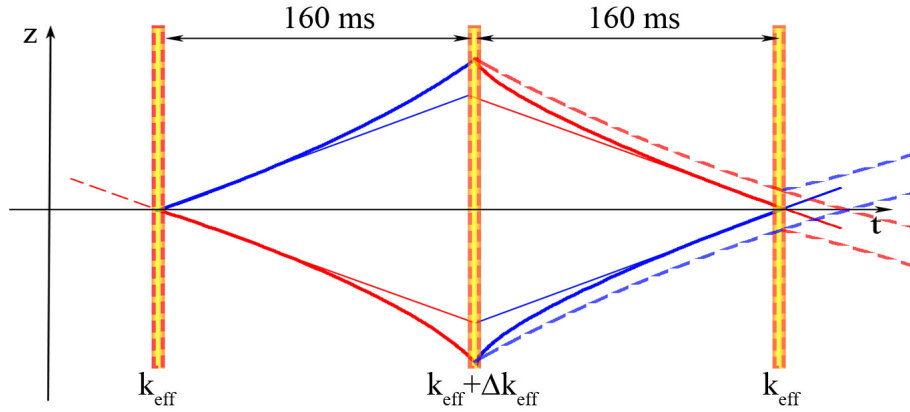
FIGURE 5.20: Space-time trajectories for the atoms in a freely falling MZ interferometer operated with Raman transitions. The thin straight lines represent the case in the absence of a gravity gradient; in this case a symmetric MZ interferometer closes perfectly at the moment of the last $\pi/2$ pulse. The curved dashed lines show the trajectories in presence of a gravity gradient without the compensation scheme active; in this case the perfect wave-packet superposition at the end of the interferometer is lost. The curved thick lines represent the case in which the momentum imparted to the atoms is changed of $\Delta k_{\text{eff}} = -\gamma T^2 k_{\text{eff}}/2$ and the gravity gradient is exactly compensated. In this last case we note that the atomic trajectories overlap again perfectly at the moment of the last $\pi/2$ pulse. Figure adapted from [103].

exactly the term due to the ambient gravity gradient when

$$\Delta k_{\text{eff}} = -\frac{\gamma T^2}{2} k_{\text{eff}}, \tag{5.38}$$

and the dependence on the initial position and velocity of the atomic ensemble is cancelled from the MZ phase shift ϕ.

In Fig. 5.20 we report the principle of operation of the proposed method for a Raman MZ interferometer. The atomic trajectories in presence of a gravity gradient do not overlap perfectly at the end of the interferometer (dashed lines in Fig. 5.20), however the change Δk_{eff}, introduced during the π pulse can reverse the atomic trajectories symmetrically (thick, curved lines) and compensate for the momentum change due to the tidal forces from the gravity gradient. When the compensation is active the atomic trajectories do overlap at the end of the interferometer preventing any loss of contrast from a non perfect wave-packet superposition.

5.4.2 Experimental realization

The measurements are performed with the atom interferometer based on Raman transitions as atom-optical elements. We vertically launch three cold clouds (4 μK) of ^{87}Rb atoms after trapping and cooling them in the 3D-MOT. For this launch we do not use the juggling technique; we perform instead a sequential cloud launch. When the three samples are in the interferometric region they have a fixed relative vertical separation of 31 cm. The ensembles are prepared in the $|F = 1, m_F = 0\rangle$ state and selected in a longitudinal velocity class corresponding to $\sim$ 80 nK along the vertical direction with three counter-propagating, square Raman pulses with a duration of 24 μs. The three atomic samples are then simultaneously interrogated in a
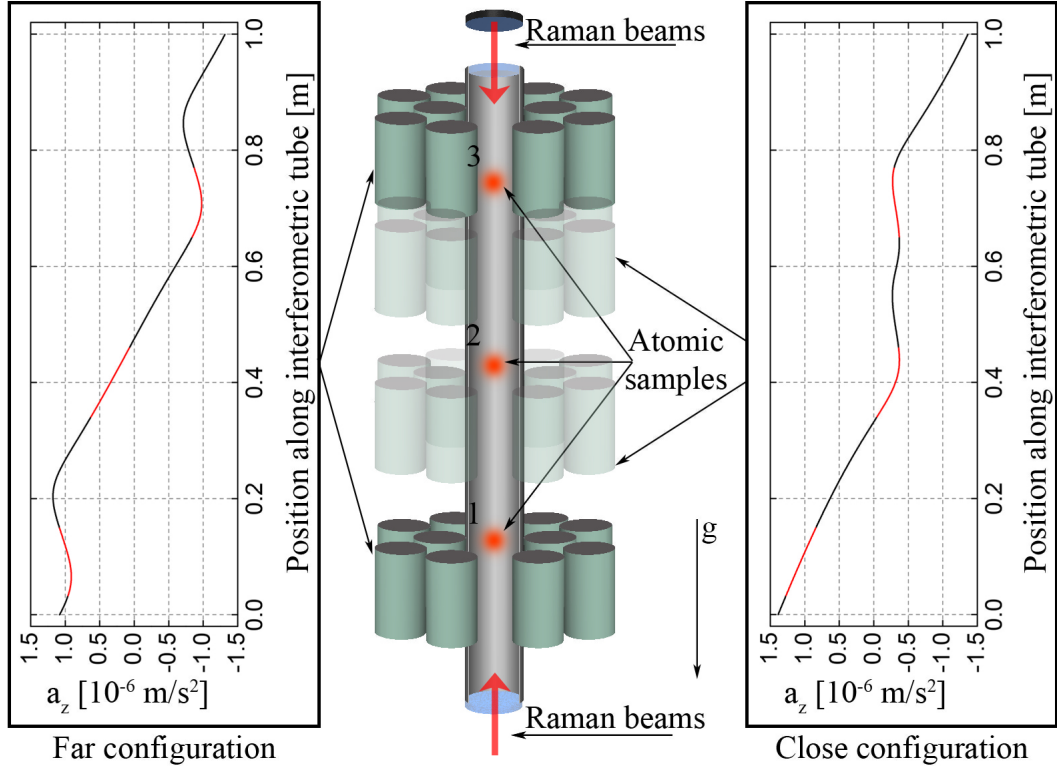
FIGURE 5.21: Scheme of the experimental apparatus. We sequentially launch three atomic samples separated by a fixed vertical distance of 31 cm. The Raman beams are used for the velocity and state selection and for the interferometric interrogation. The three ensembles realize three simultaneous AIs; the AIs signals can be combined to obtain three simultaneous gradiometer signals over three different baselines. The measurements are realized with two different geometrical arrangements of the source masses, i.e. the far and close configurations. In the side panels we show the two different acceleration profiles generated in the interferometric tube; we mark in red the regions in which the interferometers take place. Figure adapted from [103].

MZ interferometer realized with a $\pi/2 - \pi - \pi/2$ sequence of counter-propagating square Raman pulses. The π pulse has a duration of 24 μs, the free evolution time between the interferometric pulses is $T = 160$ ms and an entire experimental cycle takes about 2 s to complete.

The Master Raman laser has a red detuning of 2 GHz from the $5^2S_{1/2}|F = 2\rangle \rightarrow 5^2P_{3/2}|F' = 3\rangle$ transition. During the interferometric sequence, at the moment of the π pulse, this detuning is varied by $\Delta\nu = c\Delta k_{\text{eff}}/4\pi$ in order to introduce the change Δk_{eff} in the transferred momentum required to compensate the gravity gradient.

At the end of the interferometric sequence we use the state selective detection procedure already introduced (see Sec. 4.4) to observe the interference fringes from the three simultaneous interferometers. To reject any systematic effect which does not depend on the direction of the Raman wave-vector k_{eff} (in particular the effect of inhomogeneous magnetic fields) we always apply the k-reversal protocol.

In Fig. 5.21 we report the scheme of the used experimental apparatus together with the acceleration profiles that we can generate with the movable source masses. Since we realize three simultaneous AIs we can obtain three different gradiometric
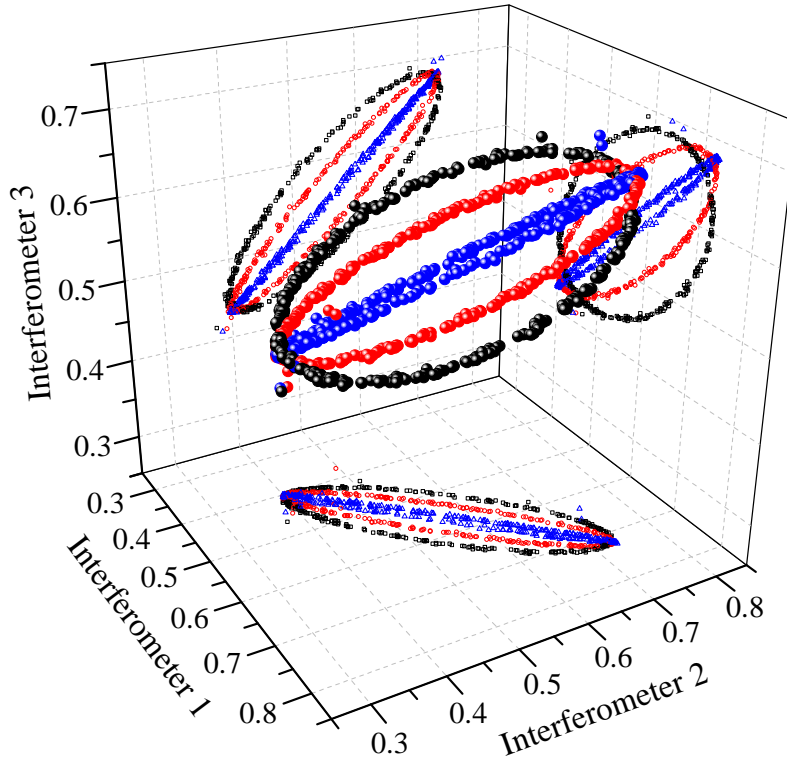
FIGURE 5.22: On each of the three orthogonal axes we plot the signal measured from one of the three simultaneous interferometers (see Fig. 5.21); with the different colors we indicate three different values of the detuning $\Delta\nu$ (steps of 10 MHz) applied during the central π pulse as required by the implemented compensation scheme. The signals from the single AIs can be combined in order to obtain three gradiometric ellipses over three different baselines; these three ellipses constitute the projections of the three-dimensional ellipse. When the gravity gradient is exactly compensated the ellipse degenerates to a line.

signals which measure the gravity gradient over the three different baselines considered: gradiometer 1-2, gradiometer 2-3 and gradiometer 1-3. In Fig. 5.22 we show an example of the typical experimental data that we collect in this configuration. The three-dimensional ellipse is obtained from the signal of the three simultaneous interferometers; its projections on the orthogonal planes constitute the signal of the three cited gradiometers. With the different colors we distinguish the signal for three different detuning $\Delta\nu$ applied during the central π pulse as required from the gravity gradient compensation technique already introduced. We note that when the gravity gradient between two samples is exactly compensated the gradiometric phase angle is zero and the ellipse degenerates to a line (see blue signal in Fig. 5.22).

By moving the sets of source masses along the interferometric tube we can generate the two acceleration profiles shown in the side panels of Fig. 5.21; the vertical region where the interferometers take place is also highlighted in red. In the far configuration the atoms experience a homogeneous gravity gradient over the 1-3 baseline while in the close configuration they experience a strong vertical variation of the gravity gradient.

In the experiment we measure the dependence of the phase angle Φ of the three
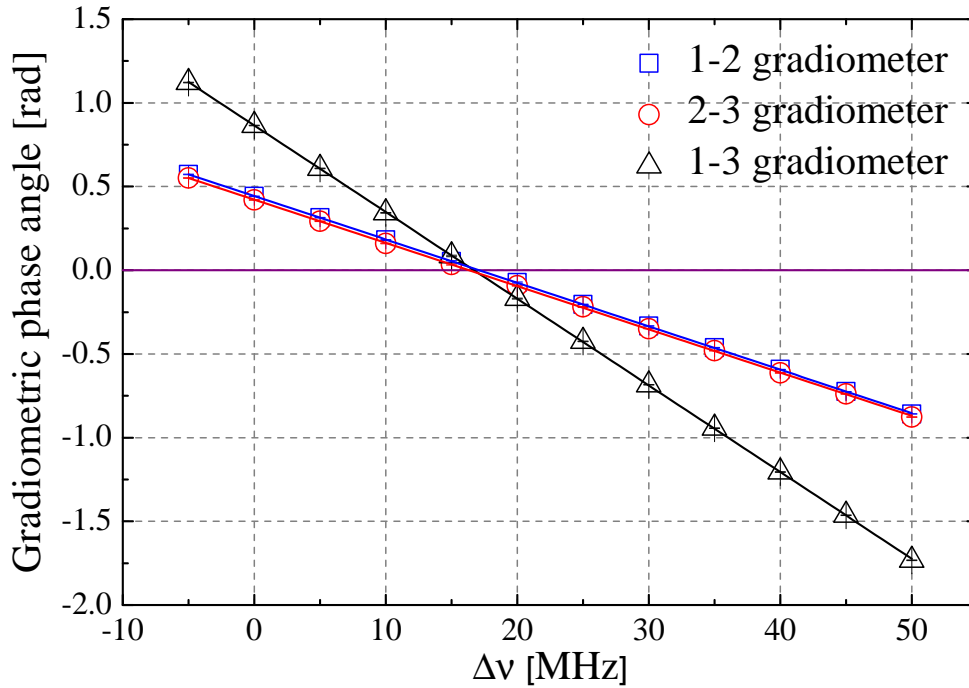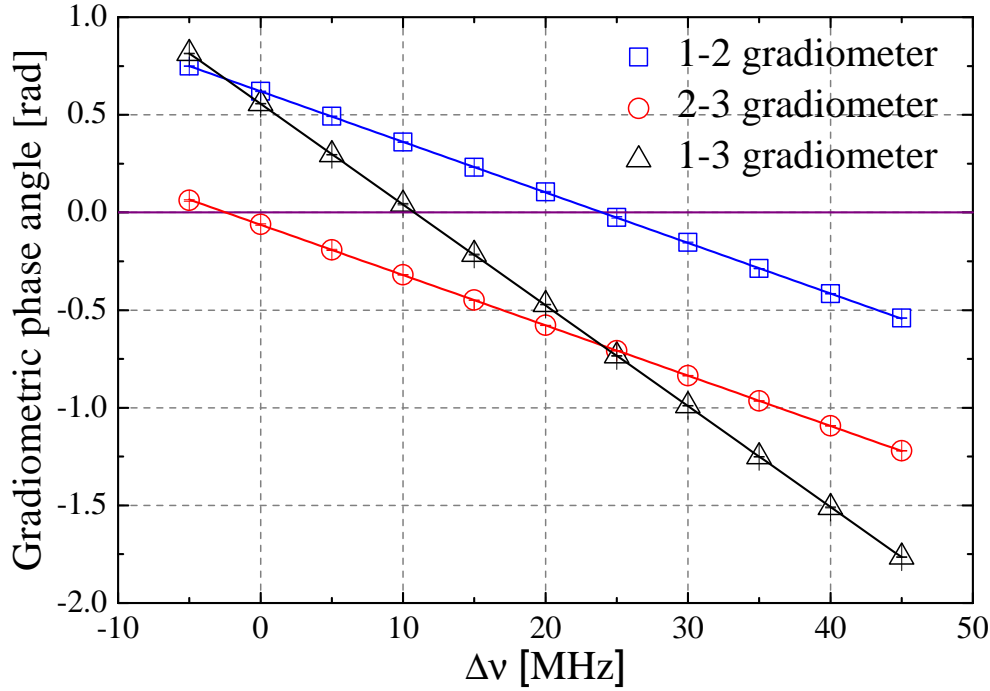
FIGURE 5.23: Phase angle of the three simultaneous gradiometers as a function of the applied detuning $\Delta\nu$ and respective linear fits. The source masses are in the far configuration. As expected the gradiometer with double baseline (1-3 configuration) shows a double slope in the linear behaviour of the phase angle with respect to the other two gradiometric configurations.

simultaneous gradiometers on the introduced frequency detuning $\Delta\nu$ which we expect to be

$$\Phi(\Delta\nu) = \left(k_{\text{eff}}\gamma T^2 + \frac{8\pi}{c}\Delta\nu\right)(d + \Delta v_{z0}T), \tag{5.39}$$

with Δv_{z0} the initial differential velocity between the two atomic samples in the gradiometer and d their vertical separation. When $\Phi(\Delta\nu_0) = 0$ the two interferometers of the gradiometer show the same phase irrespective of their vertical position. With a linear fit of the experimental data it is therefore possible to retrieve the frequency detuning $\Delta\nu_0$ and derive the average gravity gradient over the measurement baseline.

In a first series of measurements we use the far configuration of source masses in order to produce an acceleration profile with a constant gradient in the interferometric region. We report the measured gradiometric phase angles for 12 different detuning $\Delta\nu$ in Fig. 5.23; each point in Fig. 5.23 is derived from a least-squares elliptical fit of a set of 360 data points. From the linear fits we extrapolate three zero crossing frequencies from which we can derive three average gravity gradient values

$$\gamma_{12} = (-3.48 \pm 0.01) \times 10^{-6} \text{ s}^{-2},$$
$$\gamma_{23} = (-3.32 \pm 0.01) \times 10^{-6} \text{ s}^{-2},$$
$$\gamma_{13} = (-3.40 \pm 0.01) \times 10^{-6} \text{ s}^{-2}.$$

The homogeneity of the gravity gradient is within 2%-3% over the 60 cm baseline of the three gradiometers. We note that measuring the gravity gradient with this

FIGURE 5.24: Phase angle of the three simultaneous gradiometers as a function of the applied detuning $\Delta\nu$ and respective linear fits. The source masses are in the close configuration. As expected, the zero-crossing frequency for the gradiometer with the double baseline (i.e. gradiometer 1-3) falls in the middle between the zero-crossing frequencies of the gradiometers 1-2 and 2-3.

method does not require a precise knowledge of the distance d between the gravity sensors; indeed the error on the gravity gradient measure does not change even when the baseline of the measurement is doubled. This could be particularly advantageous for gravity gradient surveys with field apparatuses, for which a precise knowledge of the employed distance d could be not easy to obtain.

We repeated the same measurements with the source masses in the close configuration. In this case we obtain a strong vertical modulation of the gravity gradient (see right panel in Fig. 5.21) thus maximizing the curvature term of the gravity acceleration profile. In Fig. 5.24 we report the experimental data and the linear fits for the three simultaneous gradiometers. In this configuration we obtain

$$\gamma_{12} = (-4.87 \pm 0.01) \times 10^{-6} \text{ s}^{-2},$$
$$\gamma_{23} = (0.497 \pm 0.006) \times 10^{-6} \text{ s}^{-2},$$
$$\gamma_{13} = (-2.193 \pm 0.006) \times 10^{-6} \text{ s}^{-2}.$$

Also in this case we obtain $\gamma_{13} = (\gamma_{12} + \gamma_{23})/2$ as expected.

From the last result for γ_{23} it is evident that the measurement method is able to provide also the sign of the gravity gradient without the need for applying external magnetic fields or performing additional gravity measurements.

This procedure can also be used to obtain a measurement of the distance d between the gravity sensors of the gradiometers. Indeed the angular coefficient of the fitting line for the gradiometric phase angle data provides a measurement of d,
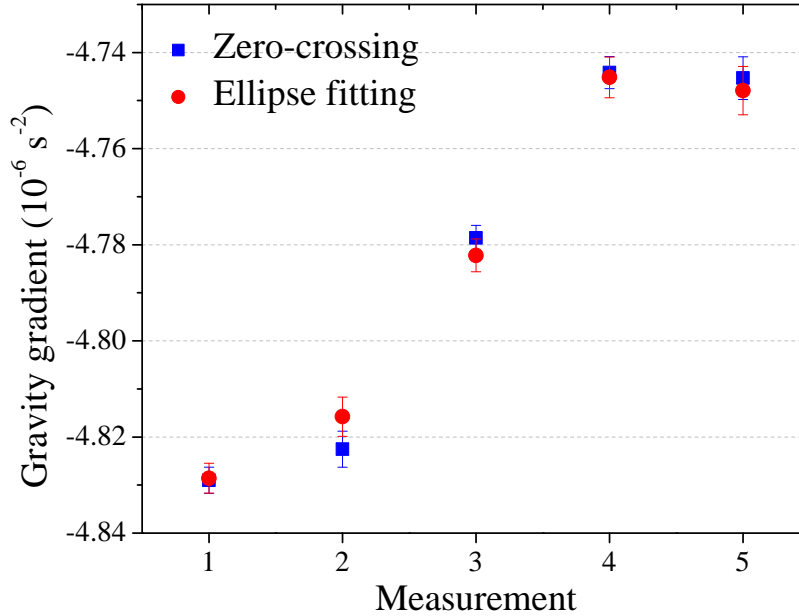
FIGURE 5.25: Gravity gradient measurements obtained from data taken over five successive days. The gravity gradient is derived both with the standard ellipse fitting method and with the new procedure which relies on the zero-crossing frequency. The residual instabilities in the measured gravity gradient values are due to our measurement systematics.

which in our case results to be

$$d_{12} = (30.86 \pm 0.04) \text{ cm},$$
$$d_{23} = (30.72 \pm 0.03) \text{ cm},$$

in agreement with the values measured from the standard time-of-flight technique. We point out that the velocity difference Δv_{z0} between the two ensembles is set by the velocity selection pulses and brings a negligible contribution to the measurement of the distance d. Indeed we can estimate a value of $\Delta v_{z0} \leq 40 \ \mu$m/s with a measurement of the gradiometer phase angle as a function of a small time asymmetry dT in the time interval between the central π pulse and the last $\pi/2$ pulse.

Using the results on the gravity gradients it is also possible to estimate the average gravity curvature over the measurement baseline

$$\zeta = (\gamma_{23} - \gamma_{12})/d = (1.743 \pm 0.004) \times 10^{-5} \text{ m}^{-1}\text{s}^{-2}. \tag{5.40}$$

In a third experiment we positioned the source masses in the far configuration and performed long duration gravity gradient measurements using only two atomic clouds at a distance d of about 33 cm. The atom interferometers are realized in the spatial region where the vertical acceleration profile has a uniform gradient. We measure the gravity gradient both with the standard method of ellipse fitting and with the new technique; this time we use only two values for the detuning $\Delta \nu$. We point out that although the new method still relies on ellipse fitting to obtain the gradiometric phase angles at different $\Delta \nu$, the gravity gradient is derived from the measurement of the zero crossing frequency, i.e. from a linear fit of the phase angles.
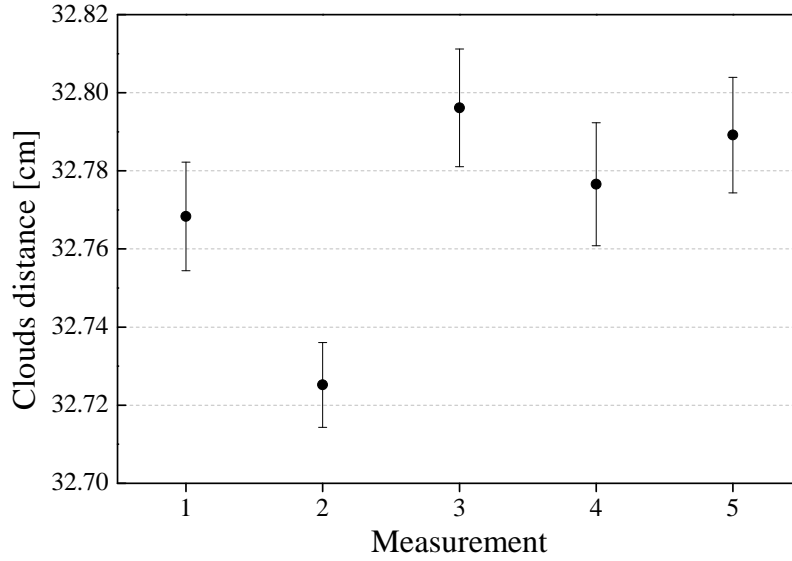
FIGURE 5.26: Distance between the two atomic samples in the gradiometer measured from the slope of the linear fits on the gradiometric phase angle for different detunings $\Delta \nu$.

We realize five different measurement runs over five successive days; the results are reported in Fig. 5.25. The measurement systematics introduce instabilities at the level of 10 mrad; we recall that our major source of instability is represented by the AC Stark shift due to the Raman beams intensity inhomogeneities along the vertical direction. The Coriolis phase shift is compensated with the use of our tip-tilt mirror, however we can still observe systematic shifts at the level of about 4 mrad for a variation of the transverse velocity of 0.1 mm/s.

We also measured the distance between the two atomic samples over the five successive days, from the slope of the linear fit of the phase angle data at different $\Delta \nu$; we found that this distance proves to be very stable at the level of 300 μm and reproducible from day to day (see Fig 5.26). We can then conclude that the measurement systematics has no contribution from a drift or a jitter in the relative position between the two atomic clouds.

We finally tested the influence of the variation in position of the atomic clouds on the measurement of the gravity gradient. Using the far configuration for the source masses and again two atomic samples with a relative vertical distance of about 33 cm, we alternate two measurement cycles in which the position of the upper atomic sample is changed by ± 1 cm. In Fig. 5.27 we report the results of the gravity gradient measurement with both the ellipse fitting method and the zero-crossing frequency method. With the source masses in the far configuration the expected variation of the average gravity gradient should be at the level of 0.04%/cm at the position of the upper sample. This produces a negligible effect over a distance of 2 cm. For this reason irrespective of the upper cloud position modulation the gravity gradient values measured with the zero crossing technique remain stable, with relative variations at the level of a few percent and consistent with the typical variations of the systematics due to the AC Stark shift. The gravity gradient values obtained with the ellipse fitting show higher relative variations, compatible with the ones of the measurement baseline $\Delta d / d$ due to the modulation of the upper sample initial position.
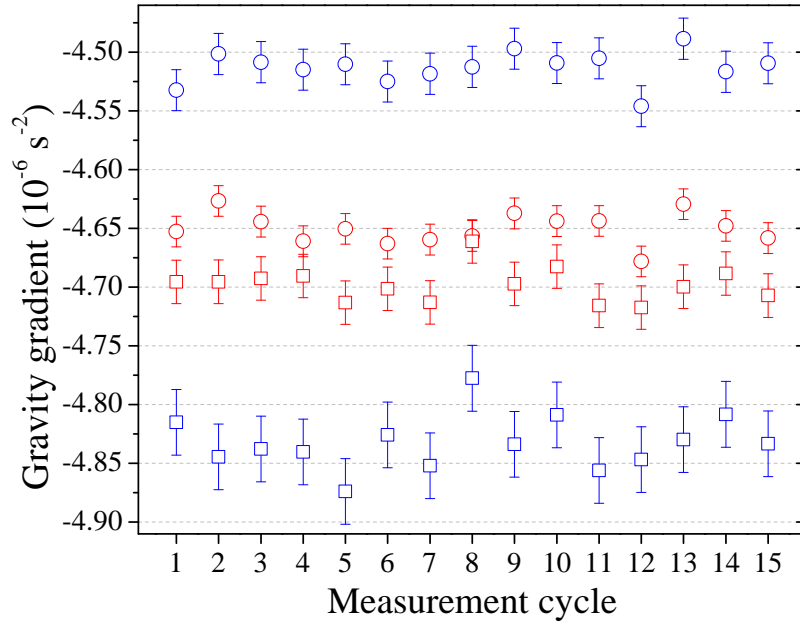
FIGURE 5.27: In blue the gravity gradient measured with the ellipse fitting method, while in red the gravity gradient derived with the zero-crossing frequency technique. For these measurements we modulated the position of the upper sample by ± 1 cm (circle and square data).

In summary we experimentally demonstrated a technique to cancel the dependence of the interferometric phase shift from the initial atomic cloud position and velocity; this dependence arises in presence of gravity gradients and it is particularly problematic for high sensitivity applications of AIs. The proposed technique allows us to reproduce the effects of a fictitious gravity gradient. When the synthetic gravity gradient is exactly opposite to the ambient one, the phase shift of the AI does not depend any more on the initial cloud position and velocity. We applied this technique on simultaneous interferometers with a vertical separation and measured the value of the gravity gradient and the gravity field curvature. In particular, our measurements do not need a precise knowledge of the baseline between the simultaneous interferometers.

Chapter 6

Conclusions

The strong development of AIs brought these apparatuses to performance levels comparable and in some cases even superior than those reached with standard measurement set-ups. This is the case in particular for the measurement of inertial forces and gravitational phenomena which constitutes the main topic of this PhD work. However, despite all the technical enhancements the sensitivity of AIs has not yet reached its ultimate limit. Indeed, since the AIs sensitivity to inertial effects increases with the momentum imparted on the atoms many experimental efforts are devoted to the development of large momentum transfer techniques.

Also in the MAGIA-Adv apparatus we recently added the possibility of stimulating multi-photon Bragg transitions; the first experimental results that we reported are dedicated to the description and characterization of a Bragg gradiometer realized with 3rd order processes. The characterization measurements study the interferometric contrast dependence versus several experimental parameters and were necessary to set the best experimental conditions for the successive measurements with the Bragg interferometer. We also measured the sensitivity of the instrument and found a sensitivity to gravity gradients of 1.2×10^{-6} s^{-2} after 1 s and of 2.6×10^{-8} s^{-2} after an integration of 2000 s. We also analysed the systematic influence on the gradiometric signal of residual magnetic fields and detuning of the Bragg laser beams.

After these characterization measurements we presented a test of the WEP made with ^{87}Rb atoms in different internal states. For this measurements we used the Bragg gradiometer and exploited the particular nature of Bragg transitions which do not change the internal atomic state, but only connect different atomic momentum states. We stress out that lots of experimental tests of the WEP are realized with AIs; they basically measure the difference in acceleration experienced by different atomic species or by the same atoms, but in different internal states. However, the novelty of our test resides in the use of a purely quantum mechanical internal state of the atom. Indeed using ^{87}Rb atoms we compare their free fall acceleration when they are in a definite spin state or in a superposition of two orthogonal spin states. Our experimental procedure can therefore access the quantum aspects of the WEP remained so far unexplored. With our experiment we detected no violation at the level of 5^{-8}. We also improved the results on classical WEP tests with different internal states by one order of magnitude by measuring the Eötvös parameter with a resolution of 10^{-9}. The major limitation in our measurements stems from the AC Stark effect due to the intensity gradients of the Bragg beams. This effect could be mitigated with suitably shaped laser beams and with a light shift compensations scheme [95]. Implementing colder atom sources can reduce the transverse momentum spread of the samples and help in reducing this systematic shift.

In the third set of measurements we demonstrated a gravimetric method particularly suited in conditions of high vibration noise. The method is based on two

Ramsey interferometers which provide two atomic velocimetry measurements separated by a known time T_c. From the measurement of the velocity variation of the atomic clouds over the time T_c we can then derive the value of the gravitational acceleration. The Ramsey interrogation time T has to be short enough in order to guarantee a sufficient wave-packet superposition at the end of the interferometer and maintain the fringe contrast. However the short-term stability of the instrument is limited by T and the interrogation time T_c. With the present experimental apparatus we use T = 200 μs and $T_c = 504$ ms. The long-term stability is instead limited by velocity variations during the preparation phase which can be introduced by the light shift. For these measurement scheme a colder atomic source could be highly beneficial; indeed high atom numbers could still be obtained even for strict longitudinal velocity selections of the atomic samples; furthermore longer interrogation times T could be used with limited loss of contrast due to the increased atomic coherence length. Also in this case a compensation of the light shift can increase the measurement stability and accuracy.

The final experimental results are dedicated to the demonstration of a method to cancel the effects of gravity gradients from the phase shift of a vertical MZ AI. We mentioned that the effect of a gravity gradient can be particularly problematic for demanding applications of AIs. In particular for proposed tests of the WEP at the 10^{-15} level or for other metrological applications. In this regard we also stressed that the major source of systematic error in the determination of the Newtonian gravitational constant G performed with an AI derives from the systematics introduced by gravity gradients. We demonstrated experimentally the method and used it to measure the gravity gradient and the gravity field curvature. Our measurements show that even in presence of non uniform forces an AI can be operated to high accuracy and sensitivity. This technique could be used to perform a new improved G determination with atom interferometry in which it is possible to control the systematics arising from the uncertainty in the initial atomic position and size to an unprecedented level. The details of the new G determination can be found in [108]. With the proposed method the systematic error in the G measurement from the uncertainty in the atomic cloud size and from its positioning along the symmetry axis of the source masses is reduced from 72 to 20 ppm in the present experimental apparatus. With an improved source mass distribution and an increased sensitivity of the gradiometer it is possible to measure G at the 10 ppm level.

Bibliography

[1] P. R. Berman, *Atom Interferometry*. Academic press, Chestnut Hill, 1997.

[2] *Atom Interferometry*. G. M. Tino, M. A. Kasevich eds., SIF, and IOS Press, 2014.

[3] M. Born and E. Wolf, *Principles of Optics*. Cambridge University Press, 1999.

[4] E. Fermi and L. Marshall, "Interference phenomena of slow neutrons", *Phys. Rev.*, vol. 71, pp. 666–677, 1947. DOI: 10.1103/PhysRev.71.666.

[5] L. Marton, "Electron interferometer", *Phys. Rev.*, vol. 85, pp. 1057–1058, 1952. DOI: 10.1103/PhysRev.85.1057.

[6] V. P. Chebotayev, B. Y. Dubetsky, A. P. Kasantsev, and V. P. Yakovlev, "Interference of atoms in separated optical fields", *J. Opt. Soc. Am. B*, vol. 2, pp. 1791–1798, 1985. DOI: 10.1364/JOSAB.2.001791.

[7] J. F. Clauser, "Ultra-high sensitivity accelerometers and gyroscopes using neutral atom matter-wave interferometry", *Physica B*, vol. 151, pp. 262–272, 1988. DOI: 10.1016/0378-4363(88)90176-3.

[8] O. Carnal and J. Mlynek, "Young's double-slit experiment with atoms: A simple atom interferometer", *Phys. Rev. Lett.*, vol. 66, pp. 2689–2692, 1991. DOI: 10.1103/PhysRevLett.66.2689.

[9] D. W. Keith, C. R. Ekstrom, Q. A. Turchette, and D. E. Pritchard, "An interferometer for atoms", *Phys. Rev. Lett.*, vol. 66, pp. 2693–2696, 1991. DOI: 10.1103/PhysRevLett.66.2693.

[10] F. Riehle, T. Kisters, A. Witte, J. Helmcke, and C. J. Bordé, "Optical Ramsey spectroscopy in a rotating frame: Sagnac effect in a matter-wave interferometer", *Phys. Rev. Lett.*, vol. 67, pp. 177–180, 1991. DOI: 10.1103/PhysRevLett.67.177.

[11] M. Kasevich and S. Chu, "Atomic interferometry using stimulated Raman transitions", *Phys. Rev. Lett.*, vol. 67, pp. 181–184, 1991. DOI: 10.1103/PhysRevLett.67.181.

[12] M. Kasevich, D. S. Weiss, E. Riis, K. Moler, S. Kasapi, and S. Chu, "Atomic velocity selection using stimulated Raman transitions", *Phys. Rev. Lett.*, vol. 66, p. 2297, 1991. DOI: 10.1103/PhysRevLett.66.2297.

[13] T. L. Gustavson, P. Bouyer, and M. A. Kasevich, "Precision rotation measurements with an atom interferometer gyroscope", *Phys. Rev. Lett.*, vol. 78, pp. 2046–2049, 1997. DOI: 10.1103/PhysRevLett.78.2046.

[14] T. L. Gustavson, A. Landragin, and M. A. Kasevich, "Rotation sensing with a dual atom-interferometer Sagnac gyroscope", *Classical and Quantum Gravity*, vol. 17, p. 2385, 2000. [Online]. Available: http://stacks.iop.org/0264-9381/17/i=12/a=311.

[15] A Peters, K. Y. Chung, and S Chu, "High-precision gravity measurements using atom interferometry", *Metrologia*, vol. 38, p. 25, 2001. [Online]. Available: http://stacks.iop.org/0026-1394/38/i=1/a=4.

[16]   M. J. Snadden, J. M. McGuirk, P. Bouyer, K. G. Haritos, and M. A. Kasevich, "Measurement of the earth's gravity gradient with an atom interferometer-based gravity gradiometer", *Phys. Rev. Lett.*, vol. 81, pp. 971–974, 1998. DOI: 10.1103/PhysRevLett.81.971.

[17]   J. M. McGuirk, G. T. Foster, J. B. Fixler, M. J. Snadden, and M. A. Kasevich, "Sensitive absolute-gravity gradiometry using atom interferometry", *Phys. Rev. A*, vol. 65, p. 033 608, 2002. DOI: 10.1103/PhysRevA.65.033608.

[18]   A. V. Rakholia, H. J. McGuinness, and G. W. Biedermann, "Dual-axis high-data-rate atom interferometer via cold ensemble exchange", *Phys. Rev. Applied*, vol. 2, p. 054 012, 2014. DOI: 10.1103/PhysRevApplied.2.054012.

[19]   D. S. Weiss, B. C. Young, and S. Chu, "Precision measurement of the photon recoil of an atom using atomic interferometry", *Phys. Rev. Lett.*, vol. 70, pp. 2706–2709, 1993. DOI: 10.1103/PhysRevLett.70.2706.

[20]   S. Gupta, K. Dieckmann, Z. Hadzibabic, and D. E. Pritchard, "Contrast interferometry using Bose-Einstein condensates to measure h/m and α", *Phys. Rev. Lett.*, vol. 89, p. 140 401, 2002. DOI: 10.1103/PhysRevLett.89.140401.

[21]   G. Rosi, F. Sorrentino, L. Cacciapuoti, M. Prevedelli, and G. M. Tino, "Precision measurement of the Newtonian gravitational constant using cold atoms", *Nature*, vol. 510, pp. 518–521, 2014. DOI: 10.1038/nature13433.

[22]   C. R. Ekstrom, J. Schmiedmayer, M. S. Chapman, T. D. Hammond, and D. E. Pritchard, "Measurement of the electric polarizability of sodium with an atom interferometer", *Phys. Rev. A*, vol. 51, pp. 3883–3888, 1995. DOI: 10.1103/PhysRevA.51.3883.

[23]   A. Miffre, M. Jacquey, M. Büchner, G. Trénec, and J. Vigué, "Measurement of the electric polarizability of lithium by atom interferometry", *Phys. Rev. A*, vol. 73, p. 011 603, 2006. DOI: 10.1103/PhysRevA.73.011603.

[24]   S. Fray, C. A. Diez, T. W. Hänsch, and M. Weitz, "Atomic interferometer with amplitude gratings of light and its applications to atom based tests of the equivalence principle", *Phys. Rev. Lett.*, vol. 93, p. 240 404, 2004. DOI: 10.1103/PhysRevLett.93.240404.

[25]   G. Rosi, G. D'Amico, L. Cacciapuoti, F. Sorrentino, M. Prevedelli, M. Zych, Č. Brukner, and G. M. Tino, "Quantum test of the equivalence principle for atoms in coherent superposition of internal energy states", *Nat. Commun.*, vol. 8, p. 15 529, 2017. DOI: 10.1038/ncomms15529.

[26]   G. Ferrari, N. Poli, F. Sorrentino, and G. M. Tino, "Long-lived Bloch oscillations with bosonic Sr atoms and application to gravity measurement at the micrometer scale", *Phys. Rev. Lett.*, vol. 97, p. 060 402, 2006. DOI: 10.1103/PhysRevLett.97.060402.

[27]   S. Dimopoulos, P. W. Graham, J. M. Hogan, and M. A. Kasevich, "General relativistic effects in atom interferometry", *Phys. Rev. D*, vol. 78, p. 042 003, 2008. DOI: 10.1103/PhysRevD.78.042003.

[28]   G. Lamporesi, A. Bertoldi, L. Cacciapuoti, M. Prevedelli, and G. M. Tino, "Determination of the Newtonian gravitational constant using atom interferometry", *Phys. Rev. Lett.*, vol. 100, p. 050 801, 2008. DOI: 10.1103/PhysRevLett.100.050801.

[29] F. Sorrentino, Y. H. Lien, G. Rosi, L. Cacciapuoti, M. Prevedelli, and G. M. Tino, "Sensitive gravity-gradiometry with atom interferometry: Progress towards an improved determination of the gravitational constant", *New Journal of Physics*, vol. 12, p. 095 009, 2010. DOI: 10.1088/1367-2630/12/9/095009.

[30] M. Prevedelli, L. Cacciapuoti, G. Rosi, F. Sorrentino, and G. M. Tino, "Measuring the Newtonian constant of gravitation G with an atomic interferometer", *Phil. Trans. R. Soc. A*, vol. 372, p. 20 140 030, 2014. DOI: 10.1098/rsta.2014.0030.

[31] A. Bonnin, N. Zahzam, Y. Bidel, and A. Bresson, "Simultaneous dual-species matter-wave accelerometer", *Phys. Rev. A*, vol. 88, p. 043 615, 2013. DOI: 10.1103/PhysRevA.88.043615.

[32] D. Schlippert, J. Hartwig, H. Albers, L. L. Richardson, C. Schubert, A. Roura, W. P. Schleich, W. Ertmer, and E. M. Rasel, "Quantum test of the universality of free fall", *Phys. Rev. Lett.*, vol. 112, p. 203 002, 2014. DOI: 10.1103/PhysRevLett.112.203002.

[33] M. Tarallo, T. Mazzoni, N. Poli, D. Sutyrin, X. Zhang, and G. Tino, "Test of Einstein equivalence principle for 0-spin and half-integer-spin atoms: Search for spin-gravity coupling effects", *Phys. Rev. Lett.*, vol. 113, p. 023 005, 2014. DOI: 10.1103/PhysRevLett.113.023005.

[34] L. Zhou, S. Long, B. Tang, X. Chen, F. Gao, W. Peng, W. Duan, J. Zhong, Z. Xiong, J. Wang, Y. Zhang, and M. Zhan, "Test of equivalence principle at 10^{-8} level by a dual-species double-diffraction Raman atom interferometer", *Phys. Rev. Lett.*, vol. 115, p. 013 004, 2015. DOI: 10.1103/PhysRevLett.115.013004.

[35] X. C. Duan, X. B. Deng, M. K. Zhou, K. Zhang, W. J Xu, F. Xiong, Y. Y. Xu, C. G. Shao, J. Luo, and Z. K. Hu, "Test of the universality of free fall with atoms in different spin orientations", *Phys. Rev. Lett.*, vol. 117, p. 023 001, 2016. DOI: 10.1103/PhysRevLett.117.023001.

[36] A. Roura, "Circumventing Heisenberg's uncertainty principle in atom interferometry tests of the equivalence principle", *Phys. Rev. Lett.*, vol. 118, p. 160 401, 2017. DOI: 10.1103/PhysRevLett.118.160401.

[37] M. O. Scully and M. S. Zubairy, *Quantum optics*. Cambridge University Press, 1997. DOI: 10.1017/CBO9780511813993.

[38] G. Lamporesi, *Determination of the gravitational constant by atom interferometry*. PhD thesis, Università degli studi di Firenze, 2006.

[39] P. Cheinet, *Conception et réalisation d'un gravimètre à atomes froids*. Physique Atomique. Université Pierre et Marie Curie - Paris VI, 2006.

[40] H. Müller, S.-W. Chiow, and S. Chu, "Atom-wave diffraction between the Raman–Nath and the Bragg regime: Effective Rabi frequency, losses and phase shifts", *Phys. Rev. A*, vol. 77, p. 023 609, 2008. DOI: 10.1103/PhysRevA.77.023609.

[41] B. V. Estey, *Precision Measurement in Atom Interferometry Using Bragg Diffraction*. PhD thesis, University of California, Berkeley, 2016.

[42] P. Storey and C. C. Tannoudji, "The Feynman path integral approach to atomic interferometry. a tutorial", *J. Phys. II France*, vol. 4, pp. 1999–2027, 1994. DOI: 10.1051/jp2:1994103.

[43] P. Cheinet, B. Canuel, F. Pereira Dos Santos, A. Gauguet, F. Yver-Leduc, and A. Landragin, "Measurement of the sensitivity function in a time-domain atomic interferometer", *IEEE Transactions on Instrumentation and Measurement*, vol. 57, pp. 1141–1148, 2008. [Online]. Available: 10.1109/TIM.2007.915148.

[44] M. Kasevich and S. Chu, "Measurement of the gravitational acceleration of an atom with a light-pulse atom interferometer", *Appl. Phys. B*, vol. 54, pp. 321–332, 1992. DOI: 10.1007/BF00325375.

[45] P. Meystre and M. Sargent, *Elements of Quantum Optics*. Springer Verlag, Berlin, 1999.

[46] D. A. Steck, "Rubidium 87 D line data,", revision 2.1.5, 13 January 2015. [Online]. Available: http://steck.us/alkalidata.

[47] K. Moler, D. S. Weiss, M. Kasevich, and S. Chu, "Theoretical analysis of velocity-selective Raman transitions", *Phys. Rev. A*, vol. 45, p. 342, 1992. DOI: 10.1103/PhysRevA.45.342.

[48] S. S. Szigeti, J. E. Debs, J. J. Hope, N. P. Robins, and J. D. Close, "Why momentum width matters for atom interferometry with Bragg pulses", *New J. Phys.*, vol. 14, p. 023 009, 2012. DOI: 10.1088/1367-2630/14/2/023009.

[49] W. H. Bragg and W. L. Bragg, "The reflection of X-rays by crystals", *Proc. R. Soc. Lond.*, vol. 88, 428–38, 1913. DOI: 10.1098/rspa.1913.0040.

[50] E. M. Wright and P. Meystre, "Theory of an atomic interferometer in the Raman-Nath regime", *Opt. Comm.*, vol. 75, pp. 388–396, 1990. DOI: 10.1016/0030-4018(90)90201-4.

[51] T. Kovachy, S. w. Chiow, and M. A. Kasevich, "Adiabatic-rapid-passage multiphoton Bragg atom optics", *Phys. Rev. A*, vol. 86, 011606(R), 2012. DOI: 10.1103/PhysRevA.86.011606.

[52] B. Estey, C. Yu, H. Müller, P.-C Kuan, and S.-Y Lan, "High-resolution atom interferometers with suppressed diffraction phases", *Phys. Rev. Lett.*, vol. 115, p. 083 002, 2015. DOI: 10.1103/PhysRevLett.115.083002.

[53] C. Lämmerzahl and C. Bordé, "Rabi oscillations in gravitational fields: Exact solution", *Phys. Lett. A*, vol. 203, pp. 59–67, 1995. DOI: 10.1016/0375-9601(95)00402-0.

[54] K. Marzlin and J. Audretsch, "State independence in atom interferometry and insensitivity to acceleration and rotation", *Phys.Rev. A*, vol. 53, p. 312, 1996. DOI: 10.1103/PhysRevA.53.312.

[55] R. P. Feynman, "Space-time approach to non-relativistic quantum mechanics", *Rev. Mod. Phys.*, vol. 20, p. 367, 1948. DOI: 10.1103/RevModPhys.20.367.

[56] G. Dick, *Local Oscillator Induced Instabilities in Trapped Ion Frequency Standards*. Proc. of Precise Time and Time Interval, Redendo Beach, 1987, pp. 133–147.

[57] J. W. Haslett, "Phase waves of Louis de Broglie", *Am. J. Phys.*, vol. 40, pp. 1315–20, 1972. DOI: 10.1119/1.1986821.

[58] C. Antoine, "Matter wave beam splitters in gravito-inertial and trapping potentials: Generalized ttt scheme for atom interferometry", *Appl. Phys. B*, vol. 84, pp. 585–597, 2006. DOI: 10.1007/s00340-006-2378-8.

[59] A. Peters, *High precision gravity measurements using atom interferometry*. PhD thesis, Stanford University, 1998.

[60] S.-Y. Lan, P.-C. Kuan, B. Estey, P. Haslinger, and H. Müller, "Influence of the Coriolis force in atom interferometry", *Phys. Rev. Lett.*, vol. 108, p. 090 402, 2012. DOI: 10.1103/PhysRevLett.108.090402.

[61] J. M. Hogan, D. M. S. Johnson, and M. A. Kasevich. Proceedings of the International School of Physics Enrico Fermi Course CLXVIII on Atom Optics, Space Physics, edited by E. Arimondo, W. Ertmer, W. P. Schleich, and E. M. Rasel (IOS Press, Oxford, 2007), p. 411.

[62] D. W. Allan, "Statistics of atomic frequency standards", *Proceedings of the IEEE*, vol. 54, pp. 221–230, 1966. DOI: 10.1109/PROC.1966.4634.

[63] T. Petelsky, *Atom interferometers for precision gravity measurements*. PhD thesis, Università degli studi di Firenze - Université Paris 6, 2005.

[64] M. Fattori, *Sviluppo di un apparato per la misura di G mediante interferometria atomica*. PhD thesis, Università degli studi di Firenze, 2005.

[65] G. Rosi, *Precision gravity measurements with atom interferometry*. PhD thesis, Università degli studi di Pisa, 2012.

[66] E. Riis, D. S. Weiss, K. A. Moler, and S. Chu, "Atom funnel for the production of a slow, high-density atomic beam", *Phys. Rev. Lett.*, vol. 64, p. 1658, 1990. DOI: 10.1103/PhysRevLett.64.1658.

[67] K. Dieckmann, R. J. C. Spreeuw, M. Weidemüller, and J. T. M. Walraven, "Two-dimensional magneto-optical trap as a source of slow atoms", *Phys. Rev. A*, vol. 58, p. 3891, 1998. DOI: 10.1103/PhysRevA.58.3891.

[68] "RTAI- real time application interface", *Official Website*, [Online]. Available: https://www.rtai.org/.

[69] A. L. Schawlow and C. H. Townes, "Infrared and optical masers", *Phys. Rev.*, vol. 112, p. 1940, 1958. DOI: 10.1103/PhysRev.112.1940.

[70] L. Ricci, M. Weidemüller, T. Esslinger, A. Hemmerich, C. Zimmermann, V. Vuletic, W.König, and T. W. Hänsch, "A compact grating-stabilized diode laser system for atomic physics", *Opt. Commun.*, vol. 117, pp. 541–549, 1995. DOI: 10.1016/0030-4018(95)00146-Y.

[71] C. J. Hawthorn, K. P. Weber, and R. E. Scholten, "Littrow configuration tunable external cavity diode laser with fixed direction output beam", *Rev. Sci. Instrum.*, vol. 72, p. 4477, 2001. DOI: 10.1063/1.1419217.

[72] X. Baillard, A. Gauguet, S. Bize, P. Lemonde, P. Laurent, A. Clairon, and P. Rosenbusch, "Interference-filter-stabilized external-cavity diode lasers", *Opt. Comm.*, vol. 266, pp. 609–613, 2006. DOI: 10.1016/j.optcom.2006.05.011.

[73] A. Giorgini, *Development of a transportable atom interferometer operating as inertial and gravity sensor*. PhD thesis, Università degli studi di Napoli, 2009.

[74] W. Demtröder, *Laser spectroscopy*. 3rd edn. Springer Verlag Berlin, 1998.

[75] R. K. Raj, D. Bloch, J. J. Snyder, G. Camy, and M. Ducloy, "High-frequency optically heterodyned saturation spectroscopy via resonant degenerate four-wave mixing", *Phys. Rev. Lett.*, vol. 44, p. 1251, 1980. DOI: 10.1103/PhysRevLett.44.1251.

[76] D. J. McCarron, S. A. King, and S. L. Cornish, "Modulation transfer spectroscopy in atomic rubidium", *Meas. Sci. Technol.*, vol. 19, p. 105 601, 2008. DOI: 10.1088/0957-0233/19/10/105601.

[77] M. Ducloy and D. Bloch, "Theory of degenerate four-wave mixing in resonant Doppler-broadened media. - ii. Doppler-free heterodyne spectroscopy via collinear four-wave mixing in two- and three-level systems.", *Journal de Physique*, vol. 43, pp. 57–65, 1982. DOI: `10.1051/jphys:0198200430105700`.

[78] J. H. Shirley, "Modulation transfer processes in optical heterodyne saturation spectroscopy", *Opt. Lett.*, vol. 7, pp. 537–539, 1982. DOI: `10.1364/OL.7.000537`.

[79] H. J. Metcalf and P. van der Straten, *Laser Cooling and Trapping*. Springer Verlag, New York, 1999.

[80] L. Cacciapuoti, M. de Angelis, M. Fattori, G. Lamporesi, T. Petelski, M. Prevedelli, J. Stuhler, and G. M. Tino, "Analog+digital phase and frequency detector for phase locking of diode lasers", *Rev. Sci. Instrum.*, vol. 76, p. 053 111, 2005. DOI: `10.1063/1.1914785`.

[81] M. A. Kasevich, E. Riis, S. Chu, and R. G. DeVoe, "rf spectroscopy in an atomic fountain", *Phys. Rev. Lett.*, vol. 63, p. 612, 1989. DOI: `10.1103/PhysRevLett.63.612`.

[82] E. L. Raab, M. Prentiss, A. Cable, S. Chu, and D. E. Pritchard, "Trapping of neutral sodium atoms with radiation pressure", *Phys. Rev. Lett.*, vol. 59, p. 2631, 1987. DOI: `10.1103/PhysRevLett.59.2631`.

[83] A. Clairon, C. Salomon, S. Guellati, and W. D. Phillips, "Ramsey resonance in a Zacharias fountain", *Europhys. Lett.*, vol. 16, p. 165, 1991. [Online]. Available: `http://stacks.iop.org/0295-5075/16/i=2/a=008`.

[84] R. Legere and K. Gibble, "Quantum scattering in a juggling atomic fountain", *Phys. Rev. Lett.*, vol. 81, p. 5780, 1998. DOI: `10.1103/PhysRevLett.81.5780`.

[85] A. Bertoldi, G. Lamporesi, L. Cacciapuoti, M. de Angelis, M. Fattori, T. Petelski, A. Peters, M. Prevedelli, J. Stuhler, and G. M. Tino, "Atom interferometry gravity-gradiometer for the determination of the Newtonian gravitational constant G", *Eur. Phys. Jour. D*, vol. 40, pp. 271–279, 2006. DOI: `10.1140/epjd/e2006-00212-2`.

[86] G. Brisebois, "Low noise amplifiers for small and large area photodiodes", *Linear Technology, Design notes*, vol. 399, [Online]. Available: `http://www.analog.com/media/en/reference-design-documentation/design-notes/dn399f.pdf`.

[87] G. T. Foster, J. B. Fixler, J. M. McGuirk, and M. A. Kasevich, "Method of phase extraction between coupled atom interferometers using ellipse-specific fitting", *Opt. Lett.*, vol. 27, pp. 951–953, 2002. DOI: `10.1364/OL.27.000951`.

[88] "Minuit fitting software", [Online]. Available: `http://lcgapp.cern.ch/project/cls/work-packages/mathlibs/minuit/index.html`.

[89] G. D'Amico, F. Borselli, L. Cacciapuoti, M. Prevedelli, G. Rosi, F. Sorrentino, and G. M. Tino, "Bragg interferometer for gravity gradient measurements", *Phys. Rev. A*, vol. 93, p. 063 628, 2016. DOI: `10.1103/PhysRevA.93.063628`.

[90] A. Louchet-Chauvet, T. Farah, Q. Bodart, A. Clairon, A. Landragin, S. Merlet, and F. Pereira Dos Santos, "The influence of transverse motion within an atomic gravimeter", *New Journal of Physics*, vol. 13, p. 065 025, 2011. [Online]. Available: `http://stacks.iop.org/1367-2630/13/i=6/a=065025`.

[91] T. A. Wagner, S. Schlamminger, J. H. Gundlach, and E. G. Adelberger, "Torsion-balance tests of the weak equivalence principle", *Class. Quantum Grav.*, vol. 29, p. 184 002, 2012. DOI: 10.1088/0264-9381/29/18/184002.

[92] J. G. Williams, S. G. Turyshev, and D. H. Boggs, "Lunar laser ranging tests of the equivalence principle", *Class. Quantum Grav.*, vol. 29, p. 184 004, 2012. DOI: 10.1088/0264-9381/29/18/184004.

[93] J. K. Stockton, X. Wu, and M. A. Kasevich, "Bayesian estimation of differential interferometer phase", *Phys. Rev. A*, vol. 76, p. 033 613, 2007. DOI: 10.1103/PhysRevA.76.033613.

[94] R. G. Schell and G. Tyras, "Irradiance from an aperture with a truncated-gaussian field distribution", *J. Opt. Soc. Am.*, vol. 61, pp. 31–35, 1971. DOI: 10.1364/JOSA.61.000031.

[95] T. Kovachy, P. Asenbaum, C. Overstreet, C. A. Donnelly, S. M. Dickerson, A. Sugarbaker, J. M. Hogan, and M. A. Kasevich, "Quantum superposition at the half-metre scale", *Nature*, vol. 528, pp. 530–533, 2015. DOI: 10.1038/nature16155.

[96] T. Damour, "Theoretical aspects of the equivalence principle", *Classical and Quantum Gravity*, vol. 29, p. 184 001, 2012. DOI: 10.1088/0264-9381/29/18/184001.

[97] S. Merlet, J. L. Gouët, Q. Bodart, A. Clairon, A. Landragin, F. Pereira Dos Santos, and P. Rouchon, "Detecting inertial effects with airborne matter-wave interferometry", *Metrologia*, vol. 46, p. 87, 2009. DOI: 10.1088/0026-1394/46/1/011.

[98] R. Geiger, V. Ménoret, G. Stern, N. Zahzam, P. Cheinet, B. Battelier, A. Villing, F. Moron, M. Lours, Y. Bidel, A. Bresson, A. Landragin, and P. Bouyer, "Detecting inertial effects with airborne matter-wave interferometry", *Nature Commun.*, vol. 2, p. 474, 2011. DOI: 10.1038/ncomms1479.

[99] F. Sorrentino, A. Bertoldi, Q. Bodart, L. Cacciapuoti, M. de Angelis, Y.-H. Lien, M. Prevedelli, G. Rosi, and G. M. Tino, "Simultaneous measurement of gravity acceleration and gravity gradient with an atom interferometer", *Appl. Phys. Lett.*, vol. 101, p. 114 106, 2012. DOI: 10.1063/1.4751112.

[100] M. Carey, M. Belal, M. Himsworth, J. Bateman, and T. Freegarde, "Matter-wave interferometric velocimetry of cold Rb atoms", *J. Mod. Opt.*, vol. 65, pp. 657–666, 2018. DOI: 10.1080/09500340.2017.1397222.

[101] M. de Angelis, F. Greco, A. Pistorio, N. Poli, M. Prevedelli, G. Saccorotti, F. Sorrentino, and G. M. Tino, "Absolute gravity acceleration measurement in atomic sensor laboratories", *Eur. Phys. J. Plus*, vol. 127, p. 27, 2012. [Online]. Available: 10.1140/epjp/i2012-12027-9.

[102] H. Müller, S. Chiow, Q. Long, S. Herrmann, and S. Chu, "Atom interferometry with up to 24-photon-momentum-transfer beam splitters", *Phys. Rev. Lett.*, vol. 100, p. 180 405, 2008. DOI: 10.1103/PhysRevLett.100.180405.

[103] G. D'Amico, G. Rosi, S. Zhan, L. Cacciapuoti, M. Fattori, and G. M. Tino, "Canceling the gravity gradient phase shift in atom interferometry", *Phys. Rev. Lett.*, vol. 119, p. 253 201, 2017. DOI: 10.1103/PhysRevLett.119.253201.

[104] A. M. Nobili, "Fundamental limitations to high-precision tests of the universality of free fall by dropping atoms", *Phys. Rev. A*, vol. 93, p. 023 617, 2016. DOI: 10.1103/PhysRevA.93.023617.

[105] S. Dimopoulos, P. W. Graham, J. M. Hogan, and M. A. Kasevich, "Testing general relativity with atom interferometry", *Phys. Rev. Lett.*, vol. 98, p. 111 102, 2007. DOI: 10.1103/PhysRevLett.98.111102.

[106] D. N. Aguilera, H. Ahlers, B. Battelier, A. Bawamia, A. Bertoldi, R. Bondarescu, K. Bongs, P. Bouyer, C. Braxmaier, and L. Cacciapuoti, "STE-QUEST-test of the universality of free fall using cold atom interferometry", *Class. Quantum Grav.*, vol. 31, p. 115 010, 2014. DOI: 10.1088/0264-9381/31/15/159502.

[107] M. de Angelis, A. Bertoldi, L. Cacciapuoti, A. Giorgini, G. Lamporesi, M. Prevedelli, G. Saccorotti, F. Sorrentino, and G. M. Tino, "Precision gravimetry with atomic sensors", *Meas. Sci. and Technol.*, vol. 20, p. 022 001, 2009. DOI: 10.1088/0957-0233/20/2/022001.

[108] G. Rosi, "A proposed atom interferometry determination of G at 10^{-5} using a cold atomic fountain", *Metrologia*, vol. 55, p. 50, 2018. DOI: 10.1088/1681-7575/aa8fd8.